THE UNIVERSITY OF CHICAGO

ATOM TRAP TRACE ANALYSIS: DEVELOPMENTS & APPLICATIONS

A DISSERTATION SUBMITTED TO
THE FACULTY OF THE DIVISION OF THE PHYSICAL SCIENCES
IN CANDIDACY FOR THE DEGREE OF
DOCTOR OF PHILOSOPHY

DEPARTMENT OF PHYSICS

BY
JAKE CHRISTOPHER ZAPPALA

CHICAGO, ILLINOIS
JUNE 2017

For Nonno,

who saw the best in me before I was even born.

"So' belli i trenini che facciamo alle nostre feste, so' i più belli di tutta Roma. So' belli. So' belli perché non vanno da nessuna parte."

- Jep Gambardella in *The Great Beauty*

TABLE OF CONTENTS

LIST OF FIGURES

LIST OF TABLES

ACKNOWLEDGMENTS

It has been both an honor and a pleasure to conduct research at Argonne National Laboratory (ANL), a privilege for which I must chiefly thank my advisor Zheng-Tian Lu. Besides his constant guidance, Lu provided me a once-in-a-lifetime opportunity by allowing me to be involved with such an incredibly novel and influential scientific technique like Atom Trap Trace Analysis (ATTA). Further on this front, I must offer many thanks to Peter Mueller for his advice and supervision, particularly during the latter half of my tenure, and Wei Jiang, who not only taught me the ATTA technique, but also provided better training than I could ever hope for in the art of being an experimental physicist.

Of course, none of my work at ANL would have been possible without the generous support of the Atom Trapping group's unparalleled engineers, Kevin Bailey and Tom O'Connor, or the wisdom of the group members who have passed through during my time, including especially Jaideep Singh, Michael Bishof, Matthew Dietrich, and Chen-Yu Xu. Also at ANL, my gratitude goes to the whole Medium Energy Physics Group and Physics Division, particularly John Arrington and Robert Janssens for the unrelenting enthusiasm they have given to the continuation of the ATTA lab at ANL. And of course, I cannot describe how much I have appreciated the guidance of the administrative staff, especially Debbie Beres and Barbara Crabtree, without whom I would remain mired in a jungle of bureaucracy, never to graduate.

At the University of Chicago, I must first thank Edward Blucher, who advised me in my first-year, and taught a naive, liberal arts school graduate how to survive the trials of an incredible physics graduate school program. Then my thanks to my thesis committee: Cheng Chin, Steve Sibener, Scott Wakely, and Reika Yokochi. Their suggestions have not only improved my work, but my way of thinking as a scientist. My endless gratitude goes especially to Reika Yokochi, who also managed to make me understand the basics of field work and hydrology, which I initially believed lay beyond my comprehension for all time.

In my various projects and collaborations through ATTA and ANL, I have learned an

incredible amount over the past five years from an uncountable number of people. However, to list a few, who I would be utterly remiss not to mention, my thanks goes to Roland Purtschert, Eilon Adar, Neil Sturchio, Roi Ram, Arik Kaplan, Yoseph Yechieli, and Zhongyi Feng.

Finally, I must thank my family and my friends in Chicago. To my mother, father, and brother, I am eternally grateful in their support for my doing whatever I found myself driven to do, no matter how foolish, and helping me back up whenever I failed. Without them, I would certainly not have found my way to my successes here. And to those friends of mine in Chicago, who have aided me with laughter and joy during the varied oppressions, my many thanks. Especially to those who have suffered alongside me during my tenure, particularly Alex Edelman and Ravi Naik for their moral and ethical support, respectively.

ABSTRACT

Atom Trap Trace Analysis (ATTA) is an efficient and selective laser-based atom counting technique that provides radiokrypton (^{81}Kr and ^{85}Kr) dating to the earth science community. ^{81}Kr (half-life = 230,000 yr) is an ideal tracer for old water and ice with mean residence times of 10^5 - 10^6 years, a range beyond the reach of ^{14}C-dating. ^{85}Kr (half-life = 10.7 yr) is an increasingly important tracer for young groundwater in the age range of 5 - 50 years.

Over the past three years, we have implemented a number of developments that have improved the precision and efficiency of the ATTA technique. These developments have further allowed us to make new leaps in the analysis of both isotopes. For ^{81}Kr, we have demonstrated measurements of ^{81}Kr/Kr with relative one-sigma uncertainties of 1% and placed an improved limit on anthropogenic ^{81}Kr in the atmosphere, removing a systematic constraint to high precision ^{81}Kr-dating. For ^{85}Kr, we have developed new methodologies that increase sample throughput from 1 sample every 48 hours to 6 samples in 24 hours. All the while, we have used the ATTA-3 system at Argonne National Laboratory to continue and provide sample measurements to the scientific community and have now completed over 230 measurements in more than 25 collaborative projects which together span all seven continents.

Finally we have investigated options for further development of the ATTA technique given the growing demand and new applications present within the scientific community at large. Ultimately, we aspire, through ATTA, to make radiokrypton dating as readily and easily available as radiocarbon dating.

CHAPTER 1

INTRODUCTION

1.1 Groundwater and noble gas radionuclides

Groundwater is an increasingly precious natural resource in our society. Of the entire fresh water supply at or near the earth's surface, groundwater and soil moisture account for 98.55% (the remainder being in rivers, lakes, the atmosphere, and the biosphere) (1). Despite its importance, however, we lack a complete understanding of how human activity affects this resource, which can lead to contamination and overexploitation. To prevent such problems we require the ability to model complex environmental systems, such as the hydrology of the aquifers where this groundwater resides. One powerful tool for developing these models are natural and anthropogenic radionuclides. Geoscientists apply these radionuclides as tracers for understanding mixing and transport processes in environmental systems (2).

Probably the most well-known among these radionuclides is ^{14}C. Cosmogenic ^{14}C was discovered in atmospheric CO_2 by Willard Libby in 1946 at the University of Chicago's Institute for Nuclear Studies (now the Enrico Fermi Institute) (3). It is produced in the upper atmosphere by the reaction

$$^{14}\mathrm{N} + \mathrm{n} \longrightarrow {}^{14}\mathrm{C} + \mathrm{p} \tag{1.1}$$

where it oxidizes ultimately to $^{14}CO_2$ and mixes with the atmosphere (4). The atmospheric ^{14}C/C ratio is balanced by uptake from Earth's carbon reservoirs and its natural beta decay, occurring with a half-life of 5730 years (5). In groundwater samples, the cosmogenic production ceases but the decay continues. Thus, upon measuring the ^{14}C/C ratio in a groundwater sample one can determine a radiocarbon age $t_{^{14}\mathrm{C}}$

$$t_{^{14}\mathrm{C}} = t_{1/2} \log_2 \frac{A_0}{A(t)} \tag{1.2}$$

where $t_{1/2}$ is the ^{14}C half-life, A_0 is the atmospheric ratio of ^{14}C/C at the time of the water's entry into the ground, and $A(t)$ is the measured ^{14}C/C ratio in the sample. This "age" determines the time since the groundwater sample has been in contact with the atmosphere, thus allowing groundwater flow paths to be effectively "traced" by use of multiple measurements within a continous hydrological system.

Of course, matters are far more complicated than being able to trace unique flow lines. There are many intricacies due to groundwater mixing processes. Moreover the timescales for transport, recharge, and discharge, within, into, and out of these groundwater aquifers occur over a wide range, spanning the geological history of the Earth. ^{14}C-dating is restricted to the 500 - 50,000 year range due to its half-life.[1] Moreover, radiocarbon dating of groundwater is "certainly one of the most–if not the most–complicated and often questionable applications of radiocarbon dating" (6) due to the aqueous geochemistry of carbon.

Enter the noble gas radionuclides. The application of noble gas radionuclides ^{81}Kr (half-life = 229,000 ± 11,000 years, (7)), ^{85}Kr (half-life = 10.739 ± 0.014 years, (8)), and ^{39}Ar (half-life = 269 ± 3 years, (9)) as environmental tracers extends the available timescales for dating substantially, as can be seen in Figure 1.1. More importantly though, these noble gases have mixing and transport processes that are simpler than other tracers and less subject to contamination due to their chemically inert nature. They each also have unique applications outside of groundwater: increased ^{85}Kr production can be a signal of nuclear fuel reprocessing (10); the age range for ^{39}Ar is ideal for tracing in oceanography (11); and ^{81}Kr can be used to extend our understanding of climate history through ice-core dating (12). As such, demand for these noble gas radionuclides as tracers is rising rapidly in the geoscience community. Unfortunately the isotopic abundances of these noble gas radionuclides are very difficult to measure by using the methods pioneered for radiocarbon dating, such as low-level proportional counting (LLC) and accelerator mass spectrometry

1. If not enough ^{14}C has decayed, the difference in the ratios is too small, if too much has decayed, concentrations are too low to detect and highly sensitive to false positives from contamination.

(AMS). For ^{81}Kr in particular, neither method is capable of providing regular measurements of environmental samples (11). Thus the development of a new technique was required: Atom Trap Trace Analysis (ATTA).

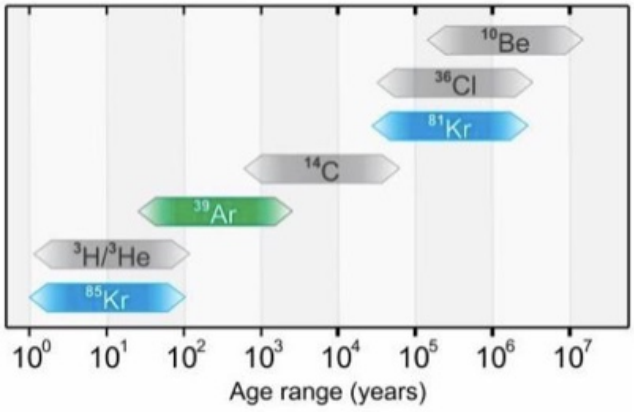

Figure 1.1: A chart which presents the applicable age range of various radionuclides based on their half-lives. The noble gas radionuclides ^{81}Kr (half-life = 229,000 years), ^{85}Kr (half-life = 10.7 years), and ^{39}Ar (half-life = 269 years) are highlighted. They compliment ^{14}C to cover the entire age range from order 1 year to order 1 million years.

1.2 History of ^{81}Kr-dating

Although ATTA is currently capable of measuring ^{39}Ar/Ar relative isotopic abundances[2] in environmental samples (13; 14), the system improved and used for this dissertation is designed only for measuring relative isotopic abundances of krypton isotopes and so ^{39}Ar-dating will not be discussed for the remainder of this dissertation. In addition, although ^{85}Kr-dating on ATTA has led to a series of developments in ^{85}Kr-dating, regular ^{85}Kr-dating was already available through LLC before ATTA's development (2). Thus, to most directly present ATTA's history, the remainder of the introduction will focus on the development and success of ATTA through the lens of ^{81}Kr methods. We will return to discuss the history

2. We define the relative isotopic abundance as the ratio between the isotopic abundance in the sample and the isotopic abundance in a standard reference. ATTA can only perform relative isotopic abundance measurements unless the standard is calibrated by a separate absolute measurement using another method (such as LLC). However, for ^{81}Kr-dating the relative isotopic abundance is sufficient, as we will see in Section 2.3.

and application of ^{85}Kr later in Chapter 5.

^{81}Kr was discovered at Argonne National Laboratory (ANL) in 1950 (15). Its presence in the atmosphere was discovered in 1969 using LLC (16). Its presence in the atmosphere and its decay by electron capture to ^{81}Br with a half-life of $(2.29 \pm 0.11) \times 10^5$ years made it an excellent candidate to supplement radiocarbon dating of groundwater. However, for this application, a problem lay in the detection efficiency of LLC. Krypton is 1.1 parts per million by volume in the atmosphere (17) and the isotopic abundance of ^{81}Kr/Kr is 6×10^{-13} (2). This low abundance, combined with the long lifetime, means that LLC measurements of ^{81}Kr in groundwater samples would require order 10^7 liters of water, wholly unreasonable for regular dating measurements.

The question of ^{81}Kr-dating remained unanswered for nearly 30 years, until AMS was successfully developed for it in 1997 (18) and used to measure environmental samples for the first time in 2000 (19). AMS, the current state-of-the-art for radiocarbon dating, however, is not optimal for ^{81}Kr. In order to prevent isobaric interference during detection a high-energy ($\sim$ 4 GeV) cyclotron is required to produced fully-stripped ^{81}Kr ions, and even then the efficiency of the method still required order 10^4 liters of water. Thus AMS measurements were not further pursued beyond this first breakthrough.

Fortunately, around the same time–also in 1997–development began on ATTA (20). First proof-of-principle measurements demonstrated the selectivity of this new technique, thus overcoming any potential background and contamination issues from other isobars, isotopes, or atomic and molecular species. Although the initial efficiency was only 10^{-7},[3] there was much room for improvement. By 2003 the ATTA-2 system had been developed at ANL and demonstrated an efficiency of better than 10^{-4} (21). This system required a still somewhat large sample size ($\sim$ 1000 L) and the aid of a supplemental measurement of ^{85}Kr/Kr by LLC to produce final ^{81}Kr/Kr relative isotopic abundances, but was used to demonstrate

3. This means that only one out of every ten million atoms was counted. At this rate, making a reasonable measurement on an environmental sample would require a million liters of water, only slightly better than LLC.

^{81}Kr-dating measurements of environmental samples (22).

Improvements continued into 2011, when the technique finally reached the point of being able to offer regular ^{81}Kr-dating measurements to the geoscience community at large, requiring only 100 - 200 liters of groundwater to measure a sample, using the ATTA-3 system at ANL (23). Since then, the ATTA technique has found a number of successful applications for its ^{81}Kr-dating capabilities, beginning with a reconnaissance analysis of noble gas radionuclides in geothermal features at Yellowstone National Park (25).

1.3 Successes of Atom Trap Trace Analysis

Since the commissioning of ATTA-3, ^{81}Kr-dating has found repeated applications in the geoscience community as an environmental tracer including groundwater measurements at the Waste Isolation Pilot Plant (WIPP) (26) and in the Guarani aquifer (27) as well as ice-core dating at Taylor glacier (12).

1.3.1 Waste Isolation Pilot Plant, New Mexico

WIPP is the first geological repository for disposal of transuranic nuclear waste from defense-related programs of the United States Department of Energy (26). The repository is buried over 200 meters below sea level and it is crucial to ensure that there is no pathway for radionuclide transport from the repository into the accessible environment if the repository is disturbed. Although a great deal of numerical flow models have been applied in the area, very few direct studies with isotopic tracers had been conducted prior to (26). Two environmental samples were measured on ATTA-3, SNL-8 and SNL-14 (named, as most samples are, after the local designation of the groundwater wells), which had ^{81}Kr/Kr ratios of 0.50 $\pm$ 0.04 and 0.67 $\pm$ 0.05, respectively. SNL-8 also showed ^{85}Kr activity of 13.6 $\pm$ 1.1 decays per minutes per cubic centimeter of krypton gas at STP (dpm/cc), which was measured in the sample on ATTA-3 simultaneously with the ^{81}Kr/Kr measurement. This

^{85}Kr activity, given the isotope's 10.7 year half-life, represented contamination of modern air, likely from intake during well construction. Using the ^{85}Kr abundance in the air during well completion (approximately 5 times that of the sample), the contamination was corrected for and the ^{81}Kr/Kr relative ratio adjusted from 0.50 ± 0.04 to 0.37 ± 0.05. This monitoring of ^{85}Kr-activity in what we expect to be old groundwater samples is a constant feature of the ATTA technique, always allowing us to apply such corrections if we understand the potential sources of the contamination.

The final values for the ^{81}Kr/Kr relative ratios produced ages of 130 (+48/-41) and 330 (+26/-23) kyr for the high and low transmissivity regions of the aquifer, respectively. Given the disparity with a mean hydraulic age of 32 kyr provided from the flow model, this study directly demonstrated that there exists significant physical attenuation of radionuclides into the accessible aquifer, as hoped.

1.3.2 Guarani aquifer

ATTA was used to perform ^{81}Kr-dating throughout the Guarani aquifer in Brazil in collaboration with the International Atomic Energy Agency (IAEA) as a way investigating radiogenic ^{4}He discharge from the mantle and crust (27). This helium is produced from uranium and thorium α-decay in these areas and this production mechanism is expected to account for approximately 70% of all ^{4}He degassed on Earth. However, the migration pathways and atmospheric residence times resulting from its migration are poorly understood. 15 samples were measured on ATTA-3 at ANL for ^{81}Kr-dating while stable noble gas isotopes of helium, neon, and argon were measured by conventional mass spectrometry elsewhere. The results for the ^{81}Kr-ages and the ^{4}He isotope abundances appear in Figure 1.2. Based on these results, it turns out that ^{4}He resides in the aquifer and travels to the discharge regions, where it is then degassed. This is in contrast to the prior held belief that it was degassed during tectonic events. This update in understanding suggests a reevaluation of ^{4}He residence times and may help to make ^{4}He-dating possible through this crustal

production mechanism in the future.

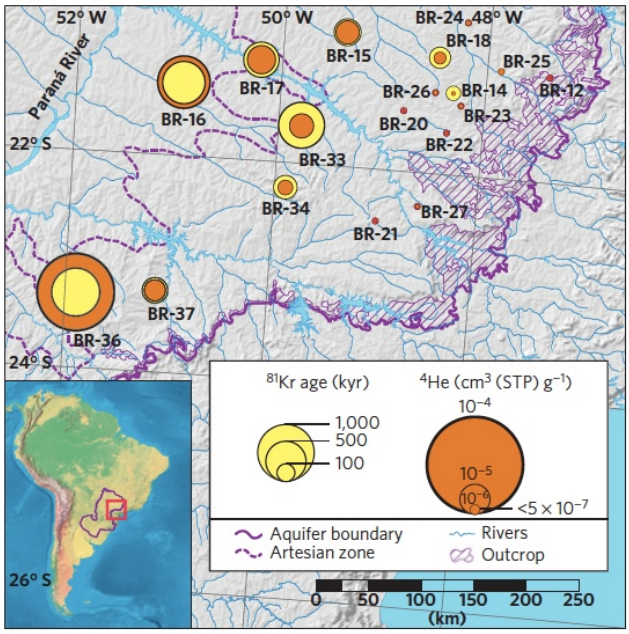

Figure 1.2: ^{81}Kr-ages, represented by the size of yellow circles, and ^{4}He isotopic abundances, represented by the size of orange circles, in wells throughout the Guarani aquifer. Reproduced from (27).

1.3.3 Taylor glacier

^{81}Kr-dating has a special application in extending our understanding of climate models through ice-core dating, and a proof-of-principle project demonstrated that the ATTA technique can be reliably applied to air extracted from ice cores for this purpose (12). Current methods (prior to ATTA and ^{81}Kr-dating) for ice-core dating, which are used to understand past polar temperature and atmospheric compositions, only reach back 800 kyr before present. Moreover, current methods have depended on age being coupled with depth, which is not true at the fringes of glacial outflows where layers of old ice are pushed to the surface. ^{81}Kr-dating offers the opportunity to reach as far back at 1.5 Myr before present as well as to date these fringe regions.

The proof-of-principle measurement was conducted at Taylor glacier for two reasons. First, Taylor glacier provides old ($\sim$ 100 kyr) ice fairly close to the surface allowing for the

collection of the 300 kg of ice needed to conduct a measurement on ATTA-3 at the time. Typical ice core samples (those required to make regular ice core dating feasible) would be closer to 20 kg or less. The second benefit of Taylor glacier is the existence of a nearby ice dome which contains well-stratified layers of ice. These layers each have well-resolved ages with distinct signatures determined by their ^{18}O and CH_4 concentrations. Such signatures can be compared to the surface ice collected for ^{81}Kr-dating as an independent measure of their age for comparison and proof-of-principle.

The location of the glacier in the Antarctic, the positions of the samples in the glacier, and the results of ^{81}Kr-dating using ATTA versus the independent stratigraphic ages are all shown in Figure 1.3, in subfigures A, B, and C, respectively. The good quantitative agreement between the two methods demonstrated the reliability of ^{81}Kr-dating for future use in ice-core dating, provided a continued reduction in sample size requirements for ATTA. As such, reduction of sample size is one of the many developments upon which this dissertation is focused.

1.4 Outline of the dissertation

Our work has sought to further improve the Atom Trap Trace Analysis technique, particularly in the context of ^{81}Kr-dating, ^{85}Kr-dating, and other applications of isotopic abundances measurements for radiokrypton. After we review the concepts behind laser trapping and cooling, as well as the fundamentals of the ATTA technique and the current ATTA-3 beamline in Chapter 2, we will discuss the variety of improvements and developments made to the ATTA-3 system and the ATTA technique as a whole in Chapter 3. Then we detail a pair of breakthroughs in ^{81}Kr and ^{85}Kr analysis made possible by these improvements in Chapters 4 and 5, respectively: the placing of a limit on anthropogenic ^{81}Kr in the atmosphere and a new rapid-processing procedure for ^{85}Kr analysis which increases sample throughput by over an order of magnitude from the previous state-of-the-art.

Alongside our development efforts, we have also continued to apply the ATTA method

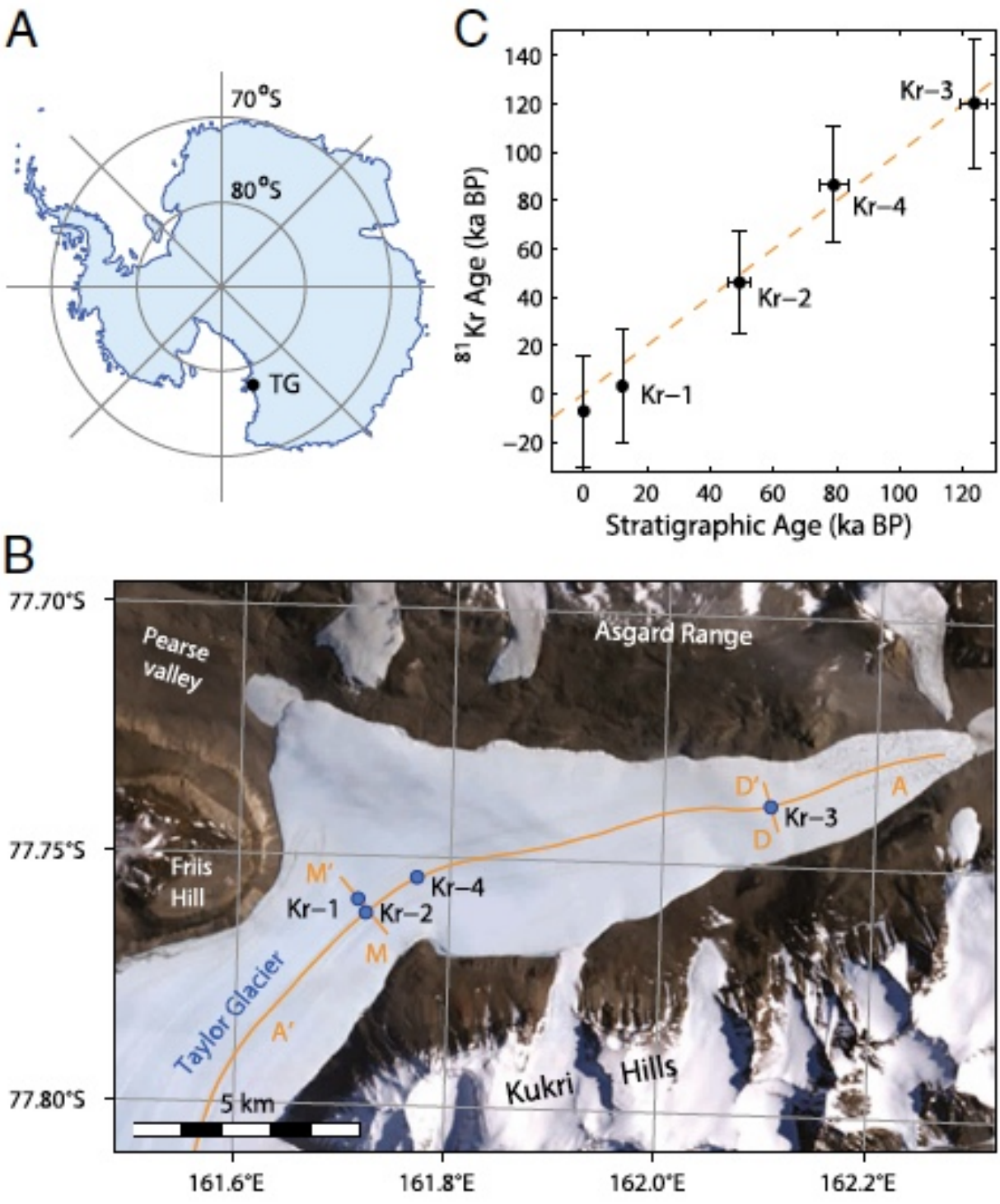

Figure 1.3: (A) The location of Taylor glacier (TG) within Antarctica. (B) The locations of the four ice core samples taken for ^{81}Kr-dating. (C) The results of ^{81}Kr-ages measured by ATTA-3 versus the stratagraphic ages determined by ^{18}O and CH_4 concentrations. Reproduced from (12).

for environmental applications using the continually improved ATTA-3 system at ANL. Our applications have focused on pursuing a better understanding of groundwater transport processes for flow modeling and groundwater management. In Chapter 6 we provide a broad overview of our many projects, as well as a detailed account of our work in the Israel groundwater campaign. The description of the campaign will enable us to present the reader with specific examples of how a groundwater sample is processed from the moment of sampling to analysis on ATTA-3.

We close in Chapter 7 by offering our view on what capabilities a next-generation ATTA system would have in light of the improvements and discoveries we have made as reported in this dissertation, along with developments that we see as available in the near future. We specifically include the results of our brief investigation into sourcing metastable krypton via krypton discharge lamp in Section 7.1.2. A new metastable krypton source, as we will note in more detail later, would be a major improvement that ATTA requires to reach its full potential of making radiokrypton dating as fast, reliable, and readily available as radiocarbon dating to the geoscience community at large.

This disseration presumes the reader has a standard knowledge of quantum mechanics up to the solutions for the energy levels of the hydrogen atom including its fine structure. Additionally, a basic comprehension of optics including the concept of light polarization will be useful. Ideally, we'll take care of the rest.

Furthermore, Chapter 2 of this dissertation–particularly Sections 2.3, 2.4, and 2.5–should be considered a basic user's guide for radiokrypton analysis of environmental samples on ATTA systems based on the ATTA-3 design used at ANL as of the writing of this dissertation. More details for using the ATTA-3 beamline specifically can be found in Appendix A.

CHAPTER 2

ATOM TRAP TRACE ANALYSIS

2.1 Laser cooling tools for slowing krypton

We follow the treatment of Foot (28) to describe how the scattering force from photons can be used to affect the momentum of krypton atoms in our system in Section 2.1.1, as well as to define the effects of the isotope shifts and hyperfine structure in Section 2.1.2.

2.1.1 Principles of the scattering force and doppler shift

Photons have a momentum $\hbar k$, which is imparted to any object which absorbs them. When an atom absorbs a photon, it then spontaneously emits one shortly thereafter (the definiton of "shortly" depending on the lifetime of the newly excited state, τ) and receives a momentum "kick" of $\hbar k$ in the direction opposite the emission, due to the conservation of momentum. However, spontaneous emission does not necessarily occur in the reverse direction of the absorbed photon. In fact, spontaneous emission occurs isotropically, and so these many emitted photons, on average, provide a net zero momentum to the atom. Thus, if the absorbed photons are all being absorbed in one direction–as they would be, say, if provided by a well-collimated laser beam–then the net effect is to change the momentum of the atom in that direction by the total number of photons absorbed by the atom from the laser. Because these absorbed photons are then reemitted, we say that they are scattered and that the incoming photons exert a scattering force F_{scatt}. The magnitude of this force is given by the momentum of each photon multiplied by the rate at which the photons are being scattered

$$F_{\text{scatt}} = \hbar k R_{\text{scatt}} = \frac{\hbar k \Gamma}{2} \frac{I/I_{\text{sat}}}{1 + I/I_{\text{sat}} + 4\delta^2/\Gamma^2}. \tag{2.1}$$

where Γ is the linewidth of the transition, which is equal to the inverse of the lifetime, $\frac{1}{\tau}$, and $I_{\text{sat}} = \frac{\pi h c}{3\lambda^3 \tau}$ is the saturation intensity of the atomic transition. The other two variables,

I and δ are properties of the laser source. I is the intensity of the laser source and δ is the detuning of the laser frequency ω of that source from the central frequency of the transition ω_0 in the atom

$$\delta = \omega - \omega_0 + \mathbf{k} \cdot \mathbf{v} \tag{2.2}$$

The last term of equation 2.2 is worth a moment's discussion. It represents an apparent shift in the laser frequency from the atom's reference frame due to the atom's velocity vector $\mathbf{v}$, and is produced by the overlap between the atom's velocity vector and the wave vector of the photon $\mathbf{k}$. It is known as the Doppler shift, and we will need to always consider it when the atom is in motion.

With the scattering force defined, we can calculate how reasonable it is to stop krypton atoms using laser light. For ATTA, we use the $5s[3/2]_2 \rightarrow 5p[5/2]_3$ electronic transition as our "trapping transition," (the transition can be found in our subsection of the krypton level scheme, Figure 2.5, which appears later for further discussion in Section 2.2.2) using the notation $nl[K]_J$, where n is the principle quantum number, l is the orbital angular momentum of the electron, K is the total angular momentum of the core, excluding the outer electron, and J is K plus the electron's intrinsic spin. We choose this transition because it is closed, meaning that $5p[5/2]_3$ can only decay back down to $5s[3/2]_2$, so we can continuously scatter photons off the atoms without the atom decaying to a different state. Additionally, for this transition $\lambda = 811$ nm, which is a wavelength we can easily produce in the laboratory for trapping and cooling (more on why we use this transition in Section 2.2.2). The transition has a line width of 53 MHz and using the most abundant stable isotope ^{84}Kr, we use a mass of 84 atomic mass units. Considering finally our laser intensity, we must note that, as $I \rightarrow \infty$, $F_{\text{scatt}} \rightarrow \hbar k \Gamma/2$.[1] So we can't just continuously scale up the intensity to increase the force due to limits in the population mechanics of the two states. For our estimation, we will assume that we achieve half the maximum scattering force,

1. We will assume here that we have conspired to make $\delta = 0$, a matter we will deal with on a case-by-case basis throughout Section 2.2

$F_{\text{scatt}} = \hbar k\Gamma/4$. For that, we require that $I = I_{\text{sat}}$, which for the transition in question is order 1 milliwatt per centimeter squared (mW/cm^2) of power. That gives us an acceleration of

$$a = \frac{F_{\text{scatt}}}{M} = \frac{\hbar k\Gamma}{4M} = \frac{2\pi\hbar\Gamma}{4M\lambda} \approx 8 \times 10^4 \text{ m/s}^2 \tag{2.3}$$

inserting the numbers that we just listed. Since atoms at room temperature have an average speed of 300 m/s, the stopping distance for our krypton atoms given this acceleration is about 1.2 m, a value that makes krypton trapping an extremely reasonable endeavor–in theory.

2.1.2 Krypton isotope shifts and hyperfine structure

Just because we can trap krypton atoms, however, it doesn't mean we can do radiokrypton dating. The more important matter is to uniquely select the extremely rare radioactive isotopes from among the abundant stable isotopes. Then we can measure the relative isotopic abundances we need for Kr-dating.

Krypton's natural isotopic abundance distribution is split among six stable isotopes ^{78}Kr (0.35%), ^{80}Kr (2.25%), ^{82}Kr (11.6%), ^{83}Kr (11.5%), ^{84}Kr (57%), and ^{86}Kr (17.3%). Of course, there are also our two long-lived radioactive isotopes, ^{85}Kr with a modern isotopic abundance of 2×10^{-11} and ^{81}Kr with an isotopic abundance of 6×10^{-13}. The even isotopes have no nuclear spin. ^{83}Kr and ^{85}Kr have nuclear spin I = 9/2, ^{81}Kr has nuclear spin I = 7/2.

Rather fortunately for us, these krypton isotopes have a slightly different trapping transition wavelength from one another due to their "isotope shifts" (29). These are changes in the electronic energy states due to the differing mass as well as size and shape of the nucleus. The heavier the nucleus, the higher the energy levels due to an increase in the reduced mass system of the electron and nucleus on which these levels depend. This is called the "mass shift." The size and shape of the nucleus, meanwhile, determine the exact distribution of

the electric field with which the electrons are interacting. For small atoms, approximating a spherical electrical charge distribution is fine, but as nuclei grow, this approximation begins to falter. The energy shifts in the atomic levels due to difference between this approximation and reality are known as "field shifts."

We can see the combined effects of the mass and field shifts for each isotope by scanning the laser frequency in our krypton trap and examining the fluorescence from the scattered krypton atoms that we trap across these frequencies, as was done in Figure 2.1.

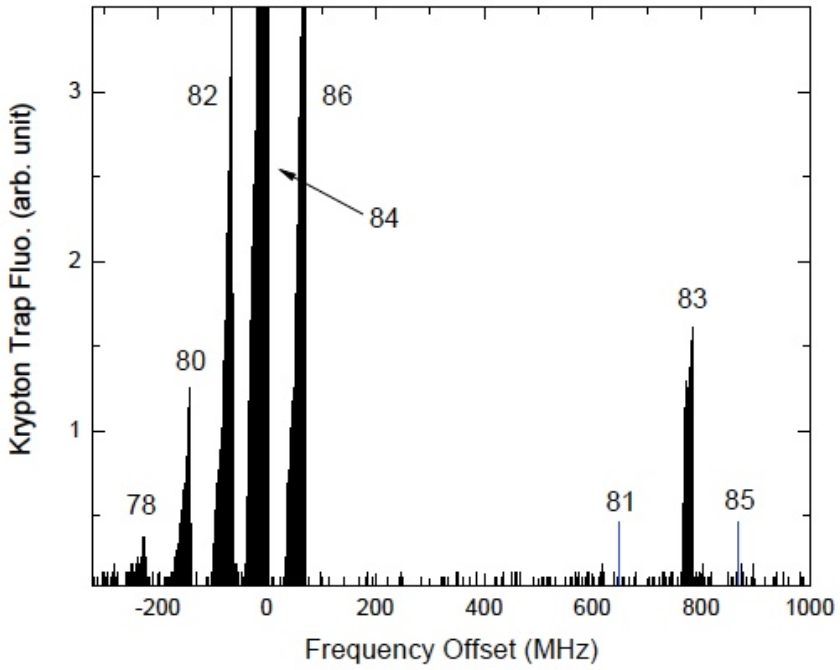

Figure 2.1: Fluorescence of trapped Kr atoms versus laser frequency of the trapping laser. The central frequency for each isotope is marked. ^{81}Kr and ^{85}Kr positions are marked, although their fluorescence does not appear at this detection level. Reproduced from (30).

We see that the even stable isotopes reliably fit the pattern described, but ^{83}Kr appears outside the others, as do the positions marked for ^{81}Kr and ^{85}Kr (obviously at this detection level, due to their low isotopic abundances, we cannot see their fluorescence, which is why they are only marked). The reason for the additional shift in the odd isotopes is due to the nuclear spins mentioned earlier. These nuclear spins can interact with the magnetic flux density and electric field of the electrons to split the energy levels, resulting in what

is known as the hyperfine structure of atom. The central energy value of these multiple states averaged over the number of magnetic sub-levels in each state (which arise from the multiple alignment possibilities of an external magnetic field with the angular momentum of the atom) does in fact fall at the location we would expect from calculating just the isotope shifts. However, the particular hyperfine transitions that we use for trapping ^{81}Kr, ^{83}Kr, and ^{85}Kr, fall where they are marked in Figure 2.1.

However, the non-trapping transitions of the hyperfine structure are quite important as well. Of the many states, the trapping transition is chosen to be between the largest F states (known as the "stretched states"), where F is the total angular momentum of the atom, and represents the alignment of the nuclear spin I with the total electron angular momentum J, as discussed, such that $\mathbf{F} = \mathbf{I} + \mathbf{J}$. Note that these stretched states happen to actually be the lowest lying energy levels because the magnetic dipole hyperfine constant is negative. For ^{83}Kr and ^{85}Kr the transition between stretched states is the $F = 13/2 \rightarrow 15/2$ transition and for ^{81}Kr it is the $F = 11/2 \rightarrow 13/2$ transition.

Now, because we have chosen these stretched states, dipole selection rules ($\Delta F = 0, \pm 1$) prevent the excited 15/2 (^{83}Kr and ^{85}Kr) and 13/2 (^{81}Kr) states from decaying anywhere but to the states from which we excited them (13/2 and 11/2, respectively). However, when we are exciting these trapping transitions, it is possible that the our laser may pump the atom to a different excited stated due the closeness of these hyperfine levels versus their linewidth. Atoms which enter these other excited states may not decay back down to the lowest-lying level from which we excited them, but instead to a higher energy ground state, which we call a "dark" state. We use the term dark because if an atom is one of these states, we will not be able to scatter photons from it anymore using our laser tuned to the trapping transition. As such, we need to use "repumping" lasers to remove atoms from these dark states. The transitions for these repumping lasers are marked in a diagram of the hyperfine states in Figure 2.2. In practice, the number of repump frequencies required depends on the probabilities of exciting to the wrong upper state–some are rare enough that adding another

repump laser does not add to the efficiency of the cooling. We will mention specifically how many repump lasers are used at each stage of cooling throughout the Chapter and we list the specific frequencies applied to produce these repump beams on ATTA-3 in Appendix A.

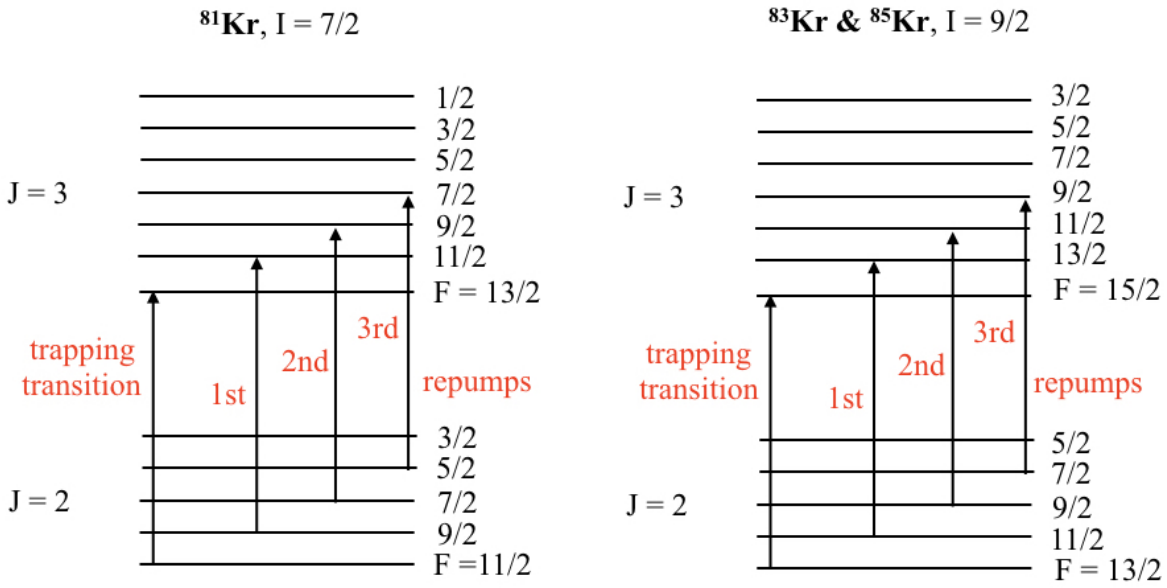

Figure 2.2: Diagram of the hyperfine structure for ^{81}Kr (left) with $I = 7/2$ and ^{83}Kr/^{85}Kr (right) with $I = 9/2$. The upper levels represent states with atomic angular momentum of $J = 3$ ($5p[5/2]_3$), and the lower levels J=2 ($5s[3/2]_2$). The trapping transition is marked along with the 1st, 2nd, and 3rd repump transitions. Although we can have as many as four repump transitions, the fourth is never applied as it does not add to the cooling or trapping efficiency in any section of the beamline.

Given these repump beams and the isotope shift, we thus have the theoretical capabilities to uniquely slow any isotope of krypton using laser light. We will now see how ATTA brings that into practice in Section 2.2 with the help a few other key tools, including most crucially the radio-frequency-driven plasma discharge source (Section 2.2.2), the Zeeman splitting of the electronic structure (Sections 2.2.4 and 2.2.5), single atom detection (Section 2.2.6), and ion collection from a metastable magneto-optical trap (MOT) (Section 2.2.7).

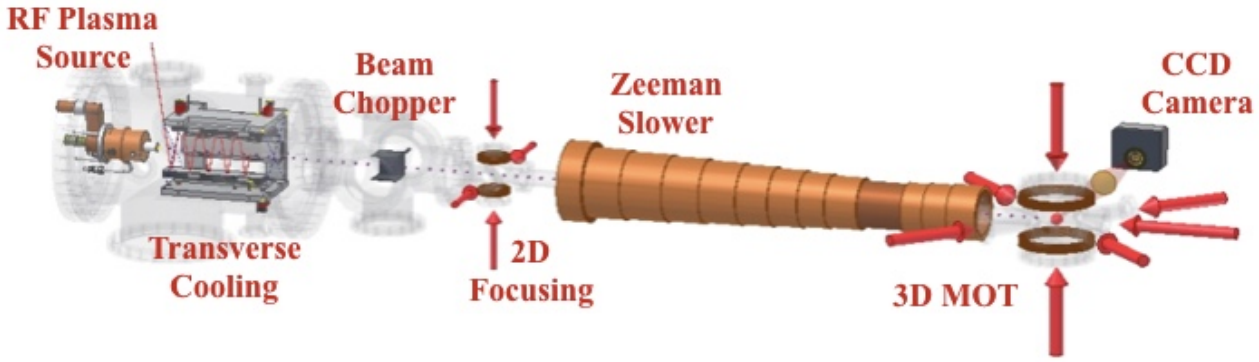

Figure 2.3: Schematic of the ATTA-3 vacuum beamline used to trap krypton atoms at ANL. The various sections mentioned in the figure are detailed throughout the Section. Figure courtesy of Thomas O'Connor.

2.2 ATTA-3 beamline

With the basic tools of the scattering force, doppler shift, isotope shift, and hyperfine structure, we are now ready to address the manner in which the ATTA technique is applied on the ATTA-3 system to measure relative isotopic abundances of ^{81}Kr/Kr and ^{85}Kr/Kr. Figure 2.3 is a diagram of the ATTA beamline which marks the tools to be described in the remainder of this Section.

2.2.1 Laser systems

We cannot do much laser scattering without lasers, so before we address the atomic beamline we must first present the layout of the optical setup which provides laser light to the beamline. The layout appears in Figure 2.4. We will take a tour through each portion of the layout now, but refer to it throughout the Section as we step through the stages of the beamline.

The system begins with an external cavity diode laser (ECDL, DL 100 from Toptica) set to 100 MHz below the frequency of the isotope we wish to trap, that is, ^{81}Kr, ^{85}Kr, or ^{83}Kr.[2] We then split the beam into three separate paths. One goes to a Bristol Waveme-

2. We have selected ^{83}Kr rather than one of the even isotopes as our stable isotope for comparing to the abundances of ^{81}Kr and ^{85}Kr because we want both our radioactive isotopes and our stable isotope to be sensitive to shifts in our repump efficiency, which ^{83}Kr is since it is the only stable isotope with hyperfine structure.

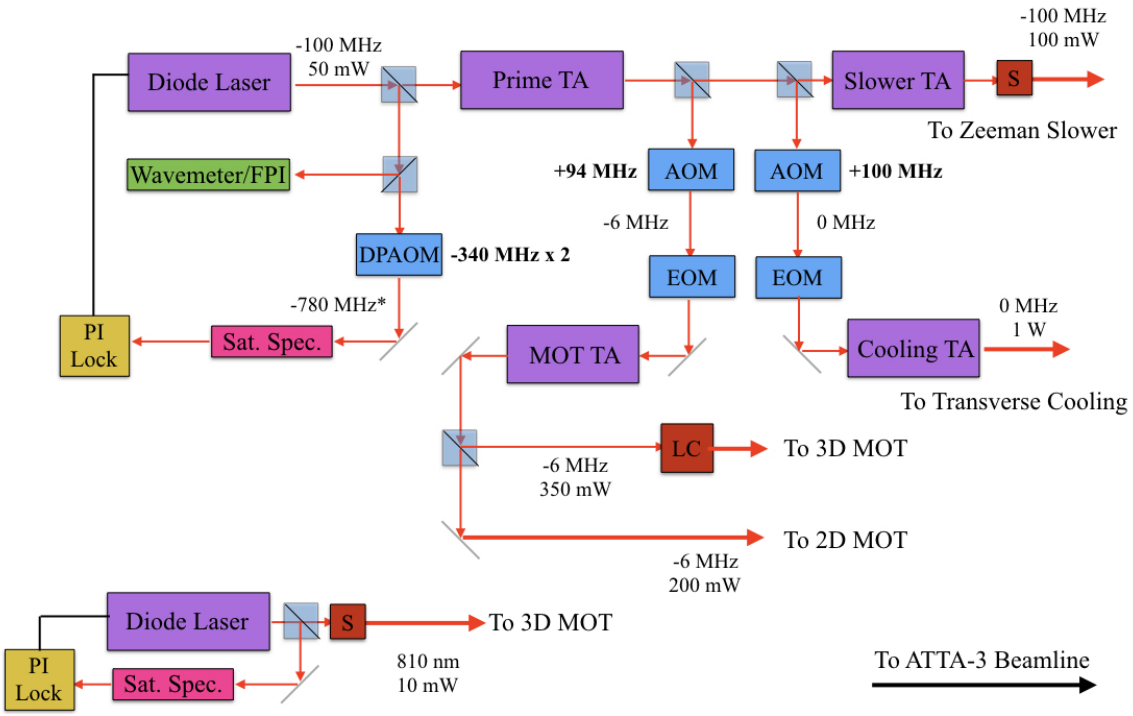

Figure 2.4: Diagram of the optical system for ATTA-3. The diagram presents how the lasers used for cooling and trapping are produced from external cavity diode lasers and amplified by various tapered amplifiers. Also marked are the saturation spectroscopy setup used to lock the laser, diagnostic tools (Wavemeter/FPI, see text) various frequency shifting devices (AOMs and EOMs with their shifts marked beside them in bold, see text), and switches/shutters (LC and S, see text) to alter, stabilize, or remove laser beams. The final powers shown going to the system are the powers required before splitting for beams in multiple dimensions, additional shifts in beam size, and polarization shifts. The frequencies shown are with respect to the trapping transition of the isotope being trapped.*This frequency is specific to ^{83}Kr (see text).

ter for keeping track of the laser frequency, and when needed for diagnostics regarding the laser's mode, a Fabry-Perot cavity. Another arm travels to a frequency modulated saturation spectroscopy setup (31). This arm is first shifted using a double-pass acoustic optical modulator (AOM) to move the frequency to the trapping transition of ^{84}Kr ($\sim$780 MHz below for ^{83}Kr, $\sim$650 MHz below for ^{81}Kr, and $\sim$870 MHz below for ^{85}Kr). Because ^{84}Kr is the most abundant of the isotopes, it provides the strongest signal for locking the laser onto in our saturation spectroscopy setup. The setup uses a cell filled with krypton gas that is subject to a radio-frequency discharge thus producing excited Kr atoms in the lower level of the trapping transition for us to do the spectroscopy. The signal is then sent to a proportional-integral lock box which feeds back a voltage to the piezo-crystal (which controls the laser cavity of the ECDL) as well as a feedback to the main current of the ECDL. The final arm provides the laser light to the rest of the system for cooling and trapping, which is amplified by a home-built tapered amplifier (TA) using a TA diode chip from Eagleyard (EYP-TPA-0808-01000-4006-CMT04-0000).

The -100 MHz is already set for the Zeeman slower to be described in Section 2.2.5 and merely requires amplification. For that we use a TA100 tapered amplifier from Toptica to ultimately send 100 mW of light to our system. There is also a shutter in front of the tapered amplifier to block the slowing light as is needed.

Light for the transverse cooling (Section 2.2.3) and the MOTs (Section 2.2.4 and 2.2.6) are sent through single-pass AOMs to shift their frequencies to the trapping frequency and -6 MHz from the trapping frequency, respectively. Those beams are then passed through electro-optical modulators (EOMs) to add frequency sidebands which can be amplified along with the main carrier beam to provide our repump lasers (32). The amplification is provided by a pair of home-built TAs again using Eagleyard chips, although with higher output (EYP-TPA-0808-02000-4006-CMT04-0000, 2 W maximum). The beam for the MOTs is further split between the 2D MOT for focusing and the 3D MOT for trapping. The beam for the 3D MOT passes through a Swift Variable Retarder from Meadowlark. Provided a voltage to

the control unit, the non-linear liquid crystal element inside the Retarder allows us to vary the output power to the 3D MOT.

Lastly, at the bottom of Figure 2.4 there is a second ECDL (another DL100 from Tui Optics [now Toptica]). This provides laser light at 810 nm, which can excite the atoms from the lower-level of the trapping transition to a separate excited state ($5p[5/2]_2$), which is not a closed transition and can thus decay to the ground state (see Figure 2.5, discussed in Section 2.2.2). This effectively removes trapped atoms from our 3D MOT and is known as our "quench transition." This laser is also locked using a discharge cell and saturation spectroscopy setup. There is a shutter to turn this laser beam on and off. We will discuss why we require this laser in Section 2.2.6.

2.2.2 Radio-frequency-driven plasma discharge source

Those familiar with atom trapping will know that when you have a convenient cycling transition where the ground state is the lower of the two levels, it is certainly the trapping transition to use. However, that is not the case for noble gases. The reason they are chemically inert is because they have closed electron shells that are highly resistant to being excited, that is, it takes quite a bit of energy to get them to even their first excited state. Figure 2.5 shows a small fraction of the level diagram for krypton with the requisite levels for our discussion.

The labeled "strong transition" is the most easily accessed excited state above the ground state with respect to oscillator strength and selection rules. However, to use it as the cycling transition would require that all of the laser light we use for cooling and trapping be replaced with 124 nm light produced from a continuous-wave narrowband laser. That is not available. In fact, there isn't even enough 124 nm laser light readily available to optically excite a sufficient amount of krypton atoms into that excited state for transfer to another state. So not only do we require another transition, but we require a non-optical method to reach the

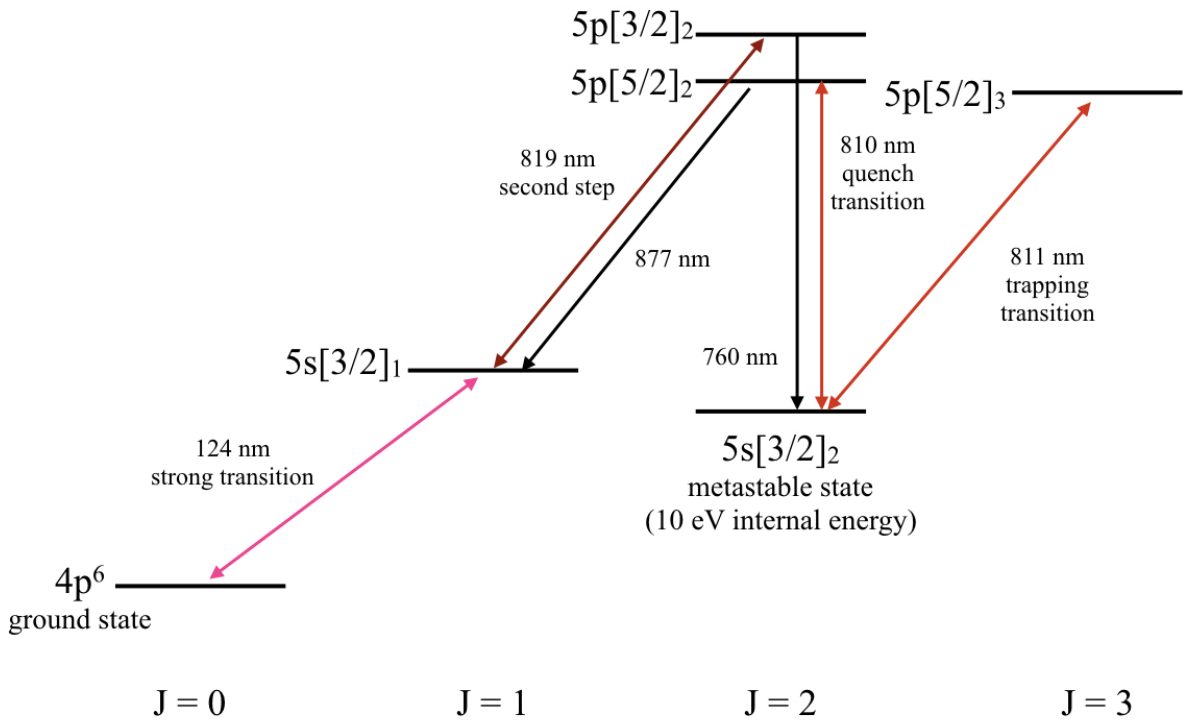

Figure 2.5: A relevant subsection of the electronic level diagram for krypton atoms. The metastable state is the lower level of our trapping transition (the 811 nm cycling transition) and sits 10 eV above the ground state. An optical path to this state is shown using a 124 nm transition, an 819 nm transition, and a 760 nm photon decay. The quench transition is also shown, which following the 810 nm excitation, allows the atom to decay to the ground state via an 877 nm photon decay channel. The $nl[K]_J$ notation is used.

state necessary for this transition.[3]

As stated, we have chosen the $5s[3/2]_2 \rightarrow 5p[5/2]_3$ 811 nm cycling transition as our trapping transition. Due to selection rules it is very difficult to decay out of the lower lying level naturally, which results in it being a metastable state with a lifetime of 40 s. Next to the ground state, a long-lived metastable state is the best thing one can hope for in terms of a trapping transition. Additionally, we would like it to be a strong transition. The more photons we can scatter per second, the more efficient we can be about cooling and trapping (the strength of this transition is, as mentioned, represented by I_{sat} in equation 2.1). Fortunately this transition has a scattering rate of 10^7 photons per second, which is quite good indeed (as noted by our little atom slowing calculation in Section 2.1.1). So we have the transition, but how do we get there if not by the optical path (shown also in Figure 2.5)?

The answer in ATTA is to use a radio-frequency-driven discharge source to produce a plasma (33). The plasma excites the electrons of the atoms, ionizing some and putting others into all manner of excited electronic states. Those in the excited states mostly decay back down to the ground state, but 10^{-4} - 10^{-3} of the atoms actually end up in the metastable state, becoming what we will refer to as metastable krypton atoms or Kr^*. It is this small fraction of atoms that we can cool and trap with the remaining tools as they proceed down the beamline.

In practice we inject the krypton gas into our vacuum system where it enters into a volume with pressure typically on the 1 mTorr level. That volume directly adjoins our source, drawn in Figure 2.6. The gas enters from the left side of Figure 2.6 (a) and proceeds into a narrow aluminum-nitride (AlN) tube with a quartz liner at the upstream end that covers approximately half of the AlN tube. Crucially, the AlN is a good conductor of heat but neither AlN or quartz are good conductors of electricity.

The heat conductance of the AlN tube allows us to easily cool the it with liquid nitrogen

3. At least for now. We'll return to the optical possibilities in Section 7.1.

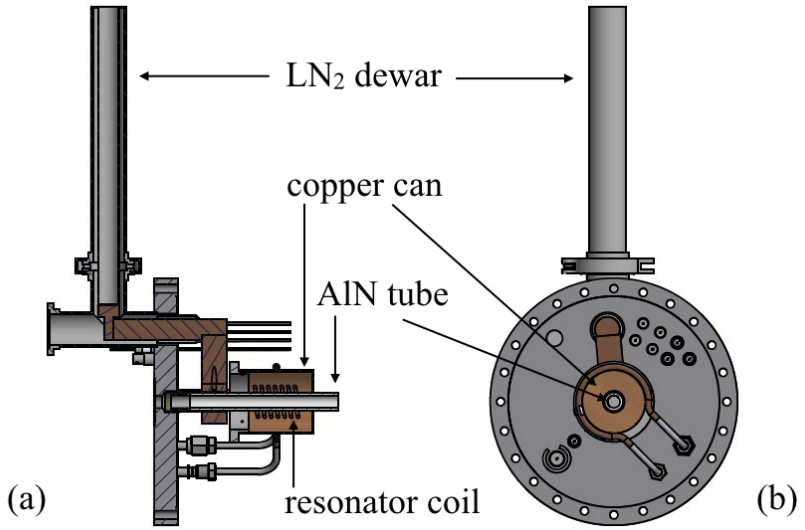

Figure 2.6: Drawing of the RF source. (a) The direction of downstream goes from left to right. In this cutaway, we see the AlN tube through which the gas travels surrounded by the coil and can (see text). Atop is the ℓN_2 mini-dewar which transfers cooling through the copper arm. (b) A view from the downstream direction (that is, downstream points out of the page), which includes various connection points where wires are attached to feed RF into the vacuum system (as well as heating if we so choose). Figure courtesy of Kevin Bailey.

(ℓN_2), a cooling which is transfered to the atoms when they bounce off the tube walls, thus slowing them from room temperature down to about 100 - 110 K.[4] The ℓN_2 is continuously refilled into the mini-dewar at the top of Figure 2.6. This dewar is connected to a copper arm which clamps onto the AlN tube to transfer the cooling effect.

The poor electrical conductance of the AlN tube (and quartz) containing the plasma is necessary for forming the plasma. Around the tube is a grounded copper can, as well as a copper coil with 11 turns, which is attached to the can at one end. This coil acts as a helical resonator (34) that enhances the radio-frequency (RF) fields, to make striking a plasma discharge easier. One turn into the coil there is connection to bring in a RF signal at 200-210 MHz and 22-24 W,[5] exciting the third harmonic of the coil's resonant frequency

4. We don't reach 77K because the heat dissipated by the plasma raises the equilibrium temperature above the temperature of the ℓN_2. However, we make no effort to alter this situation because below 100 K the krypton gas begins to freeze out on the chamber walls.

5. These parameters need to be optimized to the conditions of the tube, which change over long periods of exposure to the plasma discharge.

(typically 70-80 MHz). Due to their only being insulating material available within the coil (which, to note, includes the quartz liner), the RF has a chance to couple to the gas inside the tube, sparking the plasma and beginning metastable production. Thus coming out of the end of the tube then, we typically have an angular flux density of 10^{13} - 10^{15} $\mathrm{s}^{-1}\mathrm{sr}^{-1}$ Kr* entering the rest of our system.

2.2.3 Transverse cooling

The krypton gas exits the discharge tube as a diffuse cone into the transverse cooling chamber, where the pressure is 2 - 6 $\times 10^{-6}$ Torr. Note that the diffuse cone is primarily made up of krypton in the ground state, with only a small fraction of Kr*, as described in Section 2.2.2. However, any laser light we shine in at 811 nm will only scatter off the Kr*, so we are not worried about losing laser light to absorption by all of this ground state krypton.

We shine in laser light 0 MHz detuned (on resonance) from the trapping transition of the isotope we wish to trap, with the goal of pushing the Kr* from a cone shape into a collimated atomic beam for slowing and trapping. Recall though, that the scattering force is reduced by having a larger detuning term, which on resonance (where $\omega = \omega_0$) is simply

$$\delta = \omega - \omega_0 + \mathbf{k} \cdot \mathbf{v} = \mathbf{k} \cdot \mathbf{v} \tag{2.4}$$

Consider the effect of this term, setting $I = I_{\mathrm{sat}}$. If the laser light is perpendicular to the velocity of the atom, the detuning is zero, but if the laser light is even 1 degree off the perpendicular the scattering force is already reduced by a factor of 2 and by 10 degrees we have lost nearly an order of magnitude. Hence, if we are zero detuned, we are intending to strike the atoms we want to slow perpendicular to their velocity vector. So we bring in the laser light at an angle to the window so as to hit normal to some wide angle of the cone as shown in Figure 2.7, which scatters off the Kr* traveling along that velocity vector, pushing them in toward the center, reducing their angle and removing them from resonance. When

the beam reaches the other side of the chamber it hits a slightly titled mirror as shown and makes another pass, but now at a slightly shallower angle. The result is that light is scattered off a narrower section of the cone, before it hits a mirror across the way, and then scatters off a narrower section of the cone still. During each iteration, the krypton pushed in from the previous edges is ideally pushed into the next slice of excited velocity vectors, pushing the Kr* ever closer to having velocity vectors parallel with the beamline. By bringing in beams along both the vertical and horizontal directions, we can ultimately collect a majority of the Kr* into a forward-traveling collimated beam. This transverse cooling method (35) usually requires that order 10 bounces occur in order to achieve collimation (36). We use a combined 1 W of power for these beams in both transverse directions and apply the first three repumping sidebands for each isotope. The intensity of the beam in each dimension is about 75 mW/cm^2. The transverse cooling stage enhances our loading rate by a factor of 150.

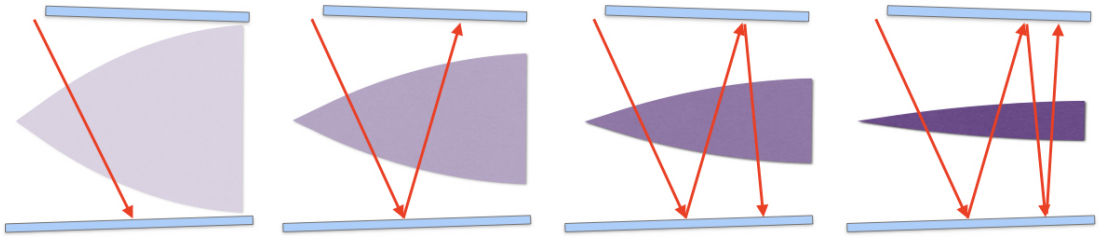

Figure 2.7: A diagram to describe how transverse cooling functions. The laser light initially strikes normal to a wide angle of the atomic cone, narrowing it. When the beam hits a mirror, we have the addition of a second ray, but with a more shallow angle, reducing the angle of the cone that is resonant with the light, and producing further narrowing. Each subsequent bounce produces a new, shallower ray, and the process recurs to push to cone into a narrow and forward-collimated beam. The magnitude of increasing shallowness with each reflection is exaggerated in the diagram for the purpose of demonstrating the effect to the reader. As such, the number of bounces shown is too few to achieve collimation as further bounces have been omitted for clarity.

2.2.4 2D focusing (2D magneto-optical trap)

The principles behind the magneto-optical trap (MOT) (37) require us to briefly review Zeeman splitting of atomic energy levels in the presence of a weak magnetic field. This effect

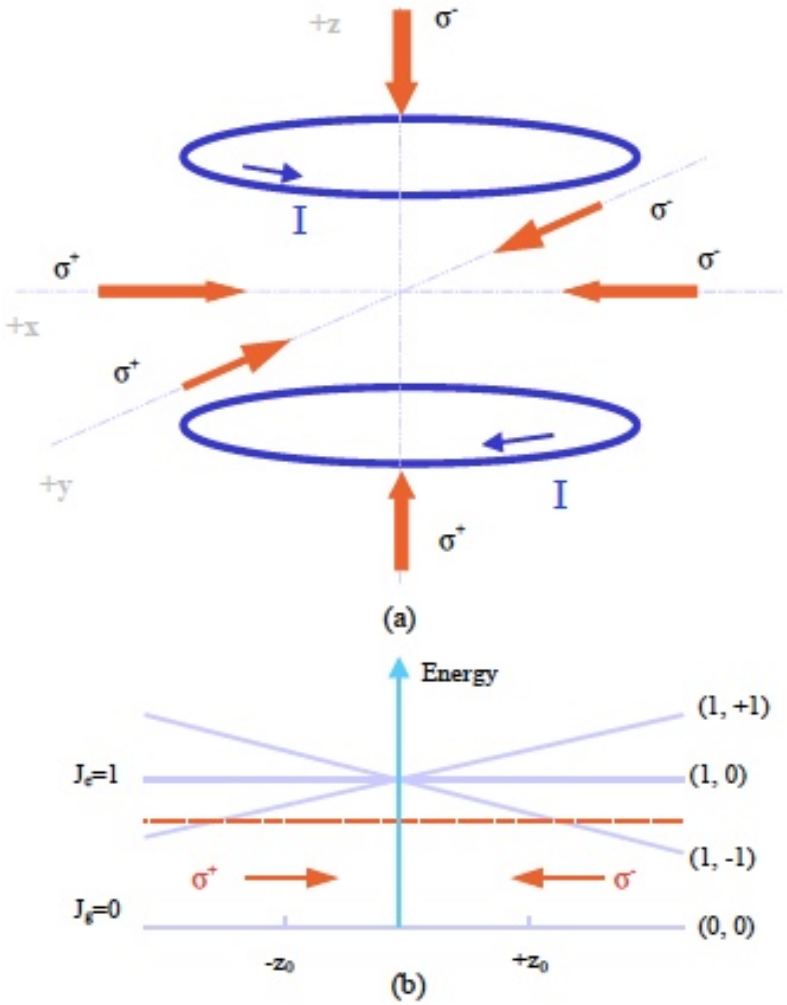

Figure 2.8: (a) A diagram of a three-dimensional magneto optical trap. The anti-Helmholtz coils provide a quadrupole magnetic field. Laser light is brought in from both directions on each axis with either right or left circular polarization. (b) The magnetic sub-level Zeeman splitting of a hypothetical atom's energy levels is plotted along the vertical versus the atom's position along the z-axis of our trap plotted on the horizontal. The dashed line marks the energy of our laser, which is brought in with different circular polarizations from the left and right. Figure reproduced from (30).

occurs based on the alignment of the angular momentum of the atomic levels **J** with the magnetic field. Each split state is then associated with its projection along the magnetic field, defined by m_J. Consider two levels: $J_g = 0$, the ground state of a two-level system, and $J_e = 1$, the excited state. Then we have a weak magnetic field produced by a pair of anti-Helmholtz coils, as shown in Figure 2.8 (a). The splitting and shift of the energy levels as an atom is moved along the z-axis due to the magnetic field is shown in Figure 2.8 (b). Also shown in Figure 2.8 (b) is an line representing the frequency of our laser, which has been purposely shifted below the trapping transition. As a result, only one set of states is on resonance with the laser when it drifts along the z-axis. We make use of this fact by sending in circularly polarized laser light in opposite directions along the axis. Each polarization will only pump light from a certain magnetic sublevel due to angular momentum selection rules. So, when the atom travels to the position $+z_0$, the state $m_J = -1$ becomes on resonance with the laser, and due to selection rules for that state will absorb significantly more of the σ_- photons, which push it to the center, than σ_+, which push the other way, resulting in a net push to the center. At the position $-z_0$, just the opposite happens.

With this knowledge in hand, we return to ATTA-3, where our collimated beam of Kr* is entering the 2D focusing chamber. Here we apply a two-dimensional MOT, using anti-Helmholtz coils to produce our magnetic field, and then shine in circularly polarized light at -6 MHz with respect to the trapping transition in the horizontal and vertical transverse directions. The collimated beam is moving perpendicular to all of the beams so the Doppler shift need not be considered. The effects of the MOT cause the beam to be "focused" in the transverse direction, pushing the edges of the collimated beam toward the center of the trap, and not effecting those atoms at the center of the beam. The goal is that with this push, the majority of the atoms in the beam will reach the center of the atomic beam axis once the atomic beam arrives at the end of the beamline, allowing us to trap them in a single spot.

200 mW of light are produced from the tapered amplifier for this section, and two re-pumping sidebands are added to the beam for each isotope. The intensity of the beam is 9

mW/cm^2 in each dimension. The 2D MOT improves the loading rate by a factor of 3.

2.2.5 Longitudinal slowing

Ideally, we have now taken care that the Kr^* in our atomic beam end up in the center of the atomic beam axis by the time they reach the end of the beamline. So the transverse directions are handled. What remains is to slow the atoms in the longitudinal direction so that they actually are slow enough to stop in our trap. To do so, we make use of the Zeeman shift effect in the thus aptly named Zeeman slower (38).

Obviously, there is quite a significant Doppler shift to contend with when we shine in a counter-propagating beam of light along the longitudinal axis. Now, we could shift the beam frequency to compensate, but as the velocities change from slowing, so will the Doppler shifts, and we'll have to continuously alter our frequency to handle that change. In slowing the beam using this method, it is impossible to slow a continous beam for capturing.

Thus we instead apply a magnetic field throughout the slowing region to make use of the Zeeman shift in the atom $\mu' B(x)$. Here the x-axis is the longitudinal axis and $\mu' = (g_e m_e - g_g m_g)\mu_B$, where the subscripts g and e refer to ground and excited states, g is the Lande g-factor, μ_B is the Bohr magneton, and the m values again, correspond to the alignment of the angular momentum of the atom with the magnetic field. We want use this shift to compensate for the Doppler shift $\mathbf{k} \cdot \mathbf{v} = \hbar k v(x)$, where

$$v(x) = v_0 \left(1 - \frac{x}{L_0}\right)^{1/2} \tag{2.5}$$

in order to assure constant deceleration such that the atoms are cooled continuously together, where v_0 is the initial velocity of the atoms, and L_0 is the distance over which we are stopping them. Setting the Zeeman shift and the Doppler shift equal and solving results in

our requiring a magnetic field profile

$$B(x) = \frac{\hbar k v_0}{\mu_B}\left(1 - \frac{x}{L_0}\right)^{1/2}. \tag{2.6}$$

We apply this profile on our Zeeman slower using a tapered solenoid seen in Figure 2.3. Notice that the tapering for the ATTA-3 slower does not actually end at its narrowest point–the point of zero field–but rather reverses to continue to produce some negative field in the region where the atoms are travelling slowest (i.e. have a very small Doppler shift). This style of slower allows us to offset the laser frequency of our slower from being on-resonance with the atoms. Conversely, if the zero field were at the end of the slower, than the beam would have to be quite close to resonance and could push the atoms while they were in the zero-field region of our 3D MOT.

We require 100 mW for the slower after some power has been used for stabilization (an improvement described in Section 3.3.1). The beam does not contain any sidebands for repumping due to the large shift of all the hyperfine lines (caused by the large magnetic fields) which may cause some unwanted atom state transfer from the repumping beams. The slowing beam intensity is 8 mW/cm^2. The slower is a truly crucial piece of the system, improving the loading rate by four orders of magnitude.

2.2.6 3D magneto-optical trap and single atom detection

Thanks to all of the pieces of the beamline that have come before, our atoms should be headed towards the center of the trap in the transverse directions and slowed to the center of the trap in the longitudinal direction. Now we simply have to trap them. To do so we employ the magneto-optical trap described in Section 2.2.4, but in three dimensions; our 3D MOT. Here we require about 300 mW of light in order for each dimension of our MOT to have 15 mW/cm^2 available. Three repumping sidebands are added to the beam. The pressure in the chamber during a measurement is typically 7 - 9 $\times 10^{-9}$ Torr.

Once the atoms are in the 3D MOT, we need only to detect them. For ^{81}Kr and ^{85}Kr the low-abundances result in only order 1 atoms being present in the trap at the same time, which we can detect by the use of a sensitive charge-coupled device (CCD) camera. We employ an Andor Luca-R camera to do so, along with a microscope made up of four aspherical lenses, one pair with 50 mm focal lengths and a second pair with 20 mm focal lengths, to collect the photons. The camera has an 8mm x 8mm sensor region with 1000 x 1000 pixels of 8 micron size. Thermoelectric cooling keeps the camera at -20 ^{o}C to suppress noise from dark current. The Luca-R is also equipped with electron multiplier technology (EMCCD) which increases the magnitude of weak signals significantly above the readout noise of the detectors, thus suppressing that instrumental background as well.

For our single atom detection method, we employ a beam chopper between the transverse cooling and 2D focusing stages which dictates the length of the 440 ms cycle during which the atoms are collected, detected, and then removed from the trap.

During collection, the atomic beam is passing through to the trap, the Zeeman slower is active, and the MOT beams are at full power. This stage lasts 330 ms. Then, during detection the atomic beam is blocked by the chopper, the Zeeman slower is inactive, and the MOT beams are set to 25% of their full power. Unfortunately, at full power, the background light is too high compared to the fluorescence of the atoms and cannot be spectrally filtered out since the atoms fluoresce at the same wavelength as the MOT beams. At low power, however, single atoms can be seen quite clearly as shown in Figure 2.9. When we lower the power, we also change the current in the 3D MOT anti-Helmholtz coils to increase the magnetic field gradient and thus "tighten" the trap to better confine the atoms to a single location. By integrating the photons over the region of interest where we expect the atoms to end up (about a 100 x 100 μm spot with the increased field gradient) we get a signal that is nicely quantized by atom number allowing us to quite literally count the atoms in our trap. The atoms are detected in a single frame over an exposure time of 50 ms.

For the removal stage, we use 10 mW of laser light at 810 nm pulsed for 10 ms to excite the

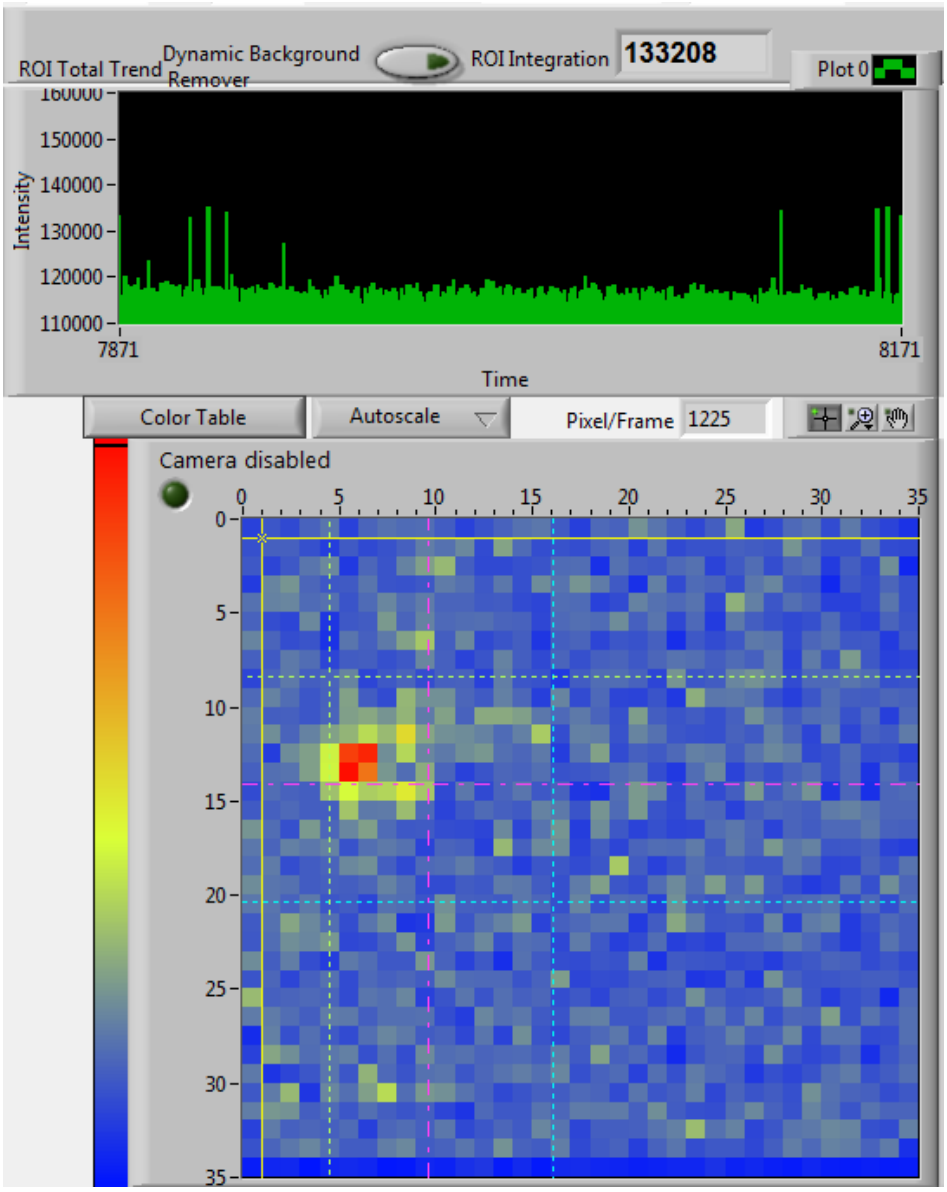

Figure 2.9: A false color image of a single atom in our MOT taken using a sensitive CCD camera as shown on our LabView program during measurements. The full image shown is 1400 x 1400 microns. Above the atom image is a timestream of integrated photon signal from the region of interest marked by the intersection of the blue and yellow dotted lines on the false color image. The spikes in the signal mark the appearance of an atom in the trap.

atoms from the lower-level of the trapping transition to a separate excited state ($5p[5/2]_2$, see Figure 2.5). From this excited state, they are no longer in a closed cycle with the metastable state and can decay toward the ground state (along the 877 nm transition shown in Figure 2.5, which has a 3 to 1 branching ratio versus the transition falling back into the metastable state), meaning our trap light no longer affects them. The light is technically on resonance for ^{83}Kr, but due to the frequency tails of the beam ^{81}Kr and ^{85}Kr atoms are also excited. This excitation obviously occurs at a severely reduced rate due to the reliance on the tails, but excitation only takes one or two cycles to work, unlike scattering and detection which requires millions of photons. We thus remove the atoms through this "quench transition" with this "quench" beam so that we don't count them again during the next collection and detection cycle.[6] After the removal the cycle begins again with collection.

The timing for the camera and laser actions is controlled by a small diode laser which passes through the system from a window behind the RF source and passes out through the end of the trap where the Zeeman slower beam is injected. The laser light from this small laser, which is being chopped by the beam chopper, is detected there by a photodiode. Thus the signal on the photodiode acts as the master clock/trigger for the system's digital controls.

So by knowing how long we load for and how many atoms we count when we are loading, we produce a loading rate for ^{81}Kr and ^{85}Kr in the ATTA system, which is crucial for how we determine ^{81}Kr/Kr and ^{85}Kr/Kr relative isotopic abundances.

Note that atoms can be knocked out of our trap by collisions with background gas. The time constant for this loss is determined by the background gas pressure and composition. Under typical conditions the lifetime is approximately 1 - 2 seconds with our background gas pressure of 1×10^{-8} Torr. While this is longer than our cycle time, it can (and does) produce a small systematic effect, which we will mention in Section 2.4 and address more

6. Readers who may feel discomfort at the qualitative assumption that we will successfully remove the atoms using the frequency tails of the beam should see Section 3.3.4 for a further examination of this issue.

fully later in Section 3.4.2.

2.2.7 Stable nuclide detection via ion current

The technique described in this Section to measure stable isotope loading rates is described in Jiang's report on ion collection as a measure of a metastable MOT in (39). This Section closely follows the discussion in (39).

We've managed in Section 2.2.6 to detect ^{81}Kr and ^{85}Kr in our trap and measure the loading rate of those radioactive nuclides into that trap. However, the loading rates are not constant throughout a single run, chiefly due to natural drifts in gas pressure. As such, we need some signal to normalize against; a signal which drifts with the loading rates of the radioactive nuclides but, unlike the radioactive nuclides, does not depend on the krypton gas sample being measured. For this purpose, the loading rate of the stable isotope ^{83}Kr will function quite nicely.

Unfortunately, measuring a stable isotope the same way as the radioactive nuclides is impossible. Because the stable nuclides are $10^9 - 10^{11}$ times more abundant than the radioactives ones, their loading rates are commensurately higher. Obviously, we thus need a different measure of the loading rate from single atom counting.

When the stable Kr* isotopes are continuously loaded into the trap, they collect and form what we call a "metastable MOT" of atoms, where dynamics for the number of atoms $N(t)$ is given by

$$\frac{dN(t)}{dt} = L - \gamma N(t) - \beta \int_V n(r,t)^2 dV. \tag{2.7}$$

Here, L is the loading rate we wish to measure. The other two terms are loss mechanisms. The first, $\gamma N(t)$, is the loss due to limited trap lifetime, which is primarily caused by collisions with background gases as mentioned in Section 2.2.6, where γ is a constant dependent on the vacuum pressure and background gas composition in the chamber. The second term comes from two-body losses, determined by some constant β based on the strength of the

loss mechanism, as well as the size and shape of the trap, represented by the integral of the atom density over the volume of the trap, which determines the likelihood of the atoms in that trap colliding into one another. With enough atoms in the trap, these two-body losses swamp the background gas loss. If we consider this large MOT scenario in the steady-state situation, $\frac{dN(t)}{dt} = 0$, where the loading rate and loss mechanisms have come into equilibrium, then equation 2.7 becomes

$$\begin{aligned} 0 &= L - \gamma N(t) - \beta \int_V n(r,t)^2 dV \\ L &\approx \beta \int_V n(r,t)^2 dV. \end{aligned} \tag{2.8}$$

Thus, if we can measure the two-body loss rate in this scenario, then we will have a measure of our loading rate. So what happens when two Kr* collide in our MOT? The interaction results in one of two outcomes: (1) Penning ionization or (2) associative ionization

$$(1) \quad \mathrm{Kr}^* + \mathrm{Kr}^* \rightarrow \mathrm{Kr} + \mathrm{Kr}^+ + e \tag{2.9}$$

$$(2) \quad \mathrm{Kr}^* + \mathrm{Kr}^* \rightarrow \mathrm{Kr}_2^+ + e. \tag{2.10}$$

As the reader may notice, both of these interactions produce one positive ion. By measuring these ions, we thus have a measure of the loss rate, which, by equation 2.8 is a measure of our loading rate in the large MOT approximation. During the capture of the stable isotopes we do not lower the MOT power or insert the quench beam, since we are interested in just measuring the steady state ion signal. It takes about 100 ms to reach the steady state. To measure a background on this signal, we measure the ion current with the slower beam blocked (since it quenches the loading rate by four orders of magnitude). The valid range of this method is shown to require that there are 10^8 - 10^9 atoms in the trap (corresponding to 0.1 - 10 nA of current).

To measure these ions in practice, we employ four half-ring-shaped electrodes shown in

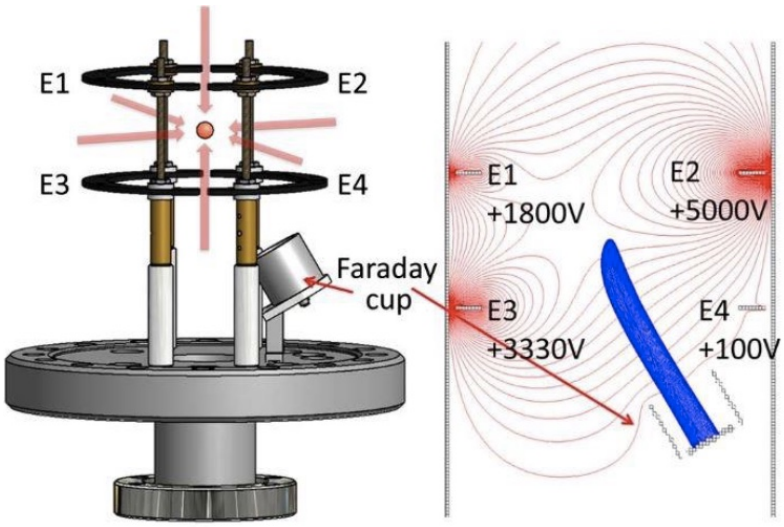

Figure 2.10: The electrode and Faraday cup positions in the MOT for ion collection. Voltages are applied to four half-ring electrodes in the orientations shown. The left diagram is a drawing of the electrodes within the vacuum system. The image on the right is a simulation in SimIon of the electric field lines (red) and the ion paths as they travel in the field (blue). Reproduced from (39).

Figure 2.10. The voltages on these electrodes create an electric field which guides the ions to a Faraday cup where the current is electronically amplified and converted to a voltage for us to measure. The voltages shown in Figure 2.10 are from a simulation, and in practice must be optimized depending on the position of the metastable MOT.

So now we have a loading rate for our radioactive as well as our stable nuclide, which we can use to normalize ^{81}Kr and ^{85}Kr signals in a given sample.

2.2.8 Open mode and closed mode vacuum configurations

Before we finally move on to describing how a measurement is conducted, it would be helpful to have a slightly more in-depth understanding of the how the vacuum system of our beamline is configured.

One of the major goals in improving ATTA has always been reducing the sample size of krypton gas required, as noted in Section 1.2. We currently claim to be able to measure samples of about 10 μL of krypton gas. However, if we just released 10 μL of gas into the system, attempted to measure it, and then pumped it away, we'd be lucky to see even a

handful of atoms before the gas ran out order tens of seconds later, primarily due to the low efficiency with which the discharge produces Kr*.

So we had to concoct a way to keep counting that same gas. We do this by recycling the gas in the "closed mode" configuration of our vacuum system. The beamline is designed to make this a rather simple process. There are three magnetically levitated turbomolecular pumps which are meant to remove gas from the system and keep it under vacuum,[7] one on the 3D MOT chamber, one on the beam chopper chamber, and one on the transverse cooling chamber. The outlet of the one in the 3D MOT chamber goes into the beam chopper chamber, and the outlet of the one in the beam chopper chamber goes to the transverse cooling chamber as seen in Figure 2.11.

When we are not measuring, and the system is thus in an "open mode" configuration, the transverse cooling chamber outlet is backed by a small turbomolecular pump which is backed by a dry roughing pump that leads to atmosphere. When measuring, we wish to recycle the gas by entering the closed mode. To do so we can valve off the outlet to the small turbomolecular pump and open a path from the transverse cooling chamber pump back to the inlet of the RF source, as seen in Figure 2.11. Even in this configuration, the system holds vacuum quite well (pressure rise in the transverse cooling chamber $< 5 \times 10^{-8}$ Torr/hr) for the duration of the measurement thanks to the lubricant-free nature of the magnetically-levitated pumps as well as the presence of an internal getter pump, which removes reactive gases, but not noble gases.

2.3 Measuring a sample for ^{81}Kr/Kr and ^{85}Kr/Kr relative isotopic abundances

This section provides a practical walkthrough of the typical procedure to measure a krypton sample. The settings for all specific instrumentation mentioned appear in Appendix A.

7. We make this caveat because there is another turbomolecular pump in the beamline that we will discuss in Section 3.1, which exists for a different purpose.

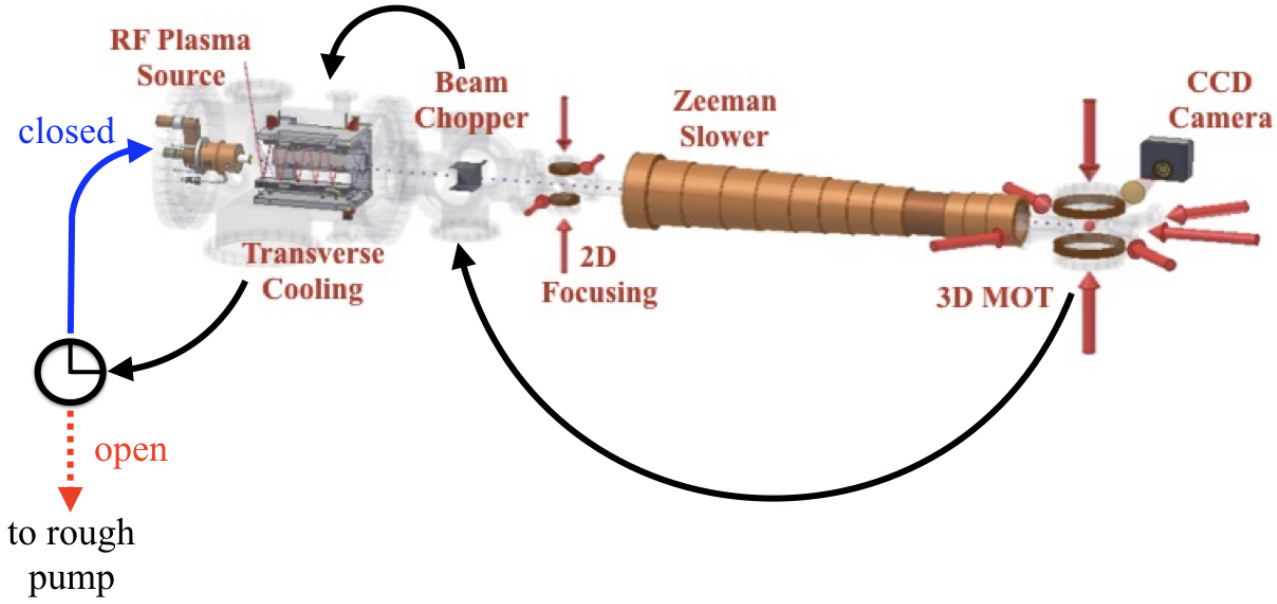

Figure 2.11: A schematic detailing how gas is recirculated in the system in the open and closed modes. In both modes, gas is pumped backward along the black arrows. After being pumped from the transverse cooling chamber the gas can be redirected into the source in the closed mode as shown (blue solid arrow), or ejected from the system in the open mode (dotted red arrow) if we were to change the orientation of the valve diagramed. Note, the valve is a schematic representation of pair of valves which are used to ultimately produce the same effect.

First, the RF source requires cooling down with ℓN_2 from room temperature to 100 K. The process takes approximately one hour. In the meantime, the remainder of the system is prepped by activating the tapered amplifiers, high voltage for ion collection, and power supplies for coils that provide the various magnetic fields (and a chiller to cool the highest power supply). The ECDLs are typically left on continuously barring maintenance. The tapered amplifiers require a few minutes to temperature stabilize, after which point the optics are tuned to ensure that the output from the amplifiers and fiber-optic couplers are optimized. Afterward the stabilizations for the Zeeman slower (Section 3.3.1) and the MOT beam power switching (Section 3.3.3) are engaged and both primary lasers (trap and quench) are locked to the error signals from their respective spectroscopy setups (the discharges for both spectroscopy setups are always left running, although occasionally require tuning to produce a better signal for locking). Then we activate the voltage-controlled oscillators (VCOs) which provide the frequencies to our EOMs for sideband production for repumping.

The EOMs and AOMs themselves are left active typically, as are the digital synthesizers that provide the frequencies for shifting via the single pass AOMs. That takes care of the optics.

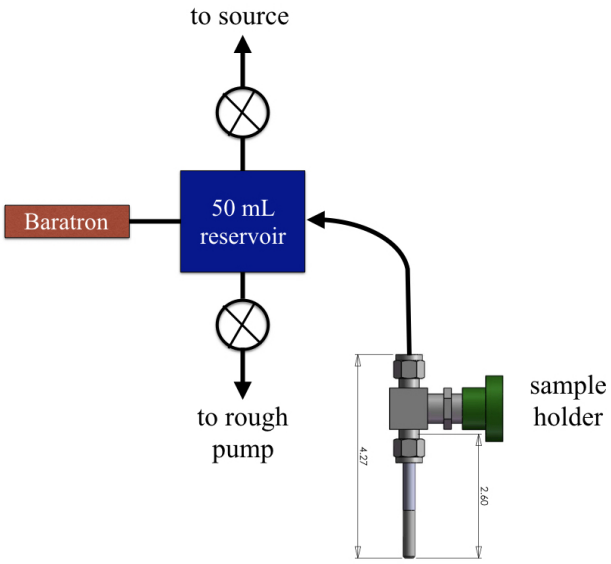

Figure 2.12: A schematic for the reservoir system, including a mechanical drawing of a typical sample holder. The gas from the sample holder is injected into a 50 mL volume where the pressure measured by the Baratron allows us to determine the gas volume of the sample. From the 50 mL volume the gas can be injected into the system using a leak valve. The dimensions on the sample holder are given in inches. The remainder of the drawing is purely diagrammatic and not to scale.

On the vacuum side of the system we need to attach the sample we wish to measure. The sample is typically 10 μL of krypton gas at STP in a short, 1/4" stainless steel tube only a few inches long, which contains activated charcoal–originally used to trap the gas in the tube–packed under steel wool and capped with an SS-4H Swagelok valve. This sample is attached to a 50 mL reservoir with a Baratron gauge, which, by measuring the pressure, can measure the volume of our sample. A diagram of this reservoir, along with the drawing of a typical sample holder, can be seen in Figure 2.12.

Once the system is cooled to 100 K, we inject the sample into the reservoir by heating the steel finger with a heat gun for two minutes to avoid mass fractionation of the sample as it fills the reservoir. Then we activate the beam chopper and the small diode laser which acts as the master clock. Finally, just before we begin, we switch the system into the closed

mode, described in Section 2.2.8.

Once in the closed mode, we leak a small amount ($\sim$ 1 μL of Kr) into the system while we run a mass scan on our Residual Gas Analyzer (RGA 100, Stanford Research Systems), in order to measure the composition of our sample. Then we open the source to the aforementioned getter pump, which removes many common non-noble gas contaminants (that haven't been frozen out by the lower temperatures) and helps to remove the molecular nitrogen and oxygen that very slowly leak into the system in the closed mode. Then we inject another 5 - 7 μL of Kr gas from the sample into the system and activate our RF discharge. Then, if all is well, Kr* is produced and we start trapping it.

For running the majority of the measurement as well as data collection, we rely on a LabView program. This program cycles the laser frequencies to cover all of the isotopes. The typical cycle is 5 minutes long with 3.5 minutes is spent on ^{81}Kr, 1 minute on ^{85}Kr, and 0.5 minutes on ^{83}Kr (the first 10% of which is used to measure the ion background mentioned in Section 2.2.7) before the sequence repeats. At the beginning of each isotope's turn, the program checks to ensure that the VCOs controlling the main frequency via the DPAOM and the EOM sidebands are in the right place, and if they are not, it corrects them. The measurement typically lasts for 2 - 4 hours, depending on the abundances (lower abundances mean fewer statistics, which means longer runtime). As mentioned in Section 2.2.2 the RF discharge ionizes some of our atoms. These ions subsequently have enough energy to then be implanted in our chamber walls, causing some sample loss over time.[8] To offset this effect, provided there is sufficient sample, we typically inject another 2-3 μL of Kr after an hour of measuring time, thus maintaining optimal discharge conditions and maximum detection efficiency.

Once the measurement is complete, while we may feel rather accomplished, we are unfortunately not finished. We want to measure the relative isotopic abundances for ^{81}Kr/Kr and ^{85}Kr/Kr, and we have measured the loading rates of ^{81}Kr, ^{85}Kr, and ^{83}Kr on the ATTA-3

8. More on the other consequences of this issue in Section 2.5.

beamline. Now, ideally we could take the ratio of the ^{81}Kr loading rate and ^{83}Kr loading rate, say, and that would give us the isotopic abundance ^{81}Kr/Kr. But for that we need to know ATTA's efficiencies for counting ^{81}Kr and ^{83}Kr, call them ϵ_{81} and ϵ_{83}, respectively. For that we need some standard reference. However, after measuring that standard reference once, we then require that these efficiencies don't change. They will. Not by more than a few percent over a couple of weeks maybe, but still they drift. This is due to temperature and humidity fluctuations in the laboratory, as well as slight shifts in the plasma efficiency. So, to ensure we have the most precise possible measurement, we actually measure our standard reference gas daily after each measurement, which takes another 2 - 3 hours.

Because we have liters of reference gas that we can continually feed into the system, we do not need to conduct the measurement in the closed mode. Due to this fact (and the cross-sample contamination effect that we will discuss in Section 2.5) we instead conduct the measurement in the open mode, using tens of mL of reference gas (STP). Besides the change in vacuum configuration, the process is the same as for the sample portion of the measurement. Then, with the loading rates for our sample and our reference measured, we define a superratio (SR) for ^{81}Kr and ^{85}Kr

$$^{81}\mathrm{Kr}_{\mathrm{SR}} = \frac{^{81}\mathrm{Kr}_{\mathrm{Sample}}/^{83}\mathrm{Kr}_{\mathrm{Sample}}}{^{81}\mathrm{Kr}_{\mathrm{Reference}}/^{83}\mathrm{Kr}_{\mathrm{Reference}}} \tag{2.11}$$

$$^{85}\mathrm{Kr}_{\mathrm{SR}} = \frac{^{85}\mathrm{Kr}_{\mathrm{Sample}}/^{83}\mathrm{Kr}_{\mathrm{Sample}}}{^{85}\mathrm{Kr}_{\mathrm{Reference}}/^{83}\mathrm{Kr}_{\mathrm{Reference}}} \tag{2.12}$$

which represent the isotopic abundances with respect to our standard (i.e. the relative isotopic abundances) and no longer rely on ϵ_{81} and ϵ_{83} (they canceled out from being present in both the numerator and denominator). And since our standard contains what we consider

to be the constant and modern value for ^{81}Kr/Kr in the atmosphere,[9] we know that

$$^{81}\mathrm{Kr}_{\mathrm{SR}} = 2^{-(t_{^{81}\mathrm{Kr}}/t_{1/2})} \tag{2.13}$$

where the $t_{^{81}\mathrm{Kr}}$ is the ^{81}Kr-dating age of our sample and $t_{1/2} = 229 \pm 11$ kyr, the half-life of ^{81}Kr.

For ^{85}Kr measurements, we can actually report our results in the more common units of decays per minute per cubic centimeter of krypton at STP (dpm/cc) by calibrating ATTA-3 against LLC results for a set of prepared calibration samples. And not only does this offer us a reporting standard, but it demonstrates the linearity and reliability of ATTA by comparing it to an already proven method. This was demonstrated by double-blind test in (23), but is consistently re-checked with each major upgrade or alteration to the system. The most recent calibration occurred on April 2016, after all of the major upgrades described in this dissertation. The results are shown in Figure 2.13.

2.4 Data analysis

In this Section we give an overview for the analysis used to produce ^{81}Kr and ^{85}Kr superratios from the data collected on the ATTA beamline. This analysis is primarily done on a Wolfram Mathematica notebook which is included in Appendix B. The graphs reproduced from the notebook are typically in arbitrary units defined by the instrumentation, unless otherwise stated.

The data collected on LabView from the ATTA beamline consists of three pieces, one for each isotope measured (^{81}Kr, ^{85}Kr, ^{83}Kr). The data for ^{81}Kr and ^{85}Kr is simply the integrated photon signal over the region of interest on the CCD camera taken over time as shown earlier in Figure 2.9, but shown again here for both isotopes over an entire run as the

9. More on the validity of this statement in Chapter 4.

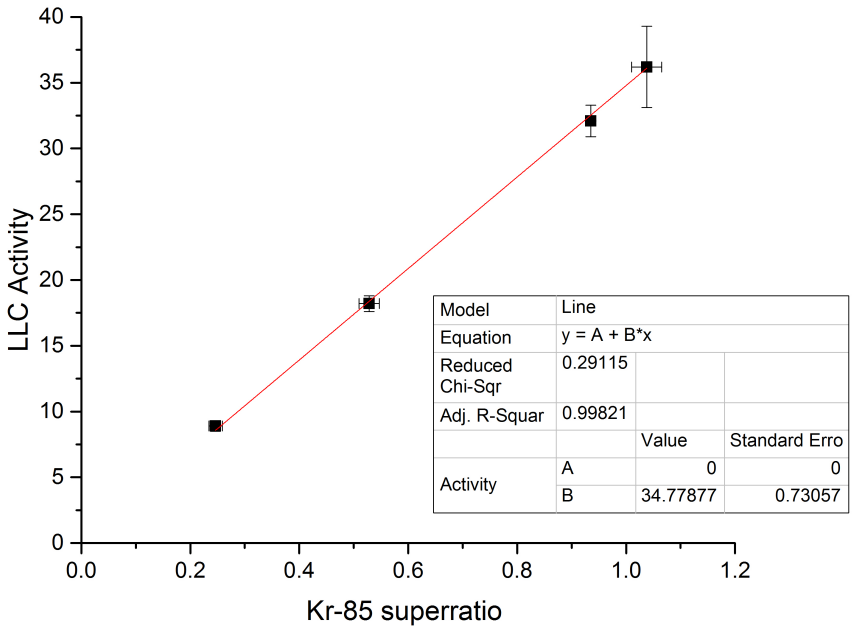

Figure 2.13: The LLC activity of four calibration samples prepared at the University of Bern versus the ^{85}Kr superratio measured on ATTA in April 2016. The fit is forced through zero because of a fifth calibration sample which was measured to have a ^{85}Kr activity below the detection limits of both LLC and ATTA. The good fit demonstrates the linearity of the ATTA method.

data appears when collected and stitched together on Mathematica in Figure 2.14.[10]

For ^{83}Kr, we collect the voltage produced from the current amplifier which takes the Faraday cup as its input. There are two components to these data: signal when the metastable MOT is being loaded and background when the metastable MOT is not present. Each piece is stitched together independently and jumps at the endpoints are removed to produce the data shown in Figure 2.15.

To produce the ^{83}Kr loading rate, we, at this juncture, simply subtract the average background from the average signal. To produce an error on that rate, we examine the standard deviation of a section of the signal where there are no discontinuities from where we stitched the data together while the pressure is still shifting due to the implantation of

10. Because the data is collected along a single timestream and the isotopes are switched through in five-minute cycles, we have to sew the data together in analysis to produce it for each isotope independently.

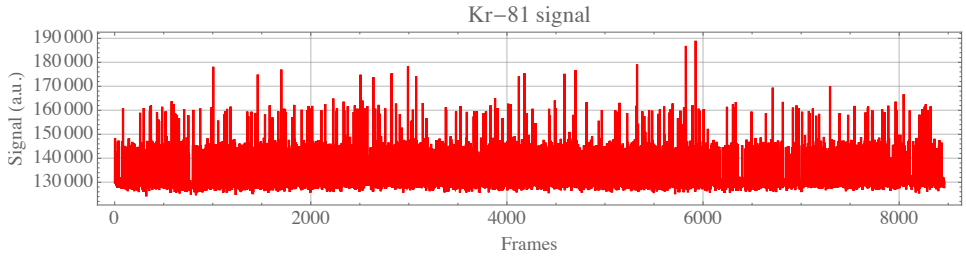

(a)

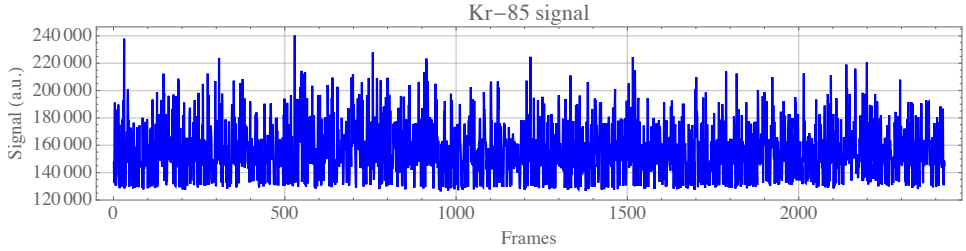

(b)

Figure 2.14: Integrated photon signal from the CCD camera of ^{81}Kr atoms (a) and ^{85}Kr atoms (b) over time.

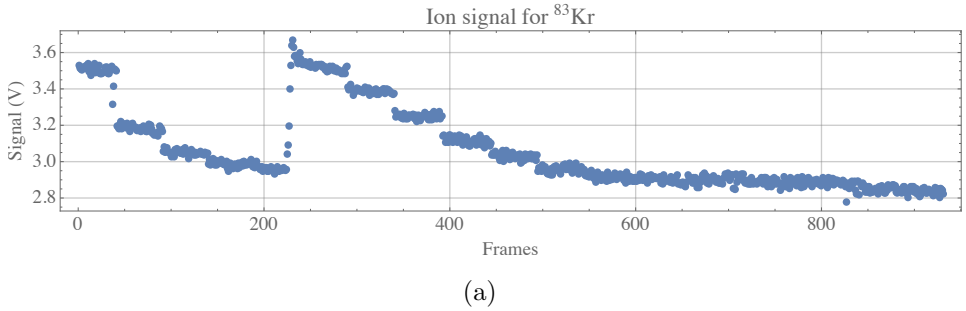

(a)

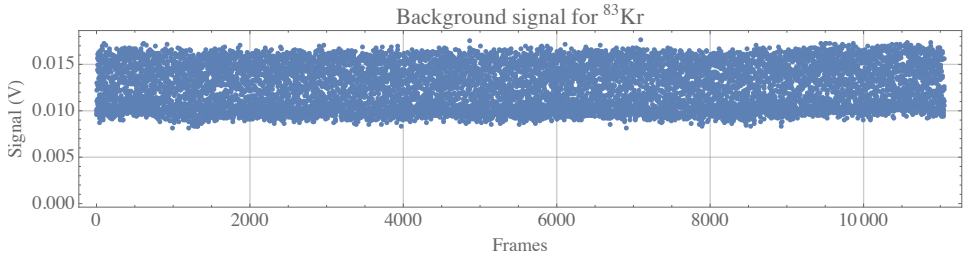

(b)

Figure 2.15: Collected ion signal from metastable ^{83}Kr atoms being loaded into the MOT (a) and the background signal of an empty MOT (b) over the course of a sample run, in volts.

krypton atoms in the system. This is permissible because we will take the ratio of this single averaged loading rate against a single averaged loading rate that we produce for ^{81}Kr and ^{85}Kr, and those loading rates correlate thanks to our short cycles. Moreover, when we take the data, we always ensure that we are measuring the ^{83}Kr when we begin the data taking, make any additional injections of gas, and end the data taking. That ensures that the ^{83}Kr's single averaged loading rate encompasses all the systematic changes for comparison with the ^{81}Kr and ^{85}Kr loading rates.

To produce the ^{81}Kr and ^{85}Kr loading rates, we do have to do a little more work though. First, we want to remove the background of the signal, which comes primarily from scattered laser photons, including any slow drifts located therein. To do so, we set a threshold on the data, about halfway between the obvious baseline and the one atom line, and select out all of the points below that as our "baseline". Obviously, that baseline may contain some data. However, since we are interested primarily in slow drifts, we put the baseline through what is effectively a low-pass filter, thereby creating a smoothed baseline by replacing every point with the average value of the ten points that come after it. And then we subtract this smooth baseline from the raw data. Next, we histogram that data, which results in Figure 2.16.

The peak around zero represents the background noise from laser photons (now set at zero because we subtracted out the baseline value), and each subsequent peak represents the trapping of one, two, three atoms, and so forth. Thus all we need to do is figure out how many counts are in each peak, multiply by the number of atoms that peak represents and that will give us the total number of atoms counted. Divide that by the time we spent counting each isotope according the the LabView program and we get a loading rate.

To analytically determine the number of atoms correctly we fit the histogram to a function $f(x)$ that is simply a series of Gaussians in the form

$$f(x) = A_0 e^{-\frac{(x-x_0)^2}{2a_0^2}} + \sum_{i=1}^{i=n} A_i e^{-\frac{(x-ix_s-x_0)^2}{2a_i^2}} \tag{2.14}$$

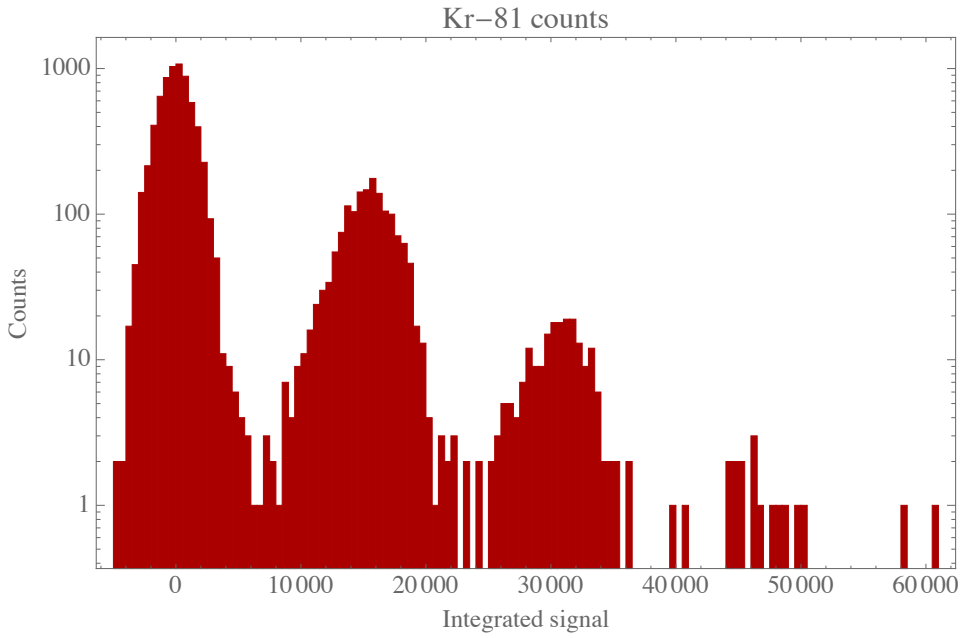

(a)

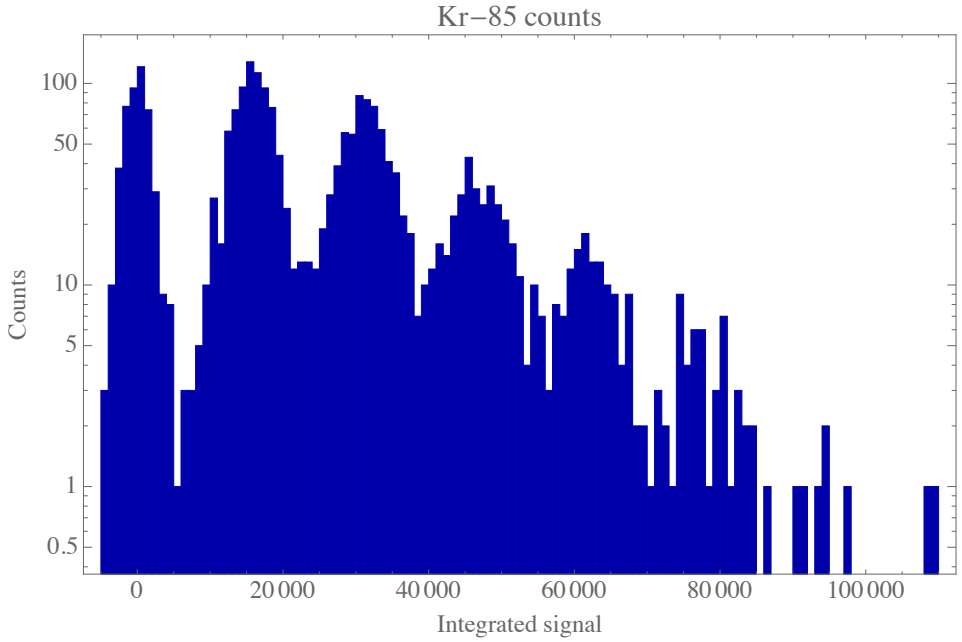

(b)

Figure 2.16: A histogram of the integrated photon signal data after background subtraction, representing atom counts for ^{81}Kr (a) and ^{85}Kr (b). Bin widths are 500 in terms of integrated signal.

where n is the number of peaks we are fitting and is input by the user before the fit is made. The remaining parameters are determined by the fit, with A_i as the amplitudes, x_0 the the center of the background peak, a_i the Gaussian widths, and most importantly, x_s as the "single atom height," i.e. what ought to be the center of each subsequent peak when considering the number of atoms that peak represents. With x_s determined, we assume that all counts between $x_s - 5a_1$ (representing a 5σ certainty that an atom was found in the trap) and $1.5x_s$ represent 1 atom, and that all those between $1.5x_s$ and $2.5x_s$ represent two atoms and so on. Such fits are shown in Figure 2.17.

There are two notes that must be made. First, cautious readers may remark that the photon distributions are governed by Poisson statistics, not Gaussian ones. However, this issue is ameliorated by the fact that each atom count actually represents the scattering of thousands of photons, which is more than enough for the Poisson statistics to be approximated by Gaussian curves.[11] The second note is that this assumption about our peaks being exactly equally spaced only holds true if we don't have any "fractional atoms." As noted in Section 2.2.6, the atoms have a lifetime in the trap determined by the likelihood of collisions with background gas. Now, there is unfortunately a chance that the atom can be knocked out of the trap during the camera's exposure time, resulting in significantly less than the typical number of photons being seen by the camera per atom. These show up as fractional atoms and produce an asymmetry in our Gaussian distribution. Luckily, especially when there are only one or two atoms being trapped at a time, this effect is small. But more importantly, this effect is not loading rate dependent and always present.[12] Thus, so long as we apply the same analysis method to our sample and our reference, the effect washes out by virtue of taking the superratio.

Once we have the number of atoms over the time spent trapping, we have our ^{81}Kr and ^{85}Kr loading rates to form a ratio with our ^{83}Kr loading rate, where the error on the

11. This issue of photon statistics should not be confused with the issue of atom statistics. The very few atoms we catch in our trap at a time are still very much governed by Poisson statistics.

12. However, there are unique situations that alter this fact, discussed in Section 3.4.2

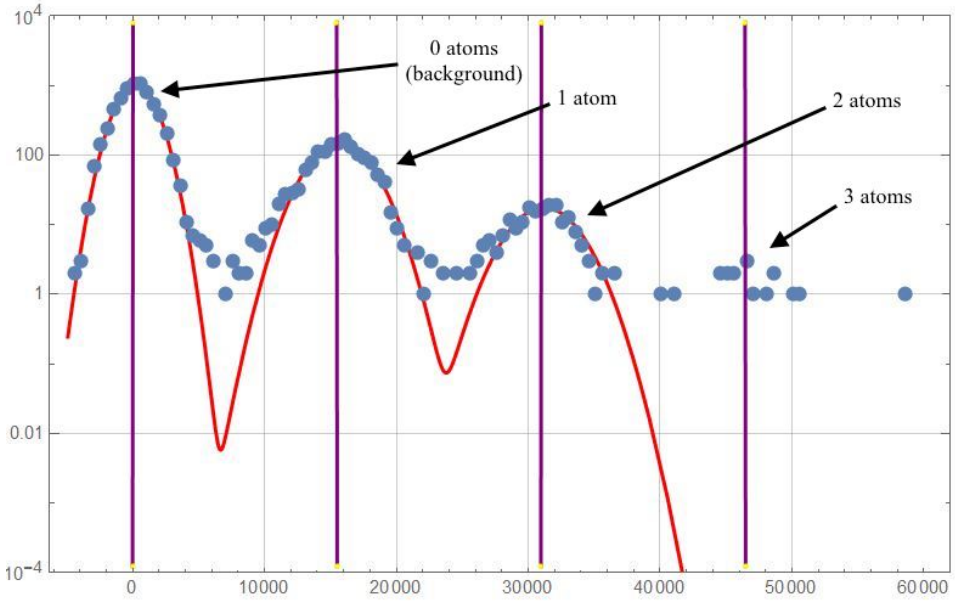

(a)

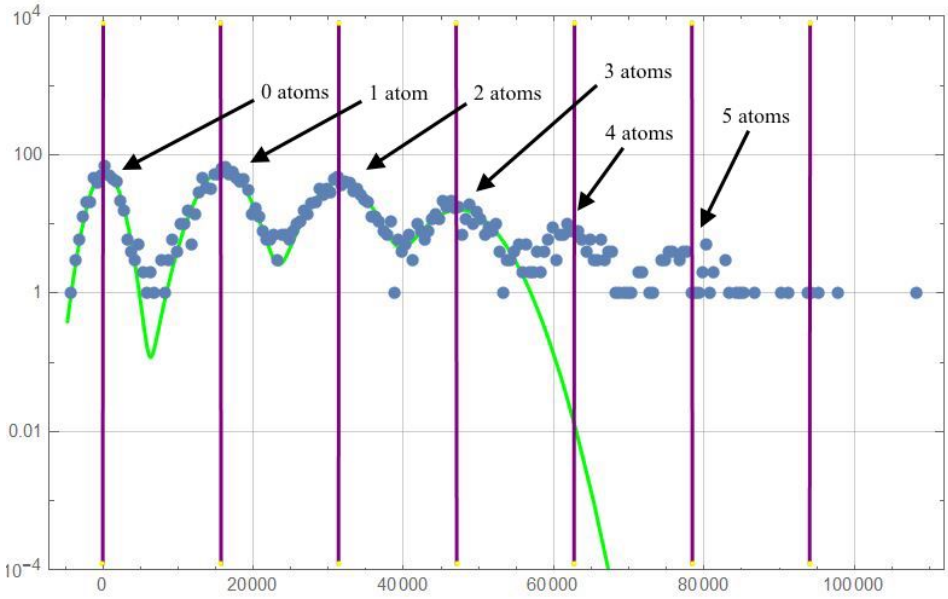

(b)

Figure 2.17: Fit of Gaussian functions to the histogram of the integrated photon data after background subtraction (seen in Figure 2.16) representing atom counts for ^{81}Kr (a) and ^{85}Kr (b). The fits are only done for two peaks in (a) and three peaks in (b), despite the labelled presence of further peaks. That is because fitting out to further peaks does not alter the value of the single atom height determined by the fit, which is the value we are interested in finding.

radionuclide loading rates is based simply on the error from counting statistics given the number of atoms counted in each case. As a check against the earlier mentioned issue of taking a single average value for the whole run, we also chop the data into three equal part and ensure that the loading rate is consistent throughout the measurement (fewer parts than three and the error bars due to statistics often get too large to be worth much in making such a comparison).

2.5 Cross-sample contamination corrections

There remains one final issue that we have not dealt with in our description of the current ATTA method, and that is cross-sample contamination. We noted this problem as part of the reason we conduct our reference measurement in the open mode configuration and it is currently the largest factor limiting the throughput of samples in the ATTA technique.

As described in Section 2.3, the krypton ions produced by the RF discharge can implant themselves in the chamber walls causing sample loss. However, this sample loss slowly tapers off as enough krypton is implanted in the walls near to the source to (nearly) come into equilibrium with the krypton remaining in the sample. That is, the rate that new krypton is implanted at this point is equal to the rate of krypton released, which is fine, provided that all of that krypton is from the current sample.

But consider when we finish measuring our first sample. We discard the remaining gas, but whatever is implanted in the chamber walls remains, and this is typically about 2-4 μL of krypton. Now, if we insert another 10 μL, these 2-4 μL from the previous sample will exchange with the new sample causing a significant contamination problem. That poses two questions: how do we measure the reference right after the sample with this contamination issue and how do we deal with the contamination in general for further sample measurements?

We have already answered the first question by measuring the reference in the open mode configuration. In doing so, we process more than 10 mL of reference gas, rather than 10 μL. So even though the sample krypton leaches out during the measurement, the amount is so

negligible ($< 0.1\%$) that no correction is needed. But afterward the problem still remains as the reference gas is newly embedded in the system in exchange for whatever sample leached out during the reference measurement.

So we strive to remove most of this implanted krypton by "washing" the system. We do so by running the RF discharge in an open mode configuration after the reference measurement, but while flowing a different noble gas, typically xenon, to replace the implanted krypton. This process currently takes 18 hours and still at this point there is a small fraction ($\sim 1\%$) of implanted krypton among implanted atoms in the system. This krypton will leach out during the next sample measurement and must be corrected for, but the effect is over an order of magnitude reduced thanks to the washing procedure.

We make a corresponding correction in two steps. First, we need to know how much krypton is leaching out. We determine this "outgassing rate" prior to each sample by running a discharge with xenon gas in the closed mode–before we cool down the system–and measuring how fast the stable isotopes of krypton collect in the system using the RGA. The outgassing rate that we get from the RGA needs to be multiplied by a correction factor to account for the fact that we are measuring the outgassing rate of krypton in the presence of a xenon discharge, but truly wish to know the outgassing rate of krypton in the presence of a krypton discharge.[13] That takes care of the how much krypton will build up during the measurement, but more importantly, we still need to know what the ^{81}Kr and ^{85}Kr superratios are for that contaminant.

The superratios of the contaminant evolve in a rather complex manner over time with the measurement of each new sample, and these changes are difficult to track and model. Now, we can actually measure them directly. We do so by continuing the wash after the first 18 hours, but in closed mode. Doing so for long enough eventually builds enough krypton in the system to do a direct (albeit statistically poor) measurement of the contaminant's ^{81}Kr

13. This factor is 2.0 for xenon, and the process by which we determine it is detailed in our more advanced contamination model in Section 5.3. Said model would be rigorously applied here if we did not enjoy the convenience of the approximation to be described now.

and ^{85}Kr superratios as if it were a sample. Unfortunately "long enough" requires over 24 hours of the beamline's time (beyond the washing procedure) and thus is not a regularly practical technique. However, because we measure the reference gas after each sample (and in the open mode, which in a sense, acts as a washing out of the sample krypton), we have ensured that the contaminant ^{81}Kr and ^{85}Kr superratios hew closely to the ratios of the reference gas, which allows us to make a more general approximation.

To prove this point, we directly measured the contaminant ratios three times, each after two weeks of sample measurements. These were environmental samples that contained little to no ^{85}Kr activity and had ^{81}Kr/Kr relative isotopic abundances ratios that ranged between 10 and 100 percent of modern krypton (i.e. had ^{81}Kr superratios between 0.1 and 1). The results of these measurements are shown in Figure 2.18.

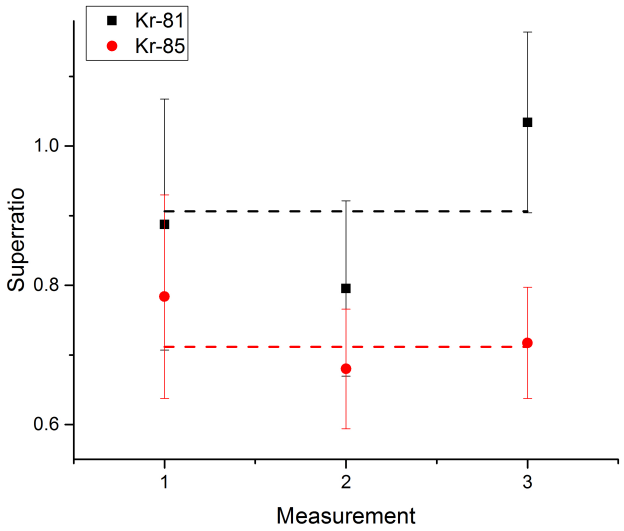

Figure 2.18: Directly measured contamination superratios for ^{81}Kr (black squares) and ^{85}Kr (red circles). Dashed lines represent constant fits for the data with superratio values of 0.9 for ^{81}Kr and 0.7 for ^{85}Kr.

As we can see, even with none of the samples contributing any ^{85}Kr, the superratio is 0.7 with respect to the reference, setting a lower bound on the contamination values (and demonstrating that 70% of the contaminant is from the reference gas). Provided we do not

have any enriched samples, a ratio of 1 with respect to the reference is our upper limit.[14] Given that the amount of contaminant gas typically appearing in our sample is only about 1% of the total sample gas volume after the wash procedure (making the correction very small), and most environmental samples fit the pattern described during these measurements, we can simply apply SR values of 0.9 and 0.7 for ^{81}Kr and ^{85}Kr, respectively, to the contaminant. The error on these corrections is about 20% to account for the uncertainty in these fits plus the error due to the measurement of the outgassing rate.

Given the outgassing rate and the contaminant ratio values, we can finally apply the correction for cross-sample contamination. We define the superratio that we actually measure for a given sample M_S, which has a real superratio S, to be altered by the contaminant as

$$M_S = (1 - f)S + fC \qquad \text{where} \qquad f = \frac{R_{\mathrm{Kr}} t}{2P_{\mathrm{avg}}}. \tag{2.15}$$

where f is the fraction of sample replaced by contaminant gas and C is the superratio of the contaminants previously defined. To get f, we need t, the length of the measurement, R_{Kr} the linear outgassing rate of the contaminant discussed, and P_{avg}, the average pressure of the run. Then we just solve for S and we finally have our corrected superratios for ^{81}Kr and ^{85}Kr.

The whole process including the analysis, correction, and wash takes 24 hours. Not bad for a single day's work.

14. For ^{81}Kr, samples that are naturally enriched beyond the modern ^{81}Kr/Kr value are not expected. For ^{85}Kr even the air has twice as high a ^{85}Kr/Kr abundance compared to our reference because our reference gas was collected from the atmosphere 15 years ago (see Section 4.3). However, our typical samples tend to be old enough to contain very little and those that we don't expect to be as old are typically measured in a different manner (see Chapter 5). However, if we do incidentally measure a sample with high ^{85}Kr/Kr compared to the reference, we can make a direct contamination measurement to account for it and better understand its effect in the future.

CHAPTER 3

IMPROVEMENTS IN ATTA

In this Chapter we review the improvements made during the work for this dissertation, which have collectively led to the state-of-the-art system described in Chapter 2. In Section 3.5 we discuss the statistical and systematic error limits that these improvements have achieved for measuring samples.

3.1 Enhanced recycling

The most major enhancement in increasing atom counting efficiency comes from the enhancement in gas recycling. As mentioned in Section 2.2.8 and diagramed in Figure 2.11, there are three turbomolecular pumps which keep the system under vacuum, removing gas from the 3D MOT chamber, back to the beam chopper chamber, back to the transverse cooling chamber, and ultimately out of the system. We installed a fourth turbomolecular pump (300 L/s) in the configuration shown in Figure 3.1 (a). We also replaced the fittings for the vacuum chamber at the source to minimize volume with a custom piece shown in Figure 3.1 (b).

Prior to the installation of this enhancement, it required 10 μL of Kr gas at STP to reach a pressure of 2 $\times 10^{-6}$ Torr in the transverse cooling chamber.[1] At this pressure, the plasma visibly filled only the AlN tube and was in what we refer to as the "weak mode." By comparison, when the pressure in the transverse cooling chamber exceeds approximately 2.5 $\times 10^{-6}$ (depending on the gas composition in the source) the plasma will suddenly "jump" modes, visibly extending also into the vacuum fittings upstream of the source volume. We refer to this condition as the "strong mode." Furthermore, it should be noted that the plasma

1. We use the transverse cooling chamber pressure as the reference point because (a) the volume on the upstream portion of the source has changed and (b) measuring the pressure in the source chamber is difficult due to the plasma's potential interference with gauges and so we removed the gauges for further volume minimization.

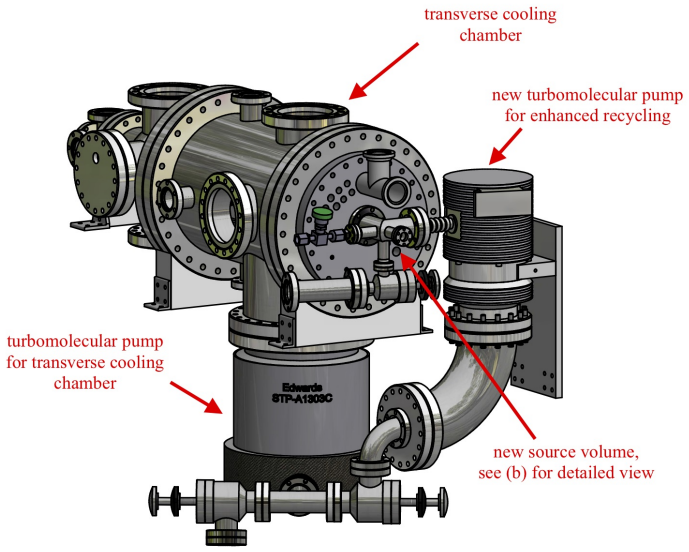

(a)

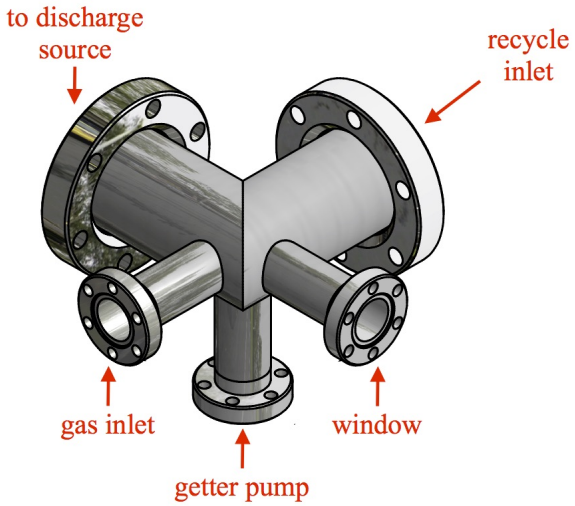

(b)

Figure 3.1: (a) An improved design for gas recycling. An additional turbomolecular pump connects the outlet of the transverse cooling back to the source, thus compressing gas in the source volume and increasing the pressure upstream without increasing the amount of gas which needs to be injected into the system. The previous iteration of the vacuum system followed the same path but without this "recycling" pump and with a different set of vacuum fittings making up the volume at the source. (b) The new custom five-way cross vacuum fitting for the source volume. The design is meant to minimize volume and thus increase pressure, reducing the minimum amount of gas required to reach the most efficient plasma discharge mode for producing Kr^* from 20 μL to 8 μL. The three 1-1/3 inch ports are for the inlet of gas from the sample reservoir, the getter pump, and the window that allows us to insert the clock laser. The 2-3/4 inch ports are for the recycled gas returning from the turbo pump and the input to the AlN tube. Drawing courtesy of Thomas O'Connor.

has two or three sub-modes within each of these modes which are not visibly different, but are seen by small jumps in the metastable production. The highest metastable production efficiency occurs when the pressure in the transverse cooling chamber is 4 - 6 $\times 10^{-6}$ Torr, one of the sub-regions of the strong mode discharge.

Since our goal has been to increase efficiency, but also reduce sample size, we wished to achieve this pressure regime with current or lower sample size requirements. Hence the insertion of the new pump and reduced volume fittings. This enhancement means that it only requires 8 μL of krypton gas at STP to reach 5 $\times 10^{-6}$ Torr. As a result, the initial ^{83}Kr loading rate for sample measurements with 10 μL went from an average ion current 1.8 nA (corresponding to 2 $\times 10^{10}$ atoms per second) to our current typical loading rate of 8 nA with only 8 μL, a factor of 5 improvement. To be explicit about the nature of this improvement, we expected at least a factor of 2.5 from the increase in pressure in the source chamber, which naturally increases gas throughput. The remaining factor of two comes from using the optimal strong mode of the plasma discharge, which both increases metastable production efficiency per atom, but also improves cooling. Because the RF signal is better coupled to the plasma in this mode, less energy is being dissipated as heat in the source, reducing the equilibrium temperature from 125 K in the weak mode to 105 K in the strong mode. This temperature reduction gives a respective reduction in atom velocity and thus an increase in atom capture efficiency.

3.2 Improved wash procedures

When the ATTA-3 system was presented in (23) as a tool for measuring environmental samples, the required time for a measurement of ^{81}Kr/Kr and ^{85}Kr/Kr relative isotopic abundances in a sample was 48 hours. The largest portion of this time was devoted to washing the system on account of cross-sample contamination; washes required 40 of the 48 hours. 16 hours of the washing was spent in the strong mode and then 24 hours in the weak mode. The reason for washing in both modes is that they wash different parts of the source

volume at different rates. By using this method, we reduced the contamination fraction f from equation 2.15 below 0.01, i.e. 1% of the sample volume.

We wished to increase sample throughput by a factor of 2 by reducing the total time for a measurement to 24 hours, specifically by reducing in wash time from 40 hours to 16 - 18 hours. Two major improvements allowed us to make such an advancement.

First, we increased the RF power used to run the discharge during the wash. Previously the RF input power was input 22 - 24 W, the same power as we use during a measurement. We previously limited the wash to this same power level for fear of overheating the source, since it is not ℓN_2 cooled during washes.[2] However, testing demonstrated no damage to the source at higher temperatures. Thus we raised the RF power to 30 W, increasing wash effectiveness.

Second, we replaced the manual knob of the leak valve that controls the xenon washing gas pressure with a stepper-motor operated through a LabView program. This now digitally-operated leak valve gives us constant control of the pressure during the wash period, allowing us to switch between the strong and weak modes in short cycles. With this control we now execute a new procedure: after running a sample and reference in the strong mode, we conduct 30 minute wash cycles for the duration of the wash where 75% of the time is spent in the strong mode, and 25% of time is spent in the weak mode. By the end of 16 - 18 hours of washing, the average contamination fractions based on our outgassing tests and typical sample run-time is 1% of the sample volume.

This advancement allows for us to measure one sample per day by conducting the wash overnight.

3.3 Stabilization and systematic tests

While Sections 3.1 and 3.2 noted improvements in efficiency and sample throughput, this Section is focused on handling systematic effects to ensure and improve the precision of

2. This is because the cooling will freeze krypton onto the chamber walls, reducing the wash's effectiveness.

our measurements. Our goal, which we demonstrate in Section 3.4, is 1% in the one-sigma relative isotopic abundance measurements (superratios) of ^{81}Kr/Kr and ^{85}Kr/Kr.

3.3.1 Zeeman slower stabilization

The Zeeman slower is a powerful tool, responsible for over three orders of magnitude in our capture efficiency for all isotopes, as noted in Section 2.2.5. However, it is also a large potential systematic in relative isotopic abundance measurements. Specifically, because we choose to avoid putting repumping sidebands in the Zeeman slower, we are certainly going to lose some atoms to dark states. Now, if the number of atoms we lose for each isotope is different, that alone is not a problem. Many things effect the isotopes differently and that is precisely why we measure a reference. But if the rate at which that happens to each isotope changes intraday (while we are measuring the sample and the reference), then we have an issue. One such parameter which could alter the loss rate to dark states is a change in light intensity, and we discovered that the Zeeman slower power intensity could shift up to 10% in a single day.

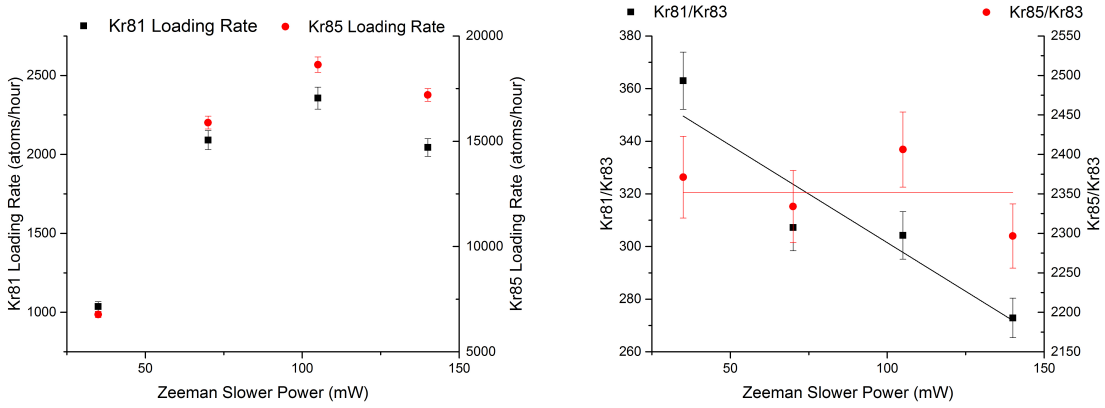

(a) (b)

Figure 3.2: (a) The raw loading rates for ^{81}Kr (left axis) and ^{85}Kr (right axis) in atoms per hour versus Zeeman slower power. (b) Ratios of the ^{81}Kr (left axis) and ^{85}Kr (right axis) over ^{83}Kr loading rate versus Zeeman slower power. The ^{85}Kr/^{83}Kr ratio is shown to fit well to a constant (red line), while ^{81}Kr/^{83}Kr fits a linear function, presenting at least a first-order effect (black line). All measurements were done in a single day on the standard reference gas in the open mode configuration.

So, we chose to investigate the effect. We measured the loading rates for all three isotopes at four different powers (35 mW, 70 mW, 105 mW, and 140 mW) for the reference gas in the open mode and took ratios of the radioactive nuclides versus the stable nuclides to see the relative effects. The results are shown in Figure 3.2. As we can see from the ^{81}Kr and ^{85}Kr loading rates plotted in Figure 3.2 (a), there is clearly an optimal power for maximizing these loading rates. Too little power and we are not slowing the atoms enough. Too much power and a variety of effects, e.g. excessive pumping into dark states, can cause a reduction in slowing efficiency. Furthermore, when we compare the loading rates to the ^{83}Kr loading rate in 3.2 (b) we notice that while ^{85}Kr/^{83}Kr ratios hold fairly constant, ^{81}Kr/^{83}Kr shows evidence of some first-order effect with respect to slower power. Thus we implemented an active power stabilization system to keep the power at just over 100 mW to maximize the ^{81}Kr loading rate based on the raw loading rates shown in Figure 3.2 (a), but prevent the first-order systematic effect seen in Figure 3.2 (b).

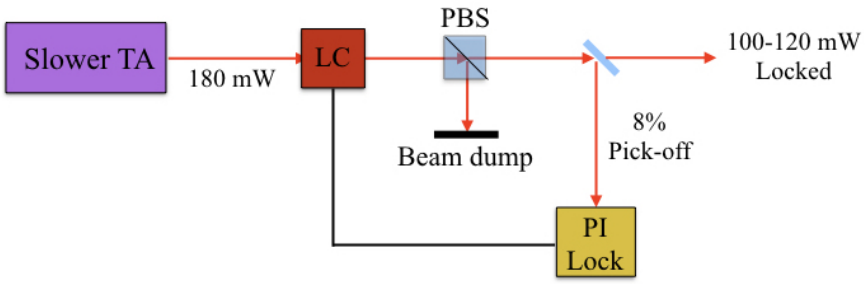

Figure 3.3: Diagram of Zeeman slower power stabilization system. The power coming from the tapered amplifier is fed through a liquid crystal polarizer and then a polarizing beam splitter. 8% of the light is picked off from a pellicle plate for a proportional-integral lock system which controls the feedback to the liquid crystal for stabilization. Other optics which alter beam size and direction are omitted from the digram for simplicity.

The stabilization system is diagramed in Figure 3.3. Light from the slower goes through a liquid crystal which acts a waveplate, shifting the polarization of the light by a desired amount. The polarizing beam splitter splits the vertically polarized component, which is

thrown away, from the horizontally polarized component, which will go to the system. Before going to the system however, 8% of the light is picked off and read out via photodiode as part of a proportional-integral locking system. Based on that signal, the PI lock feeds a voltage to the liquid crystal, which adjusts the polarization to restore to power to the set level. With stabilization, the power fluctuation is under 1%.

3.3.2 Sideband stabilization

As discussed, while we do not inject sidebands into the slower to avoid interference between shifted hyperfine levels, the transverse cooling and MOT chambers are far less susceptible to such effects. However, this does not mean that we can take for granted that they are free of any problems. While we have control over the transfer between the hyperfine levels of each independent isotope in these chambers, we must consider how the laser light from these repumping beams may be affecting *other* isotopes that we are not intending to trap.

Specifically, we consider the problem of accidentally trapping ^{82}Kr while we intend to trap ^{85}Kr. The first repumping sideband for ^{85}Kr is -76 MHz detuned from the ^{84}Kr trapping transition. Unfortunately, the ^{82}Kr trapping transition is -64 MHz detuned from the ^{84}Kr trapping transition; a difference of only 12 MHz. While that is not exactly on resonance, the 10^{10} difference in abundance means that even this far off resonance we will still see interaction with some atoms given our detection sensitivity. Not having repumping beams in the slower mean that there is no light to cool the ^{82}Kr longitudinally, but it can be still be cooled and focused transversely by the sidebands in the transverse cooling and MOT sections. The strength of the interaction is thus determined by how much power from the carrier is placed into the sidebands. At <1% sideband power (with respect to the carrier) there is some photon scattering of ^{82}Kr that adds just a couple of percent to the natural laser background (about 20% of a single atom's signal). But if the power exceeds 1% very much, then we weakly trap the ^{82}Kr in the 3D MOT, which overwhelms our ^{85}Kr signal.

During an investigation of background fluctuations on the ^{85}Kr signal, we observed

the occasional formation of this weak krypton MOT and traced the cause to instability in the sideband power. This instability was driven by temperature fluctuations in the room which altered the sideband production efficiency of our fiber-based electro-optical modulators (EOMs). These EOMs rely on how the optical properties of their internal crystals phase modulate the light passing though with respect to changes in electric field (40). Thus, they can be sensitive to temperature shifts that also effect the optical properties of the crystal. In extreme cases, we observed these fluctuations alter the sideband production efficiency up to a factor of 2.

To eliminate this systematic, we temperature stabilized the EOMs using a Peltier Thermoelectric Module in combination with a temperature controller, which reads out the temperature via the resistance of a nearby sensor and feeds back to the Peltier a current to control the temperature within $< 1\ ^{o}$C. With this stabilization in place, the sideband power is held just below 1% of carrier power and the ^{82}Kr background contribution returns to a very weak and stable scattering contribution that appears as just a flat 2% increase in the laser background photons. The EOMs in this temperature stabilization setup are shown in Figure 3.4.

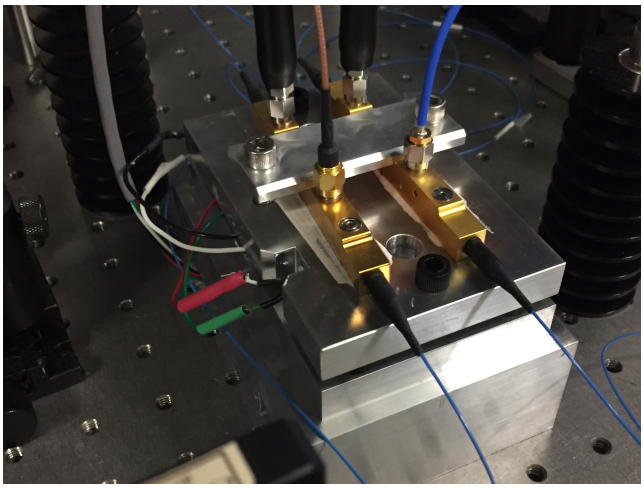

Figure 3.4: Image of EOM temperature stabilization setup. Two EOMs (the gold color rectangular prisms), one for producing sidebands on the transverse cooling beam and the other for producing sidebands on the MOT beam, are fastened down to an aluminium plate. The plate is temperature controlled by a Peltier Thermoelectric Module beneath it. Thermal paste is used to improve the thermal conductivity between the EOMs, the plate, and the Peltier.

3.3.3 MOT power control

The switching of the MOT power between the trapping (high power) mode and the detection (low power) mode is controlled by the Swift Variable Retarder mentioned earlier in Section 2.2.1. Effectively, it is a liquid crystal element, just like the one used for stabilization in Section 3.3.1 and Figure 3.3. It is fed a voltage for each of the two modes that alters the polarization of the light, which given the polarization beam splitter that follows, effectively controls the power.

When trapping ^{83}Kr, only the high power voltage is fed to the crystal. Then, when the cycle switches back to trapping ^{81}Kr, the voltages are alternated. Unfortunately, switching between these two different voltage loads causes the liquid crystal to slowly drift between two different equilibrium temperatures. While drifting, these fixed voltages actually provide slightly different polarization shifts, causing a slow drift in the MOT power at the beginning of each ^{83}Kr and ^{81}Kr cycle.

Previously, we removed this effect during analysis when we corrected for slow drifts, but it is certainly preferable from a systematic point of view to remove it experimentally. We can solve this in one of two ways: long-term temperature stabilization to counter the drifting temperature as in Section 3.3.2 or direct power stabilization as in Section 3.3.1. We choose the latter since it provides stabilization of both the laser's natural fluctuations and that of the liquid crystal.

The stabilization system we employ is shown in Figure 3.5 and is very similar the one used in Figure 3.3. The only difference is the location of the pick-off for the signal on the photodiode to use as feedback via the proportional-integral lock system (SRS SIM960 PID). On the 3D MOT, while six beams are needed for trapping, we only split the MOT laser into three separate beam and feed those into the MOT along each axis. We provide for the three counter-propagating beams by retroflecting the initial three beams (which are then passed through wave plates to adjust their polarization appropriately). When these beams return to the beam splitter we initially used to separate them, part of the beams pass back out

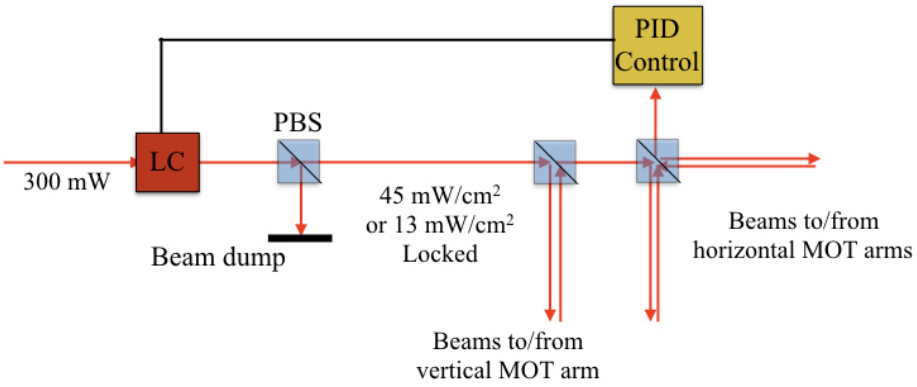

Figure 3.5: Diagram of the 3D MOT power stabilization system. The power coming originally from the tapered amplifier is fed through a liquid crystal polarizer (Swift Variable Retarder) and then a polarizing beam splitter. This light is separated via beamsplitter to provide light for each axis of the MOT chamber. The retroflected beams which return through the unused side of the beamsplitter are picked off for a proportional-integral lock system which controls the feedback to the liquid crystal for stabilization. Other optics which alter beam size and direction, as well as additional retroflections which occur but are not used, are omitted from the digram for simplicity and clarity.

along the previously unused side of the splitter, allowing us to pick-off the beam from there for reference.[3]

Note that this stabilization system has one further requirement beyond the one in Section 3.3.1: because the power is switching on the order of 100 ms (determined by the cycle time in Section 2.2.6), the time constant of this stabilization method must be able to switch fast enough not to introduce a new short-term systematic effect. Thus we chose a PID control with a time constant of order 1 ms.

With this stabilization, besides removing the systematic drift in the liquid crystal, we now have a monitor of the MOT power during the run as well as power stability control.

3. This position for the pick-off is slightly suboptimal because two MOT beam arms come through the splitter and can interfere with one another. However, given the current optical table setup, this was the least intrusive choice. A slight alignment adjustment solves the interference problem.

3.3.4 Quench laser testing

In Section 2.2.6, we described how we use a laser locked on the ^{83}Kr quench transition to excite ^{81}Kr and ^{85}Kr atoms along said transition. We did so without presentation of a calculation since (a) the ^{81}Kr and ^{85}Kr quench transitions are actually unmeasured, thus limiting the use of such a calculation and (b) we chose to instead perform here a robust experimental demonstration that the quench laser is currently sufficient to achieve quenching in all three isotopes. We do so because of the potential systematic effect a failure in the quench mechanism can cause; if the quench beam does not consistently remove atoms from the trap, we may accidentally double count atoms, artificially boosting our loading rate at random intervals. So, to control this systematic effect, we must ensure that the quench beam is always doing its job.

Our demonstration requires that we load ^{81}Kr and ^{85}Kr atoms into the trap using the usual cycle of trapping, detection, and quenching. However, on the cycle immediately following the regular one, we permit two cycles to pass during which the Zeeman slower is inactive, and thus the loading rate is reduced by four orders of magnitude. As such, during these cycles, we should not see any atoms in the trap provided the quench laser is operating as expected. Following these two "blank" cycles, we begin again with a regular cycle, followed by another pair of blank ones, and so forth.

In analysis, we compare the number of counted atoms that survived into the blank cycles, which should be empty, with the total number counted in the regular cycles. For ^{81}Kr, 3 atoms survived out of 558, demonstrating >99.4% quenching efficiency. For ^{85}Kr, 1 out of 1224 atoms survived, demonstrating >99.9% quenching efficiency. We state the quenching efficiency as >X% since, in theory, even with the significantly diminished loading rate from lacking the Zeeman slower, the "surviving" atoms may not have survived, but were actually loaded in the trap, falsely reducing our quenching efficiency. Regardless, these values are more than sufficient to allay concerns of a 1% systematic effect in measuring superratios.

3.3.5 Reference measurement frequency

When ATTA operated with errors in the 5 - 10% range of precision, reference measurements were not taken daily but instead once every two weeks, and this reference measurement was added to a running average of reference measurements to provide the $^{81}Kr/^{83}Kr$ and $^{85}Kr/^{83}Kr$ ratios for use in equation 2.11. Naturally, this subjected the technique to efficiency drifts that occurred over the two-week period, which, at the 5 - 10% level, was acceptable. However, with the increased efficiency from the enhanced recycling technique (Section 3.1), the time required to measure a sample became short enough (< 4 hours) that it was feasible to do same day reference measurements. The question of course remained, for 1% precision in our superratio measurements are these daily reference measurements in fact necessary or are the efficiency drifts over a two week period small enough not to concern ourselves with them?

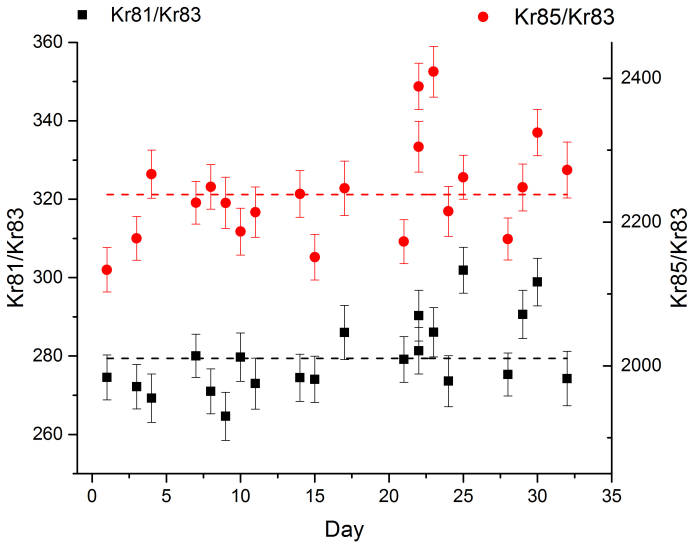

Figure 3.6: 20 $^{81}Kr/^{83}Kr$ (left axis, black squares) and $^{85}Kr/^{83}Kr$ (right axis, red circles) ratio measurements in the reference gas over one month. The ratios are fit to a constant weighted average where the weights are determined by the error on each independent measurement. The $^{81}Kr/^{83}Kr$ average (dashed black line) is 279.4 $\pm$ 1.3 with a reduced chi-squared of 2.53. The $^{85}Kr/^{83}Kr$ average (dashed red line) is 2239 $\pm$ 15 with a reduced chi-squared of 4.69. Ratios are measured in atoms/hour/nA.

Figure 3.6 shows ratios for $^{81}Kr/^{83}Kr$ and $^{85}Kr/^{83}Kr$ measured in the reference gas

over one month (with units of atoms/hour/nA) with the majority of the upgrades from this Chapter in use. Both ratios are fit to a constant and a reduced chi-squared is calculated in each case. For ^{81}Kr/^{83}Kr the relative error of the weighted average (using the error of each measurement to determine the weights) is 0.5% and the reduced chi-squared is 2.53. For ^{85}Kr/^{83}Kr the relative error of the weighted average is 0.3% with a reduced chi-squared 4.69. These suggest some instrument noise on the 0.8% level for ^{81}Kr/^{83}Kr and a 0.7% level for ^{85}Kr/^{83}Kr, which is not quite 1%. As such, we admit that we could probably get away with, say, weekly measurements if we so choose. However, we decided to instead switch to daily reference measurements for three reasons. First, we know that major optical realignment can shift the relative efficiency up to 20%, and if we have weekly reference measurements, that prevents us from doing such a realignment intra-weekly if needed. Second, as shown in Section 2.5, these daily references simplify our contamination model considerably. Third, since we know there are drifts, we may do a bit better than the precisions measured here by using daily measurements (we certainly won't do worse). We now demonstrate this new precision with the inclusion of daily reference measurements in Section 3.4.

3.4 High-precision corrections of isotope ratios

3.4.1 Mass fractionation

In Section 3.3.5, the repeated measurements of standard reference gas demonstrated systematic control at better than the 1% level for measurements of the ^{81}Kr/^{83}Kr and ^{85}Kr/^{83}Kr ratios in the open mode configuration. However, to measure a sample, we conduct a closed mode measurement of the ^{81}Kr/^{83}Kr and ^{85}Kr/^{83}Kr ratios and compare that to these open mode measurements (made daily and uniquely paired with each measurement), and it is on that superratio that we wish to demonstrate not only 1% precision (through repeatability), but also accuracy. To check whether we have succeeded at these goals, we measured 10 μL of reference gas in the closed mode as if it were a sample and then measured the reference

gas in the open mode and calculated the superratio, which ought to be 1 for both ^{81}Kr and ^{85}Kr. The results are shown in Figure 3.7.

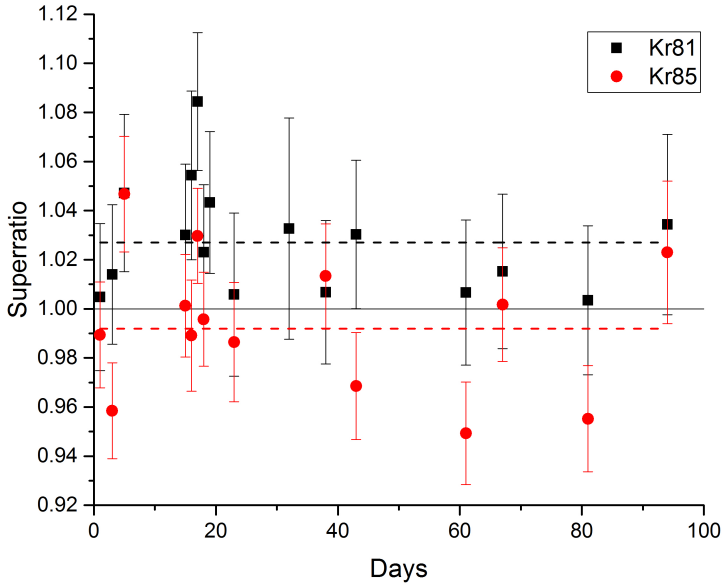

Figure 3.7: ^{81}Kr (black squares) and ^{85}Kr (red circles) superratios for the reference gas measured as sample. The weighted average for ^{81}Kr superratios (black dashed line) is 1.027 ± 0.008 with a reduced chi-squared of 0.57. The weighted average for ^{85}Kr superratios (red dashed line) is 0.991 ± 0.006 with a reduced chi-squared of 1.77. A solid black line marks a superratio of 1.

As is apparent, neither superratio is quite 1, although the ratios demonstrate that we have better than 1% precision (slightly improved from Section 3.3.5 as a result of the now daily referencing). The ^{85}Kr superratio is over one sigma below 1, and the ^{81}Kr superratio is over three sigma off in the *opposite* direction. Alone, the effect on the ^{85}Kr superratio might be ignored as insignificant, but taken together, the opposing differences suggest that the effect stems from a known issue that occurs only in the closed mode that we simply have not yet accounted for: mass fractionation.

In principle, the Kr* that leaves the plasma, regardless of isotope, has the same energy distribution. However, as a result, we thus expect the different isotopes to have different velocities, since the constant energy is proportional to mv^2, where m is the isotopic mass and v is the velocity of the atom. Thus, the heavier isotopes should move slower than the

light isotopes by a factor of $\sqrt{\frac{m_{\text{heavy}}}{m_{\text{light}}}}$. In the open mode, this effect is not relevant. The isotopes may move at slightly different speeds, but they all get to the trap eventually and then are tossed out of the system. In the closed mode, this case no longer holds. Because the gas is recycled, the faster moving atoms have more opportunities to be trapped than the slower moving atoms based on the conductance of the vacuum system.

Since the ratios we measure compare ^{81}Kr and ^{85}Kr with ^{83}Kr, we should thus expect (using the aforementioned factor) the ^{81}Kr/^{83}Kr ratio should be ∼1.2% higher in the closed mode than the open mode and similarly the ^{85}Kr/^{83}Kr ratio should be ∼1.2% lower in the closed mode than the open mode. Qualitatively these expectations agree with our data, although we are still not perfectly in line with theory. That is because we have a number of tools on our system that alter the velocity of the atoms travelling in the system slightly differently from isotope to isotope (e.g. the four turbomolecular pumps), whose effects are difficult to quantify so precisely. Thus we accept that our system has a unique (but stable) mass fractionation fingerprint, demonstrated by the results in Figure 3.7. We correct for this effect in our final sample superratio calculations using the weighted averages in Figure 3.7 and using the errors from the weighted averages as the error contribution from the correction to our measurement.

3.4.2 Trap lifetime corrections

Conducting the measurement discussed in Section 3.4.1 still disguises one last systematic effect that exists between the open mode and closed modes, but is not normally apparent when only measuring the reference gas.

Each sample that is measured is (ideally) primarily composed of krypton gas. However, depending on the geochemical conditions of the sampling location and the steps taken to perform chemical purification, each sample has its own unique composition of other gases in practice, often in trace amounts, but sometimes not. Now, most of these other gases are frozen out or removed by the getter pump during the closed mode runs. Furthermore, other

gases like CH_4, which are neither frozen nor initially gettered, are often broken down into constituent parts (e.g. C and H_2) by the plasma discharge and can then be removed by the getter pump. In fact, there is ultimately only one element that is both not removed in any manner and can be present in any sample: argon.

At first consideration, one might pass over the presence of the argon as a nonissue. However, we discovered that the increased presence of argon can indeed alter our superratios. During an experiment[4] where we applied an argon wash rather than a xenon wash in our system and then effectively conducted the same measurement discussed in Section 3.4.1, we got different results. Those results are shown in Figure 3.8.

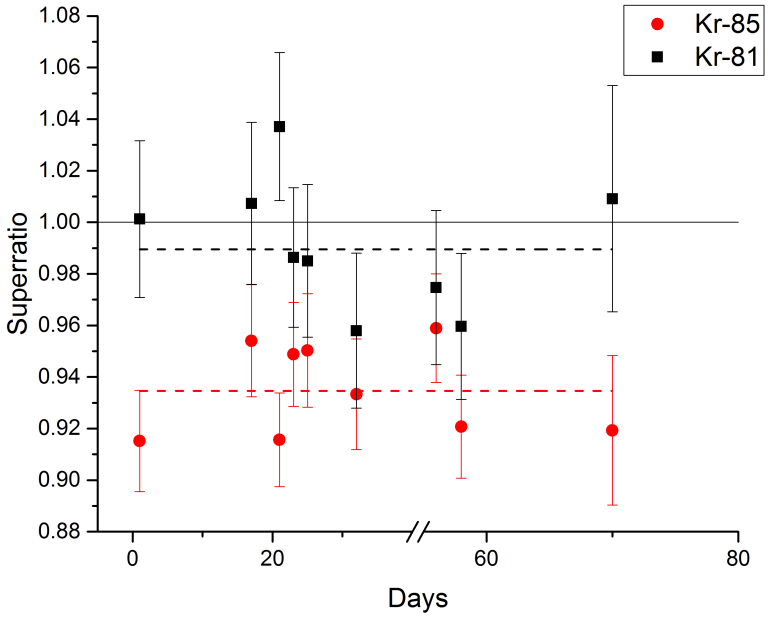

Figure 3.8: ^{81}Kr (black squares) and ^{85}Kr (red circles) superratios for the reference gas measured as sample with an argon gas wash. The weighted average for ^{81}Kr superratio (black dashed line) is 0.990 ± 0.010 with a reduced chi-squared of 0.74. The weighted average for ^{85}Kr superratio (red dashed line) is 0.935 ± 0.007 with a reduced chi-squared of 0.74. In both cases, the weights are determined by the errors of each individual measurement. A solid black line marks a superratio of 1.

In these results we still see the mass fractionation effect that is in agreement with the previous value. However, we see an overall shift in both superratios significantly downward

4. The same experiment that is the focus of Chapter 4.

by ∼4 - 5%. We believe the cause for this shift to be the issue of single atom trap lifetime (discussed first in Sections 2.2.6 and 2.4). During the closed mode measurements seen here the implanted argon from the argon wash enters into the source volume when knocked out by krypton from the discharge and its contribution to the gas composition grows over time. In the open mode, because the gas is constantly pumped away, there is no such issue. And when using xenon gas, the 100 K temperature resulted in most of the xenon that would build up in the system being frozen back onto the chamber walls. As such, only in the closed mode with an argon wash would we see this increase in argon pressure. This increase in pressure can reduce the lifetime of the atoms in the MOT in the closed mode compared with the open mode. If the MOT lifetime is shorter, then there is a higher probability that an atom trapped during the collection phase will be knocked out before the detection phase. This effect artificially suppresses the loading rate of ^{81}Kr and ^{85}Kr the closed mode, but not of ^{83}Kr, since the loss in the large MOT is still completely dominated by the two-body ionization processes. Thus producing a shift in the ^{81}Kr/^{83}Kr and ^{85}Kr/^{83}Kr ratios in the closed mode with respect to the open mode.

So now we understand that the presence of increased argon in the system can cause such an issue, but what is the magnitude of the effect as a function of argon pressure? To determine the answer to this question, we took the xenon wash measurements and the argon wash measurements from this Section and Section 3.4.1 and cut them into three pieces. As mentioned in Section 2.3, there is a small leak into the vacuum system of air, which thanks to the getter, results only in a small leak of argon. Thus, each section of the xenon wash measurements has a different argon pressure due to this small leak. Each section of the argon wash measurements also has a different argon pressure due to the continued exchange between the krypton and argon. Thus we have six different argon pressures, which give us six different superratios. These six superratios for ^{81}Kr are shown in Figure 3.9 versus the argon/krypton pressure ratio as read by the RGA with electron multipler (EM) gain active.[5]

5. This pressure ratio is by no means the real pressure ratio. There are corrections to make for the RGA

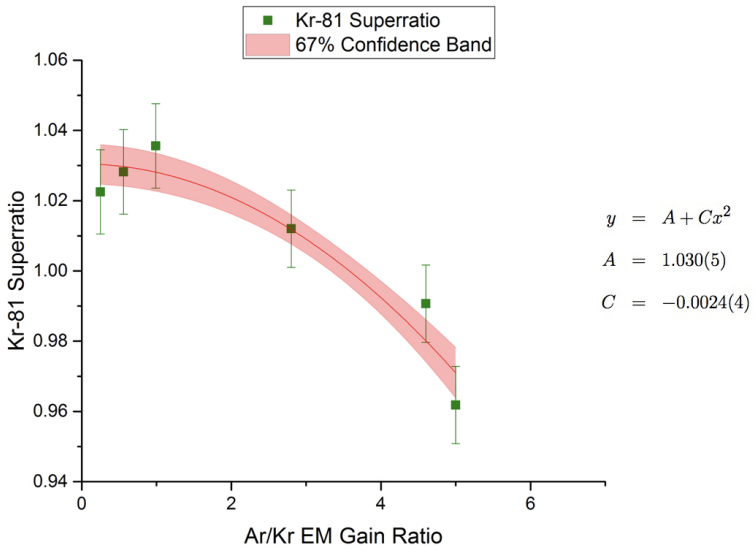

Figure 3.9: ^{81}Kr superratios versus Kr/Ar gas pressure on RGA with EM gain. The data is fit to a second-degree polynomial with the linear order contribution set to zero. The confidence band shown is at the 67% level.

We can see an obvious effect, which is insignificant due to argon just from the air leak, but quite significant at higher Kr/Ar RGA-EM ratios. As an empirical model, we apply a fit to a second-degree polynomial (with contribution from the linear order set to zero). Granted if we wanted to extend beyond the Kr/Ar RGA-EM ratios seen here, this empirical model would not do us very well. However, samples rarely tend to exceed ratios of 2, much less reach the edge of our model. Thus we use the fit shown with the error on the fit to apply this trap lifetime correction to due the argon pressure as routinely measured by the RGA.

3.5 Current ATTA error limits and volume requirements

3.5.1 Statistical and systematic error limits

With these corrections, we finally have accurate superratios for providing ^{81}Kr/Kr and ^{85}Kr/Kr relative isotopic abundances in our samples. All that is left is to quantify how precise ATTA's measurements can be, specifically for ^{81}Kr-dating of environmental samples.

efficiency, and additional ones to make for the EM gain efficiency. However, we use the straight ratio knowing that these efficiencies do not change.

As we mentioned at the outset of Section 3.3, we wished to demonstrate–and have demonstrated in Section 3.4–1% precision in the relative isotopic abundance measurements. However, that is not normally the limiting factor in our ^{81}Kr/Kr measurements of a single sample. The primary limitation is statistics. To understand how our statistical error compares to the systematic ones, we plot the relative age error for a typical 10 μL sample alongside the systematic error limits at the 3% and 1% levels in Figure 3.10.[6] All errors discussed here and elsewhere, we should note, are one-sigma relative uncertainties unless otherwise stated.

This typical "statistical error" is determined by

$$\mathrm{Err}(V,t) = \frac{t_{1/2}}{t \ln 2} \sqrt{\frac{1}{(2^{-t/t_{1/2}})200V} + \frac{1}{200V}} \tag{3.1}$$

where V is the volume of the sample in μL, $t_{1/2}$ is the half-life of ^{81}Kr in kyr, and t is the ^{81}Kr age of the sample in kyr. The idea here is that the system efficiency typically results in 200 atoms being counted per μL of sample volume (V) if the sample has a modern ^{81}Kr/Kr abundance. Thus the first term in the square-root is further adjusted by the age of the sample: if it is older, there are fewer atoms to count. The second term represents the error in the daily reference measurement. The pressure in the reference measurement, to avoid systematic effects, is adjusted to roughly match that of the closed mode measurement. So if the volume of the sample is smaller, resulting in a reduced count rate and a reduced pressure, the reference measurement count rate will also be reduced in turn. These errors are added in quadrature to give the total statistical error of the measurement. The pre-factor outside of the square-root is simply a result of converting from a ^{81}Kr/Kr relative isotopic abundance error to a relative ^{81}Kr-age error.

Equation 3.1 holds for samples as small as 4 μL[7], but can be scaled up for samples larger than 10 μL. Such scaling does not mean that we measure more than 10 μL in a single sample,

6. Note that the percent error level for the systematic errors are in terms of the superratios, so when normalized to ^{81}Kr-ages they are hence not simply straight lines in Figure 3.10.

7. We will discuss the issue of smaller samples subsequently in Section 3.5.2

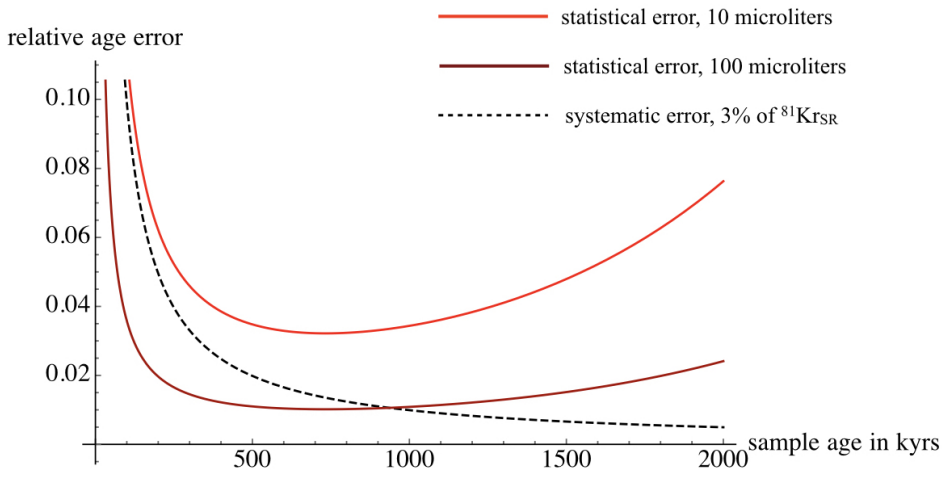

(a)

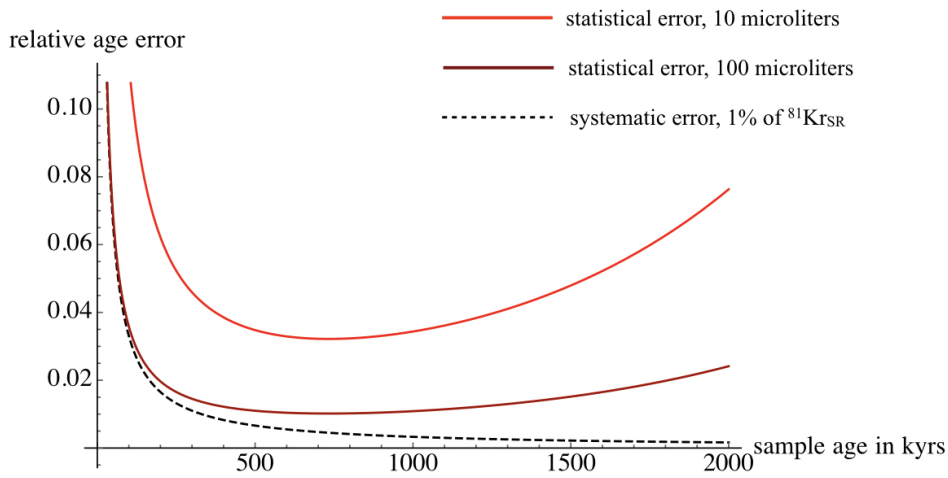

(b)

Figure 3.10: ATTA statistical and systematic relative age errors plotted against the ^{81}Kr age of the sample being measured. The statistical errors are plotted using equation 3.1 (see text) for a 10 μL (red) and 100 μL (dark red) sample. (a) The statistical uncertainties are compared with a 3% systematic error in the ^{81}Kr superratio (black, dashed). (b) The statistical uncertainties are compared with a 1% systematic error in the ^{81}Kr superratio (black, dashed). Note, the uncertainties plotted here exclude any contributions from cross-sample contamination corrections.

but rather that we can measure the sample in 10 μL intervals each day over as many days as we like. Obviously, this is not pratical to do for many samples, but can be done for special samples which require small statistical uncertainty, as we will see in Chapter 4. The statistical error for a 100 μL sample (which would be measured over 10 days), is also shown in Figure 3.10.

In measuring a sample that is 100 μL or larger, the statistical error comes down to the same relative uncertainty level as the 1% systematic error for younger samples, as seen in Figure 3.11, a subsection of Figure 3.10 zoomed in on the range of sample ages from 10 - 100 kyr. While ^{81}Kr-dating is obviously suboptimal for this age range, even conducting 10-20% relative age error measurements (that is 5,000 - 10,000 year errors on a 50,000 year old sample), can be extremely useful as a compliment to ^{14}C-dating in aquifers around this age range. The ^{81}Kr-ages in such aquifers can act as a check or calibration for the many corrections needed for ^{14}C-dating, particularly around 50,000 years, where small corrections in ^{14}C/C abundances lead to large shifts in the result.

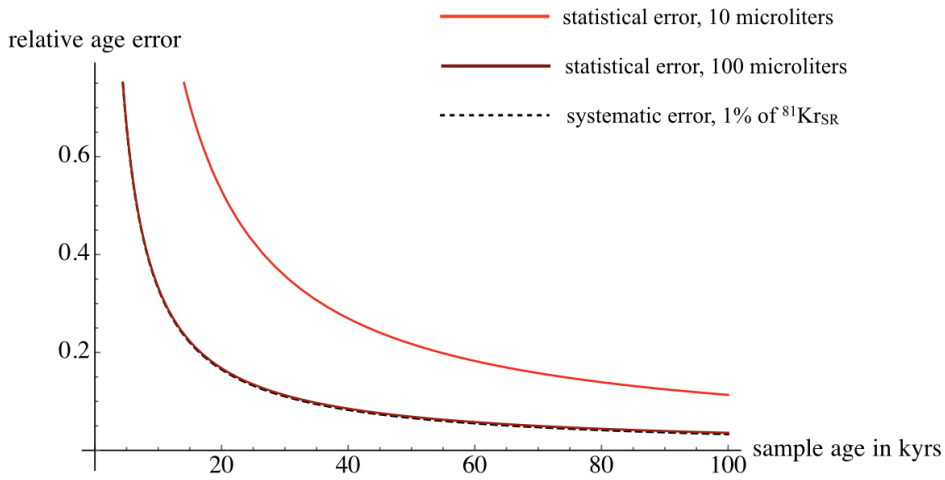

Figure 3.11: ATTA statistical and systematic relative age errors plotted against the ^{81}Kr age of the sample being measured from 10 - 100 kyr. The statistical errors are plotted using equation 3.1 (see text) for a 10 μL (red) and 100 μL (dark red) sample. The statistical uncertainties are compared with a 1% systematic error in the ^{81}Kr superratio (black, dashed).

3.5.2 Sample volume requirements

One last comment must be made regarding sample size. Equation 3.1 only holds down to sample sizes of 4 μL below which point there is not sufficient pressure in the system to run the system in the plasma's strong mode, reducing the loading rate/counting efficiency by a factor of 1.5 or so, beyond the normal scaling with volume. To give a specific example, while we obtain a maximum 8 nA of ^{83}Kr loading rate with only 8 μL, we have a maximum of 1.7 nA with 2.5 μL. Furthermore, due to the usual sample loss, sometimes the pressure must be supplemented by the addition of a different noble gas to keep the discharge alive at all, depending on both the volume and the gas composition of the sample on a case-by-case basis. Adding xenon gas functions when only a small amount of gas is needed. Because most of the xenon is frozen out at the running temperature, it is difficult to add large quantities without causing untenable fluctuations in pressure and discharge mode. Adding argon beyond that point is doable, but it both quenches the metastable efficiency and exacerbates the trap lifetime correction (see Section 3.4.2), potentially beyond the window within which we are comfortable correcting.

As a result of these complexities, it is difficult to report a typical error for these smaller volumes. However, we have demonstrated that ATTA can measure samples as small as 1 μL when care is taken with adjusting the pressure and making corrections. For 1 μL samples with modern ^{81}Kr/Kr abundances, we report a typical statistical error of 20% for ^{81}Kr/Kr, and typical ^{83}Kr loading rates of 0.3 - 0.4 nA. Below 1 μL, too much sample is currently lost due to the discharge source to make a successful measurement. For measurements of these smaller samples, alternative Kr* sources are required (see Chapter 7).

CHAPTER 4

^{81}KR DEVELOPMENT: ANTHROPOGENIC LIMIT

This Chapter is adapted from J. C. Zappala, K. Bailey, W. Jiang, B. Micklich, P. Mueller, T. P. O'Connor, and R. Purtschert. Setting a limit on anthropogenic sources of atmospheric ^{81}Kr through Atom Trap Trace Analysis. *Chemical Geology* **453**, 10.1016/j.chemgeo.2017.02.007 (2017).

4.1 Potential anthropogenic systematic for ^{81}Kr-dating

Since the advent of human nuclear activity, we have potentially been injecting anthropogenic ^{81}Kr into the atmosphere. Testing of nuclear devices, nuclear fuel reprocessing, and usage of medical isotopes are all potential anthropogenic sources of ^{81}Kr. Any anthropogenic contribution of ^{81}Kr from these sources above the precision level of current ^{81}Kr-dating measurements would disturb the atmospheric baseline over the past ∼70 years thereby adding an unacknowledged systematic error on all ^{81}Kr-dating measurements.[1] When the viability of ^{81}Kr as an environmental tracer was initially demonstrated in 1999 using AMS, no difference was measured between a sample of krypton extracted from air before human nuclear activity began and another sample originating from after the end of atmospheric nuclear weapons testing (24). This measurement carried a one-sigma, relative uncertainty of ∼30%. Subsequently, with the development of the second-generation ATTA-2 system, the same experiment was conducted with one-sigma, relative uncertainties around the 8% level (21). Previous theoretical considerations of anthropogenic ^{81}Kr estimated the effect to be at or below the 0.01% level (24).

We decided to perform two 1% one-sigma relative uncertainty measurements using ATTA, which places a 2.5% experimental limit on anthropogenic ^{81}Kr in the atmosphere at the

1. The systematic effects we considered in Chapter 3 were internal systematic effects. Anthropogenic ^{81}Kr and other such external systematic effects were not considered when quantifying our level of systematic control.

90% confidence level. Given the high precision of this limit, we first present a more detailed theoretical model for anthropogenic ^{81}Kr production in the atmosphere in Section 4.2, which sets a new upper limit of 0.15%. Then we perform measurements of samples from the modern era and before the nuclear age at this 1% uncertainty level and use them to place a limit on anthropogenic ^{81}Kr in Section 4.3.

4.2 Anthropogenic sources of ^{81}Kr

Along with the first experimental limit placed on anthropogenic ^{81}Kr production (24), several theoretical calculations were presented to estimate the expected amount of anthropogenic ^{81}Kr in the atmosphere. Those calculations suggested less than 0.01% contribution of anthropogenic ^{81}Kr to the atmosphere. Here we provide an update to those calculations including an in-depth model that removes several simplifying assumptions made in the previous calculations.

To determine a scale for how many ^{81}Kr atoms would cause a 1% contribution, we use the fact that krypton is 1.1 parts per million by volume (17) in the atmosphere (using an atmospheric mass of 5.1×10^{18} kg (41)) and that the isotopic abundance ^{81}Kr/Kr is 6×10^{-13} (2) to determine that there are about 7×10^{25} ^{81}Kr atoms in the atmosphere. Thus we are searching for effects that cumulatively produce 7×10^{23} or more ^{81}Kr atoms, i.e. 1% of the cosmogenic inventory.

There are three potential anthropogenic sources that can contribute ^{81}Kr to the atmosphere as described by (24): decay of ^{81}Rb produced for medical usage, release of ^{81}Kr during nuclear fuel reprocessing, and direct and neutron-induced production of ^{81}Kr during the period of above-ground nuclear weapons testing.

4.2.1 Negligible sources

^{81}Rb, produced for medical applications, decays to the isomer ^{81}Kr*, and the gamma rays emitted during the decay of this excited state to ^{81}Kr are used to image respiratory systems. The resulting ^{81}Kr was determined to be the smallest of the anthropogenic contributions in (24) extrapolating from an inventory based on estimated ^{81}Rb production in the United Kingdom from 1975 - 1996. The expected contribution was on the order of 10^{19} ^{81}Kr atoms. Since there has been no significant expansion of this technique after this inventory was taken, we continue to consider this contribution as negligible for our purposes.

Nuclear fuel reprocessing, by which spent nuclear fuel rods are recycled, requires the chemical processing of these fuel rods, causing a release of trapped gaseous decay remnants. For instance, ^{235}U or ^{239}Pu fissions produce ^{85}Kr and other short-lived isotopes which decay to ^{85}Kr. Since ^{85}Kr has a half-life of 10.76 years, the majority of it has not decayed by the time the rods are processed. At that point the trapped ^{85}Kr is released into the atmosphere. Reprocessing has had an enormous effect on the isotopic abundance of ^{85}Kr in the atmosphere, increasing the ratio over the natural equilibrium in the atmosphere by over four orders of magnitude in the last sixty years (10).

^{81}Kr production due to reprocessing is strongly suppressed compared to ^{85}Kr. ^{81}Kr has a substantially lower neutron-induced-fission yield and is shielded from the decay chain of neutron-rich mass 81 isobars by stable ^{81}Br. Moreover, the natural equilibrium of ^{81}Kr/Kr in the atmosphere is also greater than that of ^{85}Kr/Kr due to the the longer half-life. It nonetheless remains a potential anthropogenic contribution. In (24), ^{85}Kr activity determined in 1985 by (42) is doubled to produce an estimate of ^{85}Kr atoms produced by nuclear fuel reprocessing up to the present day. Then the ratio of the neutron-induced fission yields between ^{81}Kr and ^{85}Kr was used to determine the resulting number of ^{81}Kr atoms. We follow the approach of (24), but consult a more recent and extensive inventory of ^{85}Kr production in (10) to determine a cumulative ^{85}Kr emission up until 2002[2] of 11,800 PBq, equivalent

2. As we will discuss in Section 4.3, the krypton from the modern era used to compare with pre-nuclear

to 5.8×10^{27} ^{85}Kr atoms. Applying the ratio of neutron-induced fission yields from (43) of 6.9×10^{-3} for ^{85}Kr and 2.4×10^{-9} for ^{81}Kr gives 2.0×10^{21} ^{81}Kr atoms. This is equivalent to a $\sim$0.003% anthropogenic signal, which is much smaller than we expect to detect.

4.2.2 Nuclear weapons testing simulations

The largest and most complex source of anthropogenic ^{81}Kr is the testing of nuclear devices in the atmosphere. When a nuclear device detonates, products of the fission or fusion processes are released along with cascades of neutrons. Some of the daughter isotopes from fissions can be ^{81}Kr atoms, and thus contribute directly to the anthropogenic signal. However, much more importantly, the released neutrons can be captured (or scattered to lower energies and subsequently captured) by ^{80}Kr and ^{82}Kr atoms in the atmosphere resulting in reactions that also produce ^{81}Kr.

Calculations in (24) determined ^{81}Kr production from the ^{80}Kr(n,γ)^{81}Kr reaction by examining the well-measured nuclear testing contribution of ^{14}C from ^{14}N(n,p)^{14}C, which is caused by the same cascade of neutrons, and using the ratio of the thermal cross-sections between the two reactions. For ^{81}Kr production from the ^{82}Kr(n,2n)^{81}Kr reaction, a similar approach was applied, but instead using the anthropogenic contribution of ^{39}Ar from ^{40}Ar(n,2n)^{39}Ar reactions and assuming the cross-sections for both reactions to be equal.

Our theoretical model takes a more direct approach of determining ^{80}Kr(n,γ)^{81}Kr and ^{82}Kr(n,2n)^{81}Kr reaction rates per neutron released from the different types of nuclear devices. This approach accounts for the varying cross-sections of these reactions over the whole energy range of released neutrons and does not rely upon measurements made on other elements (i.e. ^{14}N and ^{40}Ar). We calculate these reaction rates by simulating neutrons from a nuclear weapon source at the center of a 1km radius sphere in air using the Monte Carlo N-Particle transport code (MCNP) (44).

---

krypton was sampled from the atmosphere no later than 2002, and thus this calculation represents the largest possible contribution that we can measure.

We define the chemical composition of air in our simulation using the breakdown by volume given in (45). We also allow for the addition of 0-5% water by volume, which replaces the other constituents proportionally and represents the varying moisture in the air given by humidity (46).

The spectrum of fission-produced neutrons can be approximated by a Watt spectrum (47), defined as

$$f(E) = Ce^{\frac{-E}{a}} \sinh(bE)^{\frac{1}{2}} \tag{4.1}$$

where E is the outgoing neutron energy in MeV; a and b are parameters that depend on the incident neutrons energy and the isotope undergoing fission, in units of MeV and MeV^{-1}, respectively; and C is a normalization constant. For these calculations, we used the MCNP default values of a and b which represent an average over incident neutron energies and fissioning nuclei, since the values for specific neutron energies and target nuclei do not vary the results (i.e. nuclide production rates) significantly. MCNP uses continuous-energy neutron transport to determine the neutron fluence rate as a function of energy down to thermal energies, and computes nuclide production rates from the energy-dependent fluence rate and the energy-dependent cross-sections.

For fusion sources we also use the MCNP, but must consider a different neutron spectrum. In fusion weapons the bulk of the thermonuclear energy is produced by four reactions (48)

$$\text{D} + \text{D} \rightarrow {}^3\text{He}\ (0.82\text{MeV}) + n\ (2.45\text{MeV}) \tag{4.2}$$

$$\text{D} + \text{D} \rightarrow \text{T}\ (1.01\text{MeV}) + \text{H}\ (3.02\text{MeV}) \tag{4.3}$$

$$\text{D} + \text{T} \rightarrow {}^4\text{He}\ (3.5\text{MeV}) + n\ (14.1\text{MeV}) \tag{4.4}$$

$$\text{D} + {}^3\text{He} \rightarrow {}^4\text{He}\ (3.6\text{MeV}) + \text{H}\ (14.7\text{MeV}) \tag{4.5}$$

where reactions (4.2) and (4.3) are chiefly used to breed helium-3 and tritium for reactions (4.4) and (4.5).[3] In order to reach high enough temperatures for these reactions to begin,

3. There are obviously a number of other reactions, however, given their relatively lower cross-sections

Fissile Isotope	Direct ^{81}Kr Yields		
	Thermal	Fast (1 MeV)	High (14 MeV)
^{235}U	9.4×10^{-12}	5.5×10^{-12}	3.7×10^{-9}
^{238}U	n/a	1.1×10^{-13}	1.4×10^{-10}
^{239}Pu	2.1×10^{-9}	4.4×10^{-10}	1.8×10^{-8}

Table 4.1: Fission yields used for anthropogenic ^{81}Kr production calculations from (43)

a smaller fission bomb boosted by the presence of deuterium and tritium gas is first detonated within the fusion device (50). We will assume that the energies and products of this smaller fission device are consumed by the fusion fuel and ignore them for the purposes of our calculation. The fusion fuel is typically lithium deuteride (50), which provides not only deuterium, but lithium-6 and lithium-7 that react with neutrons and breed tritium as well (51). Since we are only interested in situations where net neutrons are produced we consider only equations (4.2) and (4.4), which produce what we call DD (deuterium-deuterium) and DT (deuterium-tritium) neutrons respectively. We consider them to be mono-energetic neutrons[4] which have the energies shown in equations (4.2) and (4.4).

Using these three source spectra (Watt, DD, DT) and our dry to humid atmosphere, we calculate ^{80}Kr(n,γ)^{81}Kr and ^{82}Kr(n,2n)^{81}Kr reaction rates for various situations, and then simply multiply by the total number of source neutrons in each situation. From 1945 - 1993, fission tests produced the equivalent energy of 217 Megatons of TNT and fusion tests produced 328 Megatons over 520 atmospheric tests (52). There are additional underground tests equivalent to 90 Megatons of TNT that we neglect due to the comparatively small interaction of neutrons with the atmosphere from such tests. For fission tests, we assume 2.5 neutrons produced per fission and 200 MeV expended per fission to determine the number of neutrons. For fusion, we assume 17.6 MeV per DT neutron and 7.3 MeV per DD neutron[5]

(49) we can ignore them for our purposes.

4. They have an energy width of order $\sim$ 100 keV (51), which is negligible for our purposes given their high mean energies.

5. The 7.3 MeV energy used is the combined total energy of equations (4.2) and (4.3) since they have comparable reaction rates.

Source	^{80}Kr(n,γ)^{81}Kr	^{82}Kr(n,2n)^{81}Kr	direct fission	% of cosmogenic ^{81}Kr
Fission	3.5×10^{22}	8.5×10^{17}	2.9×10^{19}	0.050%
Fusion				
DT	4.6×10^{22}	1.8×10^{22}	n/a	0.066%
DD	2.4×10^{21}	n/a	n/a	0.003%
^{238}U	2.6×10^{22}	6.4×10^{17}	3.2×10^{18}	0.037%
Total	1.1×10^{23}	1.8×10^{22}	3.2×10^{19}	0.15%

Table 4.2: Calculated ^{81}Kr atom production by source due to nuclear device detonation (1945-1993)

and treat DT as 100 times more likely than DD, due to the larger cross-section (48) and the assumption of sufficient tritium availability from lithium reactions. Note that we are considering that the entire explosive yield is generated purely from these fusion reactions, which is an overestimate, but gives a higher upper limit, which we prefer. According to (50), 50% (or more) of the energy released in a thermonuclear fusion weapon is generally from the high-energy-neutron-induced fission of natural uranium (that we will consider to be purely ^{238}U) which is packed into a shell around the whole fusion weapon, so we include that in our calculations as well. Finally, for each fission (whether from fission weapons, or this uranium shell in fusion weapons), we applied direct fission yields of ^{81}Kr from (43) shown in Table 4.1. The error on the reaction rates is $\pm$5%.

We provide the final results of our calculations in Table 4.2, aiming to achieve the highest-bounding estimate. Thus the results shown are obtained using the dry air variants (since they produce the higher yields by a factor of 1.2-1.4 against the most humid cases), and applying the ^{239}Pu yields for neutron-induced fission in Table 4.1 (which are two orders of magnitude higher than ^{235}U yields). In total, nuclear weapons testing provides a ^{81}Kr anthropogenic signal of $\leq$0.15%, two orders of magnitude higher than the estimate in (24) due to our accounting for the cross-sections of the reactions over all energies and applying spectra for different devices.

As a check of the validity of our model, particularly in light of our considerable increase over the previous estimate, we also calculated reaction rates for ^{14}N(n,p)^{14}C and

^{40}Ar(n,2n)^{39}Ar in order to compare our model's calculations for anthropogenic ^{14}C and ^{39}Ar production against experimentally measured values reported in (24). We find that, even in this highest bounding limit scenarios, the model agrees with the anthropogenic ^{14}C and ^{39}Ar abundances cited in (24) within a factor of 2.

4.3 Comparison of Modern and PreAnthropogenic samples

To place an improved limit on anthropogenic Kr-81 in the atmosphere, we use ATTA to measure the ^{81}Kr/Kr isotopic ratios in two different samples: one from air before the advent of human nuclear activity ("PreAnthropogenic"), and one representing the isotopic abundances in modern air ("Modern"). Any difference in the ratio between these two samples would be interpreted as the anthropogenic contribution to our atmosphere. The PreAnthropogenic sample was prepared at the University of Bern from air in 1944 (53). LLC performed at the University of Bern shows the ^{85}Kr activity of this sample to be <1.0 decay per minute per cubic centimeter krypton at STP (dpm/cc). The Modern sample is a commercial bottle of krypton gas purchased in June 2002 and filled at the AGA/Linde facility in Maumee, OH. This Modern sample is actually our reference gas. However, by measuring it separately as a sample and comparing it with the PreAnthropogenic sample, we can ignore the open mode/closed mode systematic corrections described in Chapter 3.4.

Although these commercial gases are extracted from air, the exact time of separation is unknown. To ensure that this krypton gas is representative of modern air, we performed LLC at the University of Bern in March 2016 to determine the ^{85}Kr activity. We measured an activity of 32.1 $\pm$ 1.2 dpm/cc. Using the values from (10) and extrapolating the activity of our krypton gas backward in time, we find it to be consistent with krypton taken from the air in 2002.

Measurements for this experiment were taken over the course of a two-and-a-half-month period. Nine measurements were conducted for each of the two samples to obtain sufficient statistical precision for a 1% measurement (in effect, we conducted a measurement on two

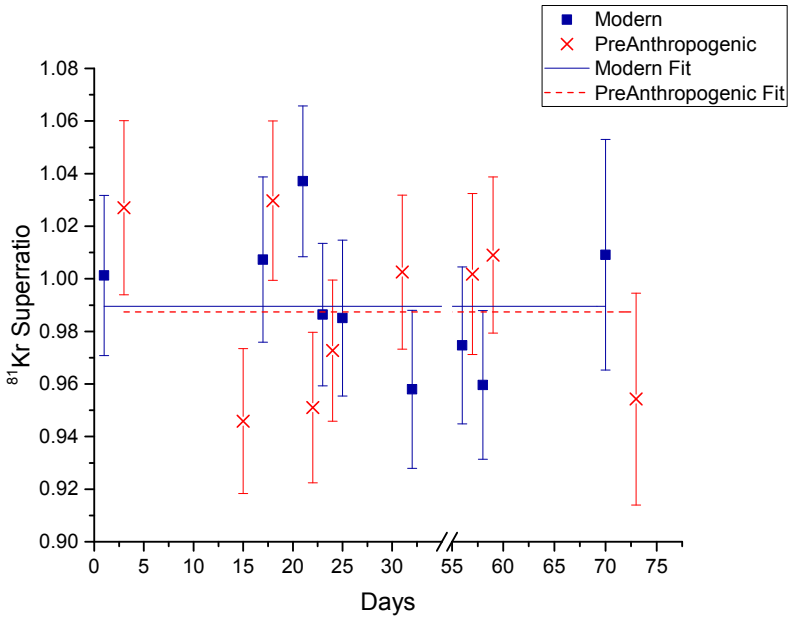

Figure 4.1: Superratios for ^{81}Kr in both "Modern" (blue squares) and "PreAnthropogenic" (red crosses). The weighted average of the Modern samples (solid blue line) is 0.990 ± 0.010 with a reduced chi-squared of 0.73. The weighted average of the PreAnthropogenic samples (red dashed line) is 0.988 ± 0.010 with a reduced chi-squared of 1.16. The weights are determined by the experimental error on each run.

100 μL samples, following the terminology from Section 3.5). Major realignment of the laser system was done at several junctures throughout the period, but never in between sample and reference measurements. Argon was used as the wash gas throughout the measurement period. The results of these measurements are presented in Figure 4.1.

We see that the two weighted averages agree within error, meaning that we have no significant anthropogenic contribution. Consequently, we report a 2.5% upper limit at the 90% confidence level on anthropogenic contributions to the atmospheric abundance of ^{81}Kr, in good agreement with our theoretical model. This measurement both increases our understanding of the anthropogenic impact on isotopes in the atmosphere and removes the potential systematic that human activity has on dating old groundwater at this level of precision. Note that the weighted averages are consistent with the ^{81}Kr superratio reported in Section 3.4.2 and shown in Figure 3.8, because an argon wash was used during this experiment.

This experiment also gives a nice opportunity to check our handling of cross-sample contamination since we know the ^{85}Kr activity of both our samples from LLC. Our outgassing tests on the stable isotopes of krypton prior to each run set a limit of 0.5% contamination per hour. Additionally, we can here also compare the ^{85}Kr loading rates from each measurement. On average the Modern ^{85}Kr loading rate was 8740 atoms/hour and the PreAnthropogenic ^{85}Kr loading rate was 150 atoms/hour. Presuming that all of the activity measured in the PreAnthropogenic sample was from the Modern gas suggests that we have a 1.8% maximum contamination effect. Given the average runtime of 3.5 hours for the PreAnthropogenic runs, this result agrees with our outgassing test limit of just below 2%.

CHAPTER 5

^{85}KR DEVELOPMENT: RAPID-PROCESSING PROCEDURE

This Chapter is adapted from J. C. Zappala, K. Bailey, P. Mueller, T. P. O'Connor, and R. Purtschert. Rapid processing of ^{85}Kr/Kr ratios using Atom Trap Trace Analysis. *Water Resources Research* **53**, 10.1002/2016WR020082 (2017).

5.1 Improving ^{85}Kr measurements on ATTA

The noble gas isotope ^{85}Kr is a radioactive nuclide with a half-life of 10.739 ± 0.014 years (8). It occurs naturally in the atmosphere, produced by cosmic radiation, but at a rate four orders of magnitude lower than current global emission from nuclear fuel reprocessing (10). Due to this anthropogenically increased abundance in the atmosphere and a precise understanding of its input function, ^{85}Kr can be applied as a tracer to date young groundwater or ice on the order of 5-50 years old.

Tracers in this age regime are crucial to water resource management given the global increased dependency on groundwater, including instances of complete dependency on young, shallow groundwater for drinking water (54). ^{85}Kr provides an excellent complement for determining ages when taken with other existing tracers in this age regime, such as chlorofluorocarbons (CFCs) (55) and ^{3}H/^{3}He, which have both independent input functions and and corrections from ^{85}Kr (56; 57). Moreover, CFCs are subject to local contamination (58) and ^{3}H/^{3}He-dating is highly sensitive to natural degassing (57). In contrast, ^{85}Kr is steadily released into the atmosphere in a manner that is both monitored and well understood (10), making it a robust tool for dating. ^{85}Kr also has a number of applications beyond groundwater dating, such as monitoring air for nuclear fuel processing activities (59; 60), monitoring gas transport in the unsaturated zones (which can differ significantly from water transport) (55), and as a tracer of ocean water ventilation and shallow mixing (61).

As a tracer for dating groundwater, ^{85}Kr has been successfully applied on many occasions

using low-level gas proportional counting (LLC), both on its own (62) and in conjunction with other isotopic tracers for deconvolving the age distributions of mixed groundwater (63; 64; 65; 66; 67; 68). ^{85}Kr samples are collected by degassing groundwater samples in the field, and then separating krypton from the bulk gas in the laboratory (69). Recent developments have both decreased separation times and increased krypton yields of groundwater samples. 10 μL of krypton gas (STP) can be purified in the laboratory from 10 L of air in approximately 75 minutes. In the field, this amount of air can typically be degassed from 100 L of groundwater in 30-60 minutes (70). However, despite these improvements, ^{85}Kr-dating has not been applied routinely at a large scale due to the slow processing time and comparatively large sample volume requirements of LLC (71; 72). Our goal is to use ATTA to provide the necessary tool to make large scale analysis of ^{85}Kr viable, by developing a rapid-processing procedure for measuring *only* ^{85}Kr/Kr ratios in our sample (skipping ^{81}Kr analysis).

The remainder of this Chapter describes this new methodology for ^{85}Kr analysis through ATTA. We demonstrate that, by using this method on our improved ATTA-3 system, we now have the ability to continuously measure ^{85}Kr/Kr ratios with 3-5% one-sigma relative uncertainty every 4 hours, on average, increasing the sample throughput by a factor of twelve from (23). We do so with no increase in sample size requirements. We show this method to be linear and repeatable, and present an understanding and control over systematic effects due to cross-sample contamination on the 0.8% level.

5.2 Rapid-processing procedure

Since ^{85}Kr/Kr isotopic abundances are 10 times higher than ^{81}Kr/Kr, simply applying a routine measurement to only ^{85}Kr/Kr would have sufficient statistics to reach a level of 2 - 3% error in 15 minutes, commensurately reducing the amount of krypton being embedded in the system during such a short run. To further improve the time requirements, we can also remove the ℓN_2 cooling from the source. This will increase the mean velocity of the atoms, reducing the efficiency of our trap by a factor of 4, lengthening the measurement time to

Table 5.1: Krypton calibration samples measured using LLC, ATTA, and the new rapid-processing procedure.[a]

	LLC Activity[b]	ATTA $^{85}Kr_{SR}$	Rapid ATTA $^{85}Kr_{SR}$ (raw)	Rapid ATTA $^{85}Kr_{SR}$ (corrected)[c]
J5	269 ± 13	8.0 ± 0.5[d]	7.7 ± 0.3	7.8 ± 0.3
J4	36.2 ± 3.1	1.04 ± 0.03	1.09 ± 0.05	1.09 ± 0.05
J3	32.1 ± 1.2	0.94 ± 0.01	0.95 ± 0.05	0.95 ± 0.05
J2	18.2 ± 0.6	0.53 ± 0.02	0.54 ± 0.03	0.54 ± 0.03
J1	8.9 ± 0.4	0.25 ± 0.01	0.26 ± 0.02	0.25 ± 0.02
J0	<1.0 (90% C.L.)	<0.013 (90% C.L.)	0.032 ± 0.006	<0.021 (90% C.L.)

[a] All ATTA results are expressed using the superratio (SR) defined in equation (2.11).
[b] Reported in decays per minute per cc of Kr gas at STP, adjusted to 3 March 2016.
[c] Corrected values include adjustment from the contamination model. Raw values do not.
[d] Measured using 1μL of Kr gas to prevent extensive contamination of the apparatus with ^{85}Kr.

1 hour to reach the same level of statistics; however, it saves 2 hours by removing the ℓN_2 heating/cooling cycle.[1]

So, we present a new measurement procedure without liquid-nitrogen cooling for rapid-processing of ^{85}Kr/Kr ratios using the ATTA system. First, in Section 5.3, we describe a contamination model for this new method that allows us to control the systematic effects caused from the residual cross-sample contamination (a new and necessary step given that we have to severely truncate the wash times in order to achieve a measurement every 4 hours, on average). Then we apply that model to six calibration samples measured in a 24-hour period, the results of which we report in Section 5.4. Samples for this experiment were prepared at the University of Bern and ANL. Their activities were measured using LLC at the University of Bern, and their ^{85}Kr superratios were measured using our routine ATTA technique described in Section 2.3. These activities and superratios are reported in the first two columns of Table 5.1, respectively.

For the remainder of the Chapter, all measurements described are done under our liquid-

1. Based on other tests of the implantation effect that we have conducted, there is also an indication that the water frozen onto the source chamber walls during ℓN_2 cooling plays a role in increased krypton implantation.

nitrogen free "rapid-processing" conditions unless otherwise stated. Measurements are conducted in the manner illustrated in Figure 5.1: a sample is measured for ^{85}Kr/Kr for 1 hour, followed by a 2.25 hour argon wash, another 1 hour sample measurement, a 1 hour reference measurement, and finally another 2.25 hour argon wash before the cycle is repeated. This timing permits us to measure the ^{85}Kr/Kr ratio of one sample every 4 hours, on average. To define a shorthand for the following sections, a measurement of "S_1-S_2-R", would mean a measurement of S_1 as the first sample and S_2 as the second, followed by a reference measurement R. During the sample measurements, gas is recirculated in the closed mode configuration. During the washes and the reference measurements, the gas is flowed continuously and discarded in the open mode.

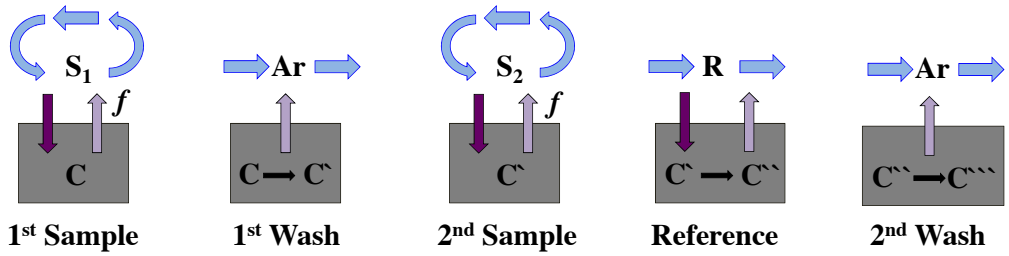

Figure 5.1: A diagram for the sequence S_1-S_2-R. During sample measurements, there is gas exchange between the contaminant in the chamber wall and the sample gas, which is being recirculated. During washes, argon gas is flowed through the system without recirculation, removing some contaminant. During the reference measurements, reference gas is flowed without recirculation. It enters the chamber walls and reduces the presence of the previous contaminant simultaneously. The contaminant changes in each step as described by our model (see text for details).

5.3 Contamination model

We here present a more advanced model for our cross-sample contamination than in Section 2.5. Although some comments and equations are repeated, we do so to present a full and coherent explanation of the model that we apply. Although we do not apply this model in general to routine ATTA procedures with ^{81}Kr-dating, we could do so by measuring the same calibration samples in the manner to be described, but in the normal measurement

mode. Note that this is meant to be a simple but reliable *empirical* model that quantitatively describes the data without going into the complexities of the cross-contamination mechanism such as specific implantation sites and chamber volumes.

Following the diagram in Figure 5.1, we consider the collective surfaces of ATTA-3 affected by implantation and the volume of sample gas to be two distinct reservoirs. The former is filled with contaminant from previous samples and the latter is filled with our sample to be measured. The contaminant has its own ^{85}Kr/Kr ratio, which we define as C. Due to the plasma discharge there is an exchange: sample gas enters the surface reservoir and contaminant leaks into the volume of the sample gas. The contamination that leaks into the sample becomes part of our measured value. The sample which enters into the surfaces replaces some fraction x of the current contaminant in the reservoir, reducing the influence of each previous sample's contribution to the contaminant by some fraction 1-x. The wash procedure afterward reduces the overall number of contaminating krypton atoms by replacing them with argon atoms. However, the wash does not alter the ^{85}Kr/Kr ratio of the contaminant since it affects all implanted krypton isotopes equally. Thus, if there is some contaminant C before S_1 is measured, then after the wash we now have a contaminant

$$C' = C(1 - x) + S_1 x \tag{5.1}$$

We test such a model by attempting to find a repeatable value for x. This x is particular to our current vacuum system and requires reevaluation if changes are made to the chamber.

To find x we first need to know how much contamination we have in our system. We define f, the average fraction of the sample (S) volume that is replaced by the contaminant (C) during a measurement of the sample (M_S) as

$$M_S = (1 - f)S + fC \qquad \text{where} \qquad f = \frac{\frac{1}{2} t R_{\mathrm{Kr}}}{P_{\mathrm{avg}}}. \tag{5.2}$$

Here t is the length of the measurement, R_{Kr} is the linear outgassing rate of the contaminant,

and P_{avg} is the average partial pressure of krypton during the run. The factor $\frac{1}{2}tR_{\text{Kr}}$ gives us the integrated contamination injected into the gas volume, which is normalized by the partial pressure of krypton, P_{avg}. The only unknown here is the outgassing rate. To determine the rate we regularly conduct an outgassing test prior to each measurement: the system is filled with argon gas and the gas is recirculated with the plasma active. We then measure how much krypton leaches out of the wall over a few minutes using our RGA and extrapolate a krypton outgassing rate due to the argon discharge, R_{Ar}. However, we need to determine the krypton outgassing rate in the presence of a krypton discharge, which should be proportional, but not equal to the rate we have measured, i.e. $R_{\text{Kr}} = bR_{\text{Ar}}$.

To determine b, we first clean the system for longer than the normal wash period such that the outgassing rate is more than a factor of 4 lower than the typical rates we expect in these measurements. In this "clean start," if we measure S_1-S_2-R, then the contaminant $C \approx S_1$ when we measure S_2. Accordingly we obtain

$$M_{S_2} = (1-f)S_2 + fC = (1-f)S_2 + fS_1$$

Using our calibration samples, we start with a clean system and then measure J5-J0-R. This simplifies the above equation even further, since J0 is devoid of ^{85}Kr ("^{85}Kr-dead") and thus $S_2 = 0$. With only the second term, we can solve for b. We used three such measurements to determine that $b = 2.4 \pm 0.3$.[2]

Now that we know the value of f, we can work to find x by applying the model. If we consider measuring S_1-S_2-R-S_3 with our clean start, the model gives us the following for the

2. For xenon, $b = 2.0$, hence the factor of 2.0 mentioned in Section 2.5.

third sample measurement

$$\begin{aligned} M_{S_3} &= S_3(1-f) + fC'' \\ &= S_3(1-f) + f(C'(1-x) + Rx) \\ &= S_3(1-f) + f(S_1(1-x) + S_2x)(1-x) + Rx) \end{aligned}$$

From here, we can solve for x. We ran two separate sequences, J2-J5-R-J0 and J5-J0-R-J0-J0, to solve for x and found that $x = 0.60 \pm 0.02$. Note that we have considered the reference to both be a sampling *and* a wash procedure. Yet, despite it only being 1 hour instead of 2.25, we still found consistent results. The reason is that, as shown by solving for b, a krypton wash is $\sim$2.4 times more effective at extracting krypton than an argon wash. As such, we could increase the efficiency of the wash by using ^{85}Kr-dead krypton gas as our wash gas. However, sufficient amounts of ^{85}Kr-dead krypton gas are not readily available.

With this repeatable value for x we have determined a simple and consistent model for describing our contamination in this rapid-processing mode.

5.4 Demonstration of rapid-processing

We measured six calibration samples in a 24-hour period (measured in the order J2-J5-R-J0-J4-R-J1-J3-R). The ^{85}Kr superratios determined from these measurements are listed in Table 5.1 in the third column, and listed with corrections from the contamination model in the fourth column. The LLC activities of the samples are plotted against these corrected values in Figure 5.2 and fit to a line. The measurement of J0 does not appear in the figure due to the $\log_2$ scaling, but is included in the fit. The reduced chi-squared of the fit is 0.2. We also see that in the six samples we measured the contamination fraction per sample saturated below the 2.5% level, as seen in Figure 5.3. Based on this saturation level and the errors of our contamination model, the correction will add a maximum error of 0.8% to the ^{85}Kr/Kr isotopic abundance measurements, which typically have 3-5% statistical error.

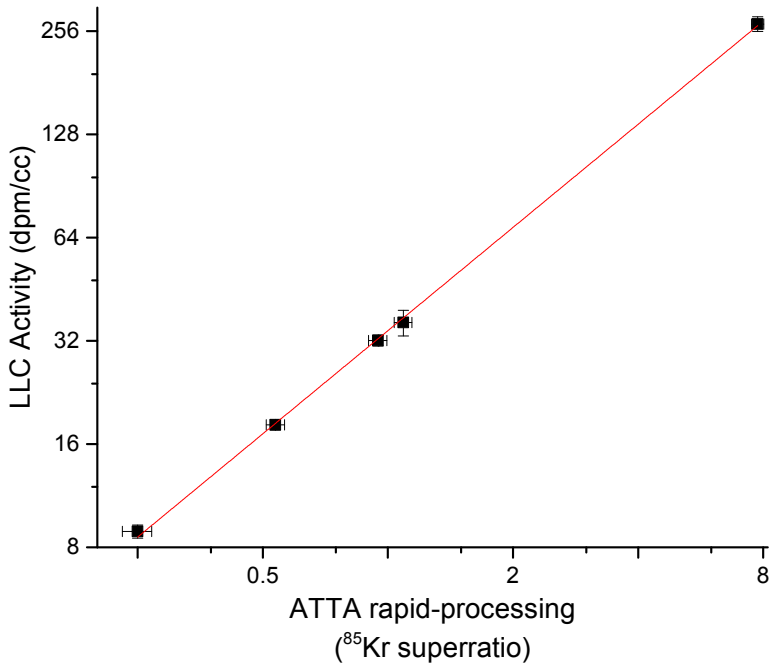

Figure 5.2: A demonstration of linearity for rapid-processing superratio measurements on ATTA via comparison with LLC results. Both axes are drawn on a $\log_2$ scale. J0 was measured to have a superratio of <0.021 (90% C.L.), but is not shown due to the log scale. The fit has a reduced chi-squared of 0.2.

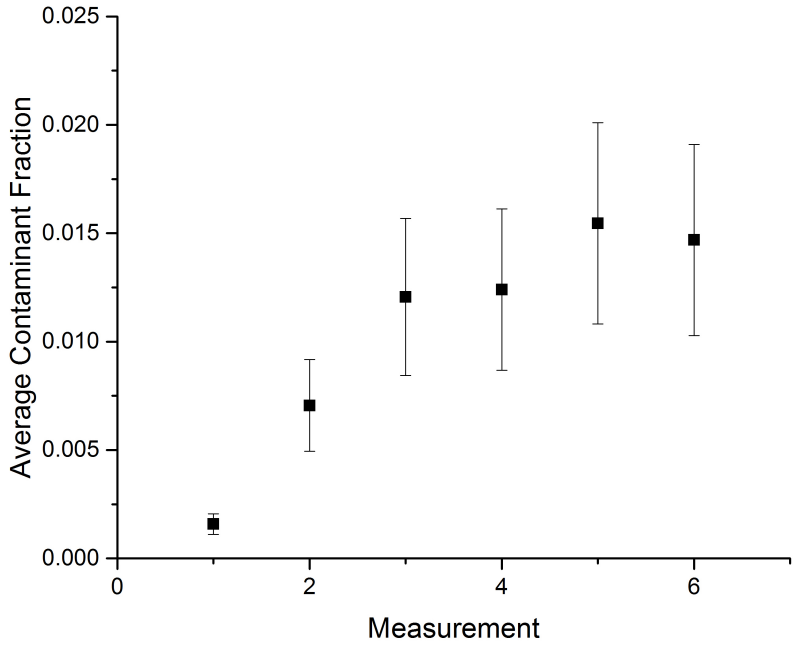

Figure 5.3: Average contamination fractions during each measurement over six sequential measurements during a 24-hour period.

The rapid-processing measurements' agreement with typical ATTA measurements and their linear relationship with LLC activities, demonstrates the validity of this approach. This method increases the throughput of ^{85}Kr/Kr isotopic abundance measurements on a single ATTA system by a factor of twelve. The agreement of this calibration over such a large range of activities (J5 being nearly 4 times higher than the typical 75 dpm/cc activity in the atmosphere of the northern hemisphere (10)) also shows that our contamination model can even handle enrichment levels we would normally wish to avoid in the standard ATTA system. With this rapid-processing procedure validated, ATTA is ready to increase the capacity for ^{85}Kr-dating for the geoscience community.

CHAPTER 6

APPLICATIONS WITH ATTA-3

6.1 Survey of measurements and applications

Alongside our development efforts, we have also continued serving environmental (and other scientific) applications using the continually improved ATTA-3 system at ANL. Our applications have focused on pursuing a better understanding of groundwater transport processes for flow modeling and groundwater management, but have ranged into other applications as well. We will here detail many of the various projects for which samples have been measured during the period of this disseration's ATTA analysis work, i.e. May 2014 - February 2017. ^{81}Kr and ^{85}Kr analysis from this period which were officially submitted to collaborators are included in Appendix C. Several ongoing projects do not yet have officially submitted results because sampling, measurement and/or analysis is on-going as of this writing (March 2017). Results from those projects are not included in Appendix C. The described projects follow chronologically by the time of their samples' measurements on ATTA-3, excluding the Israel campaign, which is described in detail in Section 6.2, and a sample from the Beatrix gold mine in South Africa discussed in Section 6.3. Also omitted from the list are several measurements for which the data either did not prove useful in improving scientific understanding or for which contamination issues were later discovered to have occurred during sampling.[1]

- Baltic Artesian Basin (BAB): ^{81}Kr-dating through ATTA, as well as other noble gas analysis, was performed on groundwater on the deepest aquifer system of the Baltic Artesian Basin with the goal of understanding the flow dynamics of the system, which occur on a timescale of several hundred thousand years. The system mixes interglacial meteoric water, glacial meltwater, and an old brine component. ^{81}Kr-dating

1. Those results are also omitted from Appendix C.

was specifically applied to estimate the age of the end-members involved in the mixing. ^{81}Kr ages ranged from 300 kyr to 1.3 Myr for interglacial meteoric water and glacial meltwater. For the brine component, ages actually exceeded the dating range of the ATTA-3 instrument at the time of measurement, providing an age limit of >1.3 Ma (73).

- International Atomic Energy Agency (IAEA): The IAEA is conducting a thorough survey of ancient groundwater aquifers throughout the world. ^{81}Kr-dating on ATTA has been carried out on samples from Vietnam, Argentina, Estonia, Hungary, and Tunisia. Measurements on samples from Thailand are on-going, and more measurements are expected in the future. Detailed hydrological analysis of these results is also on-going.

- Krypton neutron capture cross-sections: Neutron capture cross-sections of krypton and xenon isotopes are of special interest for *s*-process nucleosynthesis. However, determining these cross-sections through abundance measurements in primitive meteorites has proven impossible and so a more direct measurement has been sought (74). ATTA can provide this for the ^{80}Kr(n,γ)^{81}Kr and ^{84}Kr(n,γ)^{85}Kr reactions by measuring isotopic abundances in a sample of krypton gas which has undergone controlled neutron irradiation and comparing those abundances with the pre-irradiated levels. Neutrons are provided by a compact liquid-lithium target (LiLiT) at the Soreq Nuclear Research Center. The lithium target, bombarded by the high-intensity proton beam of the Soreq Applied Research Accelerator Facility (SARAF), constitutes an intense source of neutrons with energies ranging up to 200 keV produced by the ^{7}Li(p,n)^{7}Be reaction for nuclear astrophysics research (75). While one irradiated sample has been measured on ATTA-3, a second sample, irradiated at a different energy, needs to be measured to account for background effects due to high-energy gamma rays.

- Fukishima effects on Chicago air (Official results not yet submitted): 30 individual air samples were taken from once every few days (earlier in the period) to once every

three weeks (later in the period) nearby the University of Chicago, IL, U.S.A. between 15 March 2011 and 4 January 2012 to measure a possible signature of the Fukishima incident (which first began 11 March 2011) on the atmospheric ^{85}Kr abundance. The goal is to use ^{85}Kr-analysis on ATTA to trace the Fukishima plume over North America. Five samples have been measured and there is an apparent peak in ^{85}Kr-activity of 10 - 15 dpm/cc over the average value of 74 dpm/cc, but further measurements are required to ensure that this is not a random fluctuation.

- Paris Basin (Official results not yet submitted): This 110,000 km^2 bowl-shaped basin in France provides fresh drinking water, high-grade oil, and geothermal energy. Its sedimentary layers constitute relatively simple stratigraphy, facilitating numerical model studies, and predictive assessments of fluids movement. As such it has been intensively studied to understand not only crustal fluid flow but also as a potential nuclear waste repository (76). ^{81}Kr can prove to be a significant aid to these studies; already a preliminary sample from a deep geological nuclear waste repository site was measured to have a ^{81}Kr age $>$ 1 Myr. This result implies that, even if the radioactivity leaked from the clay formation, the hydraulic conductivity is so low that said leak will not easily be spread by water advection.

- Floridan Aquifer: The Floridan Aquifer System is one of the most productive aquifers on Earth, underlaying the entire state of Florida and beyond. Based on noble gas recharge temperatures it is suggested that the Upper Floridan Aquifer was recharged during the last glacial period (LGP), and that the sea water intrusion in the Lower Floridan Aquifer was triggered by the holocene sea-level rise (77), both important conclusions in understanding the effects of a shifting climate on the hydrological cycle. Because ^{14}C activities are compromised by water-rock interactions in this carbonate aquifer system, we analyzed ^{81}Kr to validate these conclusions. The apparent ^{81}Kr ages range from modern to 38.5 kyr, confirming the recharge during LGP for most locations.

However, the younger ages near the recharge zone suggest an active hydrological cycle rather than trapped LGP groundwater. Additionally, in the Lower Floridan Aquifer ^{81}Kr can be used alongside other tracers to deconvolve the mixing of older seawater with the intruding Holocene seawater (76).

- Waste Isolation Pilot Plant (WIPP), 2nd campaign: As a follow-up to the analysis of WIPP related samples described in Section 1.3.1 (26), three further samples were measured, two from low-transmissivity wells (AEC-7R, H-12R) like those discussed in Section 1.3.1, and a third well from a high-transmissivity region (SNL-16).[2] The low-transmissivity wells showed ^{81}Kr-dating results consistent with the first project's measurements (198 (+22/-20) kyr and 269 (+19/-18) kyr) after a small correction using the ^{85}Kr-activity (as described in Section 1.3.1). The high-transmissivity well had a ^{81}Kr/Kr ratio consistent with modern isotopic abundances, as expected. Corrections provided by (78).

- Isodetect GmbH: Samples measured for Isodetect marked the first commercial venture for ATTA-3 at ANL. Isodetect, headquartered in Munich, Germany, is a company that conducts environmental monitoring through isotope analysis, in this case for exploration of young groundwater. We conducted ^{85}Kr-analysis using ATTA-3 on samples provided by Isodetect and purified by the University of Science and Technology in China. The rapid-processing method presented in Chapter 5 was applied to conduct two measurements each day (provided an eight hour work day). The results from the first batch of 10 samples was submitted. Analysis of 9 further samples is on-going.

- Etsch Valley: The deep water in the Etsch Valley in Italy is currently being explored as a potential source of geothermal energy. To better understand its availability and utility as such a source, various measurements are being taken, including ^{81}Kr-dating.

2. In Section 1.3.1, we also mentioned low- and high-transmissivity regions. However, those were relative to one another. Compared to SNL-16 discussed here, both earlier samples were in a low-transmissivity region.

So far a single sample was measured originating from a deep borehole (> 2 km) in the valley, and the ^{81}Kr-age was determined to be 460 (+23/-22) kyr (uncorrected)[3], demonstrating that the age range of the water makes ^{81}Kr an extremely useful tracer in the area for further work.

6.2 Israel groundwater campaign

The Sinai Peninsula in Egypt and the Negev Desert in Israel are located in the global desert belt and lie atop the Nubian Sandstone Aquifer. This aquifer contains over 2×10^{11} m^3 of fresh to brackish water with what is assumed to be almost negligible modern active recharge. The aquifer has clear hydraulic gradients from the southern Sinai sandstone toward the Arava Valley outlets suggesting flow patterns that contradict the relatively homogenous apparent ^{14}C-dating ages of 20,000 - 35,000 years throughout the central Sinai and the Negev Desert, which suggest stagnant groundwater over the entire basin (79). This discrepancy in such a major basin for water resources, especially one that serves the local desert communities, offered a perfect opportunity for large-scale ^{81}Kr-dating given several additional signals that pointed to the potential presence of groundwater beyond 50,000 years old.

We are thus currently participating in a major ^{81}Kr-dating campaign in the Negev Desert and Arava Rift Valley in collaboration with the University of Chicago and Ben Gurion University in Israel. Because our responsibilities in this campaign included both collection of the samples in the field, as well as measurements–and in some case repeated measurements–of samples, a description of our work will offer a rather complete presentation of how one conducts a groundwater dating campaign for analysis through ATTA.

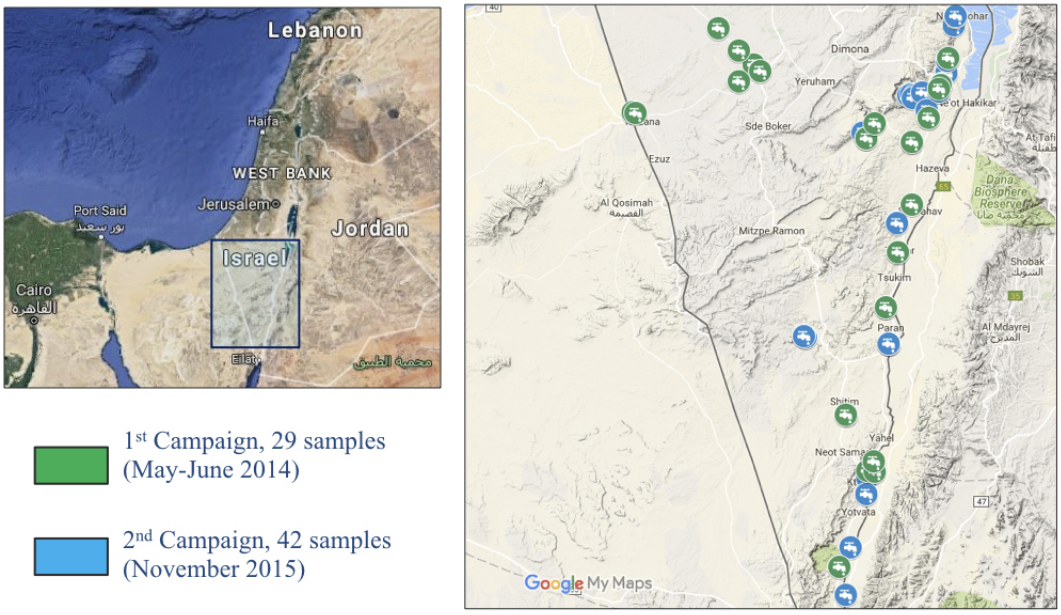

Figure 6.1: Israel groundwater campaign sampling locations in the Negev Desert and Arava Rift Valley. The region of interest (right) is the marked subsection on the larger map of Israel (left). See text for further details on sampling.

6.2.1 Field sampling

Two major field-sampling campaigns have been conducted to date of this diseration. In May - June 2014 we collected 29 samples, and in November 2015 we collected an additional 42 samples. Figure 6.1 shows locations where sampling occurred in the Negev Desert and Arava Rift Valley. Several wells sampled are not shown, as they are outside of this the region of interest, and most of those are located in the Hula Valley, in the northeast of the country. 8 wells from the second campaign are resampled wells from the first campaign.[4]

All of the wells sampled in the region of interest fall into two categories: artesian flowing wells and commercial water production wells.[5] Artesian flowing wells are naturally flowing

3. The sample had a small ^{85}Kr-activity of 3.37±0.31 dpm/cc, but the contamination source has not yet been determined and so a correction has not yet been made.

4. The reasons for resampling are elaborated on in Section 6.2.2.

5. Outside the region of interest, namely in the Hula Valley, a number of the wells were gas production wells. The methodologies for sampling these wells changes depending on a number of circumstances as they suffer from a high relative abundance of natural gases produced by geochemistry versus the trapped air we wish to collect.

wells which occur due to hydraulic pressure from the comparatively high hydraulic head level in the area (that is, compared to the ground level) (1). These wells typically have no further apparatus for pumping the water into our system for sampling and thus additional work is required to move the water into the sampling system. Such a setup for pumping is shown in Figure 6.2 (a), where a pump moves water from a tube inserted several feet into the well towards our system. The vast majority of the wells, however, are commercial water production wells, shown in Figure 6.2 (b). These wells can be tapped directly because of their internal pumping mechanisms which will deliver the water with sufficient pressure to our system. In both cases, we strive to attain a flow rate of 10 - 15 L/min, typically easy for commercial wells, but more difficult to attain for artesian wells.

Ultimately, we wish to collect the air (and more specifically the krypton in that air) that was trapped within the water during exchange with the atmosphere before it entered into the groundwater system. Therefore we must "degas" the water on our sampling system. The system that we use is described fully in (70). An image of this system in active use during field work in Israel is shown in Figure 6.3. We will provide a basic description of the principles of the system here.

Groundwater that is delivered into the system travels through a Liqui-Cel 4 x 13 Extra Flow Membrane Contactor. This device is a stainless steel cylinder which houses a hydrophobic membrane running though its center. The water passes along this membrane, but will not pass through it. However, when vacuum is pulled inside the stainless steel cylinder volume outside of the membrane, then the resulting equilibration of gas phase pressures causes the gas trapped in the water to move from the membrane volume (at 800+ Torr due to the combined atmospheric and water pressures) into the outside volume (kept at 40-200 Torr). This gas is then transfered by a pair of compressors (which thus also maintain the vacuum pressure in the cylinder) to a previously emptied gas cylinder. The 3.8 L cylinder is filled to 4 bar in pressure such that we obtain over 15 L of gas at STP. This requires about 150 L of water and so sampling can be accomplished in about 15 minutes with the flow rate described

(a)

(b)

Figure 6.2: (a) The artesian flowing well (left side of image) flows naturally due to hydraulic pressure. Water is drawn through the black tube inside the well head by the small green external pump (right side of image) to move water to our sampling system through the clear plastic 1/4" tube. (b) This commercial well is exposed above ground only as a long pipe over a foot in diameter. Underground, an internal pump moves the water through this pipe. There are several points where this pipe can be tapped. We have tapped it (upper right hand corner of the image) to take water to our sampling system through the clear plastic 1/4" tube.

Figure 6.3: The groundwater sampling and degassing device in active use during the Israel groundwater sampling campaign. The entire device fits into the back of a truck for ease of transport between wells. See text for sampling details.

(not including time to setup the system at the well, etc.). Higher flow rates are permitted, but with a loss in gas extraction efficiency by the Liqui-Cel device.

The gas that we collect is primarily air, but other gases can be present due to natural underground production and dissolving of other gases into the water. For wells where the gas content is expected to be entirely air, less gas can be taken (using lower pressures or smaller, 1.7 L, cylinders), since we will obtain more than 1 μL of krypton per L (STP) of air.[6] If high dissolved gas content besides air is expected, more sample can be taken. The system's compressors can handle an upper pressure of 5 bar and we have gas cylinders as large as 5.6 L available. The system logs the pressure in the Liqui-Cel membrane, Liqui-Cel cylinder, and the gas cylinder where the sample is collected. The temperature and flow rate of the water are also recorded.

The device, as it appears in Figure 6.3, was kept in the back of an SUV throughout both campaigns for ease of transport between wells.

6. Despite krypton being 1 ppm by volume in air, it is slightly more soluble than nitrogen in water, resulting in an enhancement to about 1.3 μL of krypton per L of air extracted from water.

6.2.2 Krypton analysis on ATTA-3

After each sampling campaign, the gas cylinders were shipped to the University of Bern and the University of Chicago for chemical purification to reduce the order liters air sample to a standard order microliters krypton sample for processing on the ATTA-3 machine at ANL. Since the chemical purification portion of the process was not part of our responsibility for the campaign, the details are not described here. They can be found in (70).

Samples of 5 - 20 μL krypton at STP are prepared and shipped (in sample holders akin to the one shown in Figure 2.12) to ANL for processing through ATTA, as per Section 2.3. The ^{81}Kr-dating results of all the samples measured in the Negev Desert and Arava Rift Valley from the first campaign, as well as those measured for the second campaign as of February 2017, are shown in Figure 6.4. Measurements from the second campaign are on-going. The results are grouped into age range, and the specific ^{81}Kr/Kr values used to produce these dates can be found in Appendix C. Our goal in presenting the values here and in this manner is to demonstrate the variety of groundwater ages that appear in the Negev Desert and Arava Rift Valley beyond what was expected from earlier ^{14}C-dating (and most of which are beyond the ^{14}C-dating range). Through ^{81}Kr-dating we can now resolve these different ages from one another, allowing our collaborators to draw new hydrological conclusions through better informed flow-modeling simulations. A first publication is in preparation (79).

As a further test of the reliability and repeatability of the ATTA technique, as well as our sampling techniques, we analyzed 8 wells twice, once from a sample collected and purified during the first campaign, and another from the second campaign. The ^{81}Kr/Kr and ^{85}Kr/Kr results from both campaigns for 4 of these samples that have already been remeasured appear in Table 6.1. The results, save for Paran 20, show consistency of sampling and measurements, as well as an improvement in precision between the two campaigns, thanks to several of the improvements described in Chapter 3, which were implemented between the two analyses.

Paran 20 is a special case. During the first measurement, there was a non-negligible ^{85}Kr/Kr signal higher than the background suggested by the ^{81}Kr age, but less than the

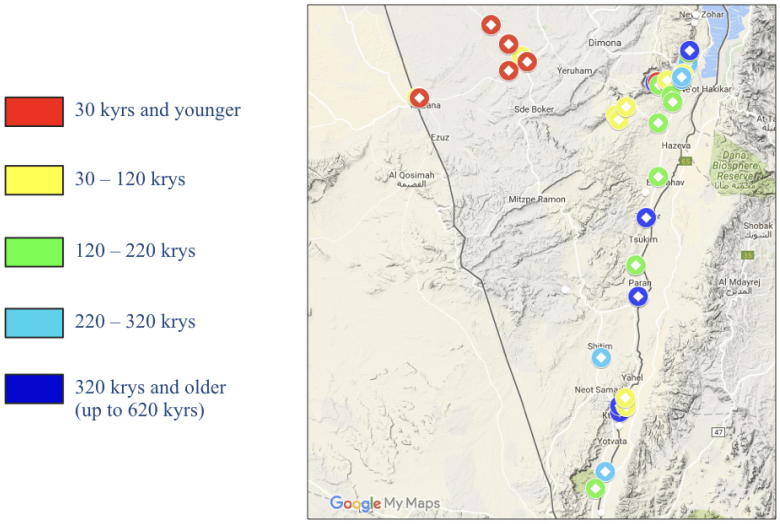

Figure 6.4: ^{81}Kr-dating results in the Negev Desert and Arava Rift Valley for a combined 39 sampled wells between both campaigns. The results are grouped by age range. Those marked in red fall into the 30 kyr and younger range, a range where ^{14}C-dating suggested almost all of the water in the valley belonged. The ^{81}Kr-dating results clearly demonstrate otherwise, showing not only many different ages, but water as old as 620 kyr.

Table 6.1: Results of ^{81}Kr/Kr and ^{85}Kr/Kr analysis from resampled wells, including dates of collection and analysis. All detection limits reported as $< x$ are done with 90% confidence.

Well	First Campaign (May-June 2014)		Second Campaign (November 2015)	
	^{81}Kr/Kr (date collected)	^{85}Kr/Kr^a (date analyzed)	^{81}Kr/Kr (date collected)	^{85}Kr/Kr^a (date analyzed)
Tamar 9	0.75 ± 0.04 (28 May 2014)	< 0.57 (27 Aug 2014)	0.68 ± 0.03 (4 Nov 2015)	< 0.56 (18 Oct 2016)
Tamar 11	0.49 ± 0.04 (28 May 2014)	1.16 ± 0.58 (4 Sept 2014)	0.46 ± 0.02 (5 Nov 2015)	0.34 ± 0.13 (21 Oct 2016)
Gome'e 1	0.30 ± 0.02 (1 June 2014)	0.34 ± 0.25 (24 Apr 2015)	0.313 ± 0.014 (6 Nov 2015)	< 0.64 (4 Oct 2016)
Paran 20	0.56 ± 0.03 (27 May 2014)	5.50 ± 0.46 (19 Dec 2014)	0.346 ± 0.015 (10 Nov 2015)	< 0.47 (30 Sept 2016)

^{a} Reported in decays per minute per cc of Kr gas at STP, adjusted to date of analysis

average value of ^{85}Kr activity in air for the northern hemisphere (75 dpm/cc, from (10)). As discussed in Section 1.3.1, this is typically due to some contamination which we can correct for, if we understand its source. In the case of Paran 20, we were made aware of a failure in the well that could cause the internal pump to draw in air or young groundwater due to abstraction. Unfortunately, we do not know what ^{85}Kr/Kr ratio we should be correcting with, since we do not know if the contamination source is air or young groundwater, and the young groundwater can take any value below the atmospheric activity. Thus, during the second campaign we resampled the well under reduced pumping speed conditions for the internal pump to mitigate this effect. As can be seen in the results from Table 6.1, these new conditions removed the ^{85}Kr/Kr contamination signal, and correspondingly yielded a lower ^{81}Kr abundance.

6.2.3 Hydrological implications

Although it is not under the umbrella of our contribution to the campaign, it is worth briefly noting some of the hydrological implications that can be determined from these results. As discussed in (79), the current results already provide a new understanding of how the aquifer was recharged as well as mixing and flow patterns within the aquifer. Previously, the aquifer was understood to be a stagnant pool recharged during a single event. However, these new ^{81}Kr data give evidence of multiple recharge events and multiple flowlines which underlie a much more complex system. Mapping this now dynamic system is crucial to water management and contamination modeling in the aquifer.

Several samples outside the region of interest shown in Figure 6.1 are of concern for other more specific projects and applications. Measurements taken in the Hula Valley have uncovered nearly 400 kyr old water that was completely unexpected in the area given the understanding of the flow from the country's northern border, which will now require further investigation. Additionally, measurements along the aquifer where it borders the Mediterranean Sea may provide evidence of modern sea water intrusion due to over abstraction of

the various wells along the border; a massive issue for ensuring understanding of the aquifer's fresh and brackish water supply.

6.3 Subsurface production of ^{81}Kr

As discussed throughout this work, one of the greatest strengths of ^{81}Kr as a tracer is the lack of external influences on the ^{81}Kr/Kr ratio in the atmosphere as well as in groundwater. Because of its noble gas nature, there are no geochemical reactions that need be considered or corrected for, as with radiocarbon dating for example. In addition, as we demonstrated in Chapter 4, anthropogenic sources of krypton also do not interfere with our ^{81}Kr-dating efforts. That leaves natural subsurface production of ^{81}Kr as the only remaining source of potential interference. As mentioned earlier, stable ^{81}Br shields ^{81}Kr from the nuclear decay chain of fission products, leaving direct fission to ^{81}Kr and neutron capture on ^{80}Kr as the only two remaining possible production channels. Both channels, on the basis of calculated spontaneous yields and neutron capture cross-sections, respectively, were believed to be far too weak to contribute any detectable production in the course of ^{81}Kr-dating.

However, in 2012 three samples taken from gold and diamonds mines in Witwatersrand Basin, South Africa showed higher than atmospheric ratios of ^{81}Kr/Kr when measured on ATTA (in 2013 - 2014). The mines were Star Diamond, Masimong, and Beatrix and had ^{81}Kr superratios of 2.1, 2.9, and 4.6 (with errors of $\sim$0.2), respectively. Furthermore, each had a non-negligible ^{85}Kr signal, believed to be contamination from air (80). The average ^{85}Kr activity in the mines was measured using LLC and ATTA to be about 70 dpm/cc, and used to correct the ^{81}Kr superratios to 2.6, 3.2, and 4.9. The results, along with the corrections, can be seen in Figure 6.5.[7]

Considering the uranium content of these mines and a simple hydrogeological model for intrusion of fission products into nearby subsurface fluids, such levels of ^{81}Kr enrichment

7. The measurement of a fourth site sampled during the campaign, Finsch BH1, is also plotted. However, it had a ^{81}Kr superratio of less than 1.

suggested direct spontaneous fission yields of 2×10^{-7}, nearly four orders of magnitude higher than the accepted value (80). In order to ensure the validity of these results, and rule out the possibility of enrichment by contamination in the laboratory when the three samples were processed,[8] we sought to produce a second independent measurement at one of the sites which showed these elevated superratios.

The location of the sampling sites made both access and sampling extremely difficult, resulting in a long delay before a new sample could be acquired. However, this measurement finally occurred in February 2017, on a sample taken from the Beatrix mine on June 2016, which has a uranium content of 84 ppm (about 20 times higher than is typical for granitic rock). The results of this new measurement were

$$^{81}\mathrm{Kr}_{\mathrm{SR}} = 3.63 \pm 0.11 \qquad ^{85}\mathrm{Kr\ activity\ } = 23.4 \pm 0.8\ \mathrm{dpm/cc} \tag{6.1}$$

When considering the ^{85}Kr activity as contamination from air–which is expected given the difficulty of sampling mentioned–this result is in good agreement with the previous corrected result from March 2014 from the Beatrix sample taken in August 2012. This agreement can be seen in Figure 6.5.

This independent measurement confirms that subsurface production of ^{81}Kr must be considered in locations with elevated uranium (and potentially thorium) content. However, whether the cause of this enrichment is truly a much higher than calculated fission yield or some sort of second-order effect (e.g. impinging of alphas from uranium alpha decay on light metals in the rock, which would subsequently produce neutrons for neutron capture on ^{80}Kr) remains unknown. As such, further investigation in this area is required in the future.

8. The laboratory where the samples were processed sometimes handles gas with artificially enriched ^{81}Kr/Kr abundances, i.e. having a superratio greater than 1.

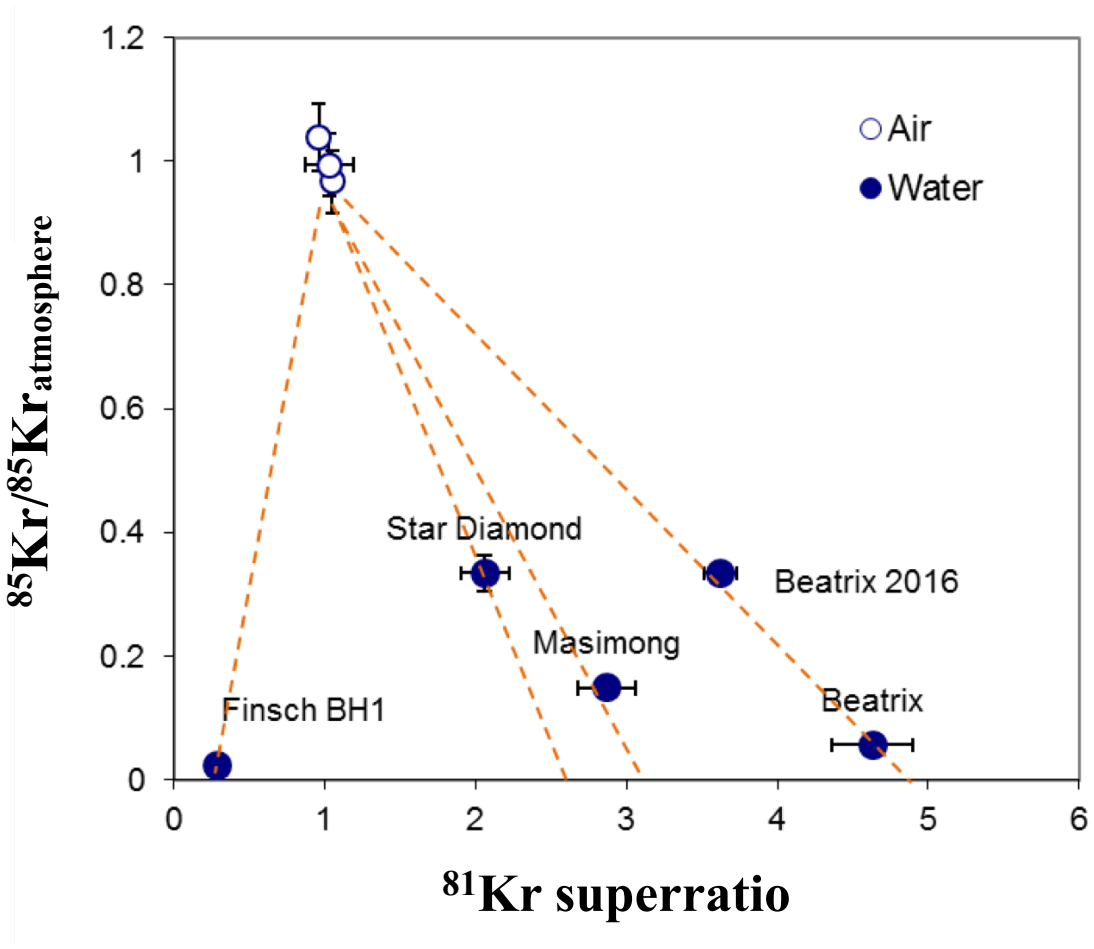

Figure 6.5: ^{81}Kr-dating results for gold and diamond mines in South Africa. The vertical axis represents the ratio of the ^{85}Kr activity of the samples with respect to the ^{85}Kr activity of the atmosphere. The ^{85}Kr activity of the atmosphere was determined by averaging air results shown on the graph as white circles. The points are plotted along the horizontal axis according to their uncorrected ^{81}Kr superratios. The dotted lines indicate admixtures of atmospheric air with a "^{85}Kr free" version of each sample. Both Beatrix values falling along the same dotted line indicates agreement between the two measurements.

CHAPTER 7

NEXT GENERATION ATTA SYSTEMS

Chapter 6 demonstrated a number of applications for ^{81}Kr-dating, ^{85}Kr-analysis, and the ATTA technique and there are a number of projects in preparation that will continue providing samples for measurement on the ATTA-3 system. Additionally, with the advances presented throughout this dissertation, more applications are becoming regularly available, e.g. ice core dating (Chapter 3), high-precision ^{81}Kr-dating (Chapter 4), and large scale ^{85}Kr-dating (Chapter 5). As such, we must consider how we can continuously improve upon the ATTA technique in the future to increase efficiency and remove the cross-sample contamination effect. Those two issues alone control our ability to reduce sample size, increase sample throughput, and increase both statistically-limited and systematically-limited measurement precision.

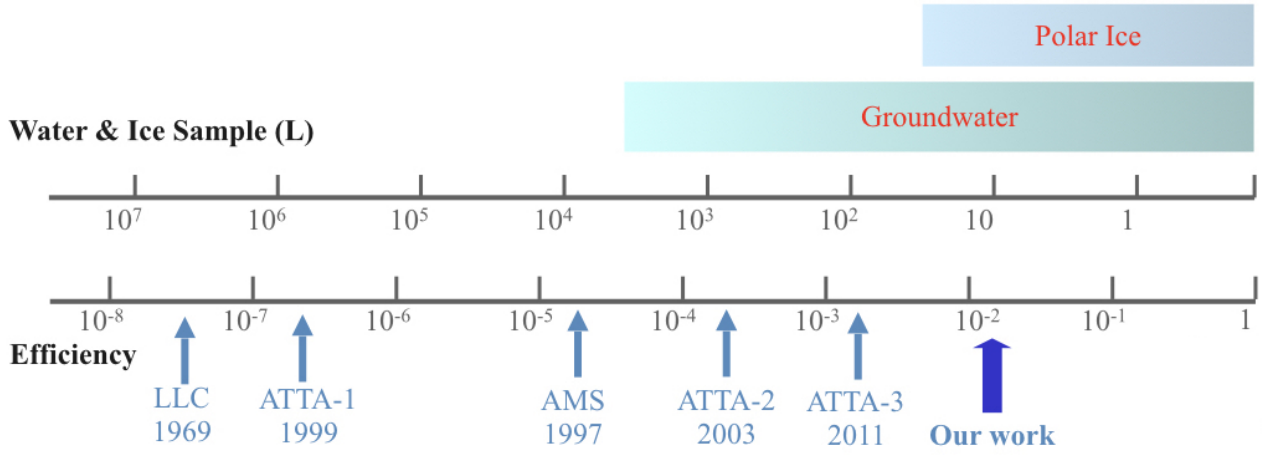

Figure 7.1: ATTA atom counting efficiency and sample size requirements in liters of water or ice. We show the improvements in the technique over the years and in comparison with other methods. We display the ranges over which regular groundwater and ice-core dating are available using bands above the scales.

We present ATTA-3's current ^{81}Kr atom counting efficiency against former versions and iterations of ATTA, as well as the efficiency of other methods in Figure 7.1. We have certainly come a long way through ATTA and have improved a great deal up to and including this

work. However, how do we move forward for the next generation of ATTA? What can we do to improve efficiency and remove the cross-sample contamination effect?

The obvious solution is an improvement of the metastable krypton source. Most of the improvements that we have used to reach the current efficiency have been updates to atomic optics technology to better our slowing, cooling, and trapping. However, the fraction of atoms available to trap is set by the number of metastable atoms produced at the source, the efficiency of which is 10^{-4} - 10^{-3} with the current source. In addition, the implantation from ionization within the plasma discharge is what causes the cross-sample contamination effect. Ideally then we wish to somehow increase metastable production efficiency, and simultaneously avoid the exposure of our sample to a plasma discharge. Such an approach, specifically using the optical excitation of metastable krypton, has been both developed (81) and demonstrated (82), as we will detail in Section 7.1. We further investigated this approach and describe the findings of our investigation in Section 7.1.2.

Afterward, we also lay out other non-source-related improvements that we envision for future systems in Section 7.2.

7.1 Optical sources

Two optical excitation schemes have been proposed for forming metastable krypton as shown in Figure 7.2. Both require three photons due to selection rules. The first, mentioned in Figure 2.5, and suggested in (81), requires a 124 nm photon and then a 819 nm photon. From this $5p[3/2]_2$ excited state, the atom will decay, emitting a 760 nm photon, to the metastable state. Alternatively, a pair of 215 nm photons can be used to excite a two-photon transition to $5p[3/2]_2$. Again, from that state, the atom will subsequently emit a 760 nm photon and reach the metastable state.

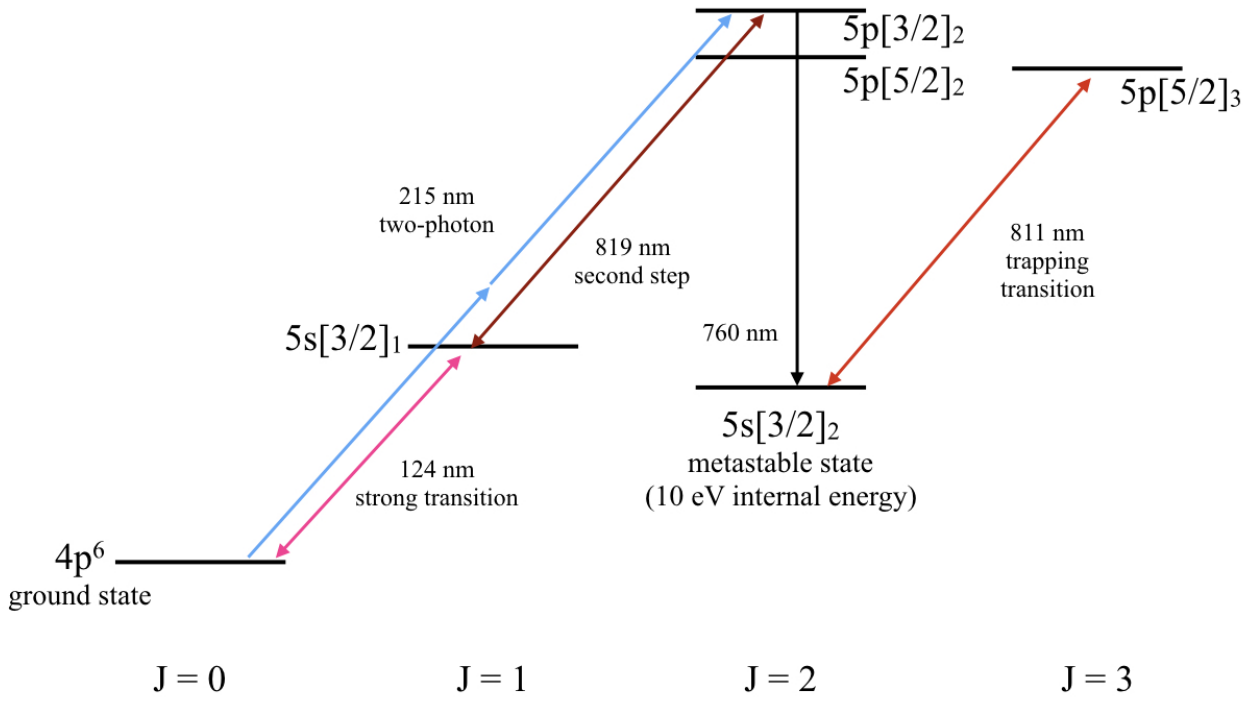

Figure 7.2: A relevant subsection of the electronic level diagram for krypton atoms. Two optical excitation schemes are shown. The first uses a 124 nm transition, an 819 nm transition, and a 760 nm photon decay (shown also in Figure 2.5). The other uses a 215 nm two-photon transition and a 760 nm photon decay.

7.1.1 Laser excitation

The most natural thought one might have to conduct either of these schemes is the implementation of a laser, or set of lasers. As mentioned in Section 2.2.2, doing this for the 124 nm transition is difficult. Laser sources do exist at this wavelength and may at some point be made viable, however, the current state-of-the-art lasers are not practical to achieve useful metastable production efficiency using this scheme.

The alternative path is to use a 215 nm two-photon transition, shown in Figure 7.2, to excite the atom to the same state that the 124 nm and 819 nm photons would ($5p[3/2]_2$). The advantage is that 215 nm laser light is much more readily available than 124 nm. The drawback is that because we are now using a two-photon transition, we require a lot more power. To achieve such power, we would need to use a build-up cavity at the krypton gas source or a high-powered pulsed laser. In both cases, reaching enough power for higher metastable production efficiencies is still difficult and, to date, undemonstrated. In addition, there may be unwanted side-effects using this scheme, such as substantial ionization of our krypton atoms. Given the power needed to excite the two-photon transition at a reasonable rate, it would be very easy for an excited atom to pick up another 215 nm photon and become ionized.[1] This will not only reduce efficiency, but could produce systemic effects and losses we were hoping to avoid if the ionization occurs to a large enough fraction of the atoms.

7.1.2 Krypton discharge lamp

An alternative method, however, is to return to the scheme requiring 124 nm light, but produce that light from a krypton discharge lamp (81). This method requires sparking a plasma discharge in a glass cell of krypton gas and appending that cell to the ATTA vacuum system which contains the sample krypton gas that we wish to transfer to the metastable state. The krypton gas in the cell, when excited by the plasma, produces 124 nm light once it

1. The ionization energy of krypton atom is 14 eV, and a 215 nm photon is 5.8 eV in energy.

subsequently decays from the first excited state to the ground state. Ideally, the cell, i.e. our lamp, is appended to the ATTA vacuum system in such a way that the "lamp" krypton under discharge and the "sample" krypton in ATTA are kept separated from one another, but the UV photons emitted from the "lamp" krypton reach the "sample" krypton for excitation. This requires that the lamp and ATTA vacuum systems are separated by some solid material that is transmissive in the 124 nm range. Options with high transmissivity at 124 nm are fairly limited. We use a magnesium fluoride (MgF_2) window (83).

This discharge lamp idea was originally presented in (81), where it was shown that $\sim$10% of the 124 nm photon flux is converted ultimately to metastable flux, using a Ti:Sapphire laser to produce 819 nm with sufficient power to saturate the second stage of the transition. With further development, a beam of metastable krypton atoms was produced with metastable excitation efficiencies equivalent to the current ATTA source, but by using five times higher gas flow (82). Even with this higher gas flow requirement, the benefits of avoiding the cross-sample contamination alone make the lamp an extremely promising option. Unfortunately, the lamp presented in (82) had a limited lifetime of just a few hours, barely enough for a single ATTA run (84). The cause of this lifetime is sputtering of the local material in or near the lamp by the plasma discharge, which coats the MgF_2 window, reducing transmissivity until the lamp is unusable. After this point the window needs to be cleaned or replaced.

We thus decided to conduct a brief exploration into this lifetime problem. First, we designed a slightly different lamp from (82) in two respects. (1) Rather than have a closed glass cell filled with krypton, we developed a "flowing" lamp where the krypton gas is constantly passing through the system and carried away. Operated in the >50 mTorr range, this produces viscous flow (rather than molecular flow), capable of potentially carrying sputtered materials away from the window (85) and reducing the coating rate. (2) We developed a contact vacuum seal between the lamp and MgF_2 window which adjoins the ATTA vacuum system. This contact seal is created by an o-ring which presses down on the *outside* of the lamp. Such a seal removes all material besides the lamp itself from the plasma region,

reducing the types of material which can sputter onto the window. A mechanical drawing of the lamp and an image of it in use, appended to our source chamber with a contact seal, are shown in Figure 7.3 (a) and (b), respectively. In Figure 7.3 (b) a microwave cavity, which operates at 2.4 GHz, is used to stimulate the discharge. Our system is designed to use either this microwave-based method or an external copper can and coil like that used on the current ATTA source to instead produced an RF-based discharge at 70 - 80 MHz.

Opposite the lamp, attached to the other side of the source chamber, we placed a UV spectrometer (also under vacuum to prevent UV losses to the air). The spectrometer has a resolution of 0.1 nm and was set to 124.6 nm to measure signal from the desired UV photons in our lamp. We varied pressure, input power, gas admixtures of krypton with oxygen or other noble gases, and type of discharge (RF and microwave), but the lifetime problem persisted, although with a slightly higher lifetime (15 hours versus the 5 hours from (82)), as can be seen in Figure 7.4.

To continue our investigation, we conducted energy-dispersive x-ray spectroscopy (EDX) of our used (and thus coated) MgF_2 window on a scanning electron microscope (SEM) at the Center for Nanoscale Materials (CNM) at ANL. This procedure fires high energy (7 - 30 keV) electrons at the surface of a material, which knock out an inner shell electron, causing higher level electrons to decay to fill the inner-shell vacancy. These decays produce characteristic x-rays for each element, given the element's unique atomic structure (86). Thus, EDX allows us to determine the elemental composition on the surface of our window. The results of one such scan on our MgF_2 window are shown in Figure 7.5. There are three x-rays peaks which are marked with the elements they represent. Thus we detect the expected presence of magnesium (Mg) and fluoride (F), but also some very light element. We determine this other element to be boron (B), etched from the borosilicate pyrex glass used to make our lamp. Note, however, we do not see any characteristic peaks for silicon (Si). As such, we have determined from our investigation that switching to a purely quartz (SiO_2) lamp (which is more difficult to manufacture than a pyrex lamp from a glass blowing standpoint, but still

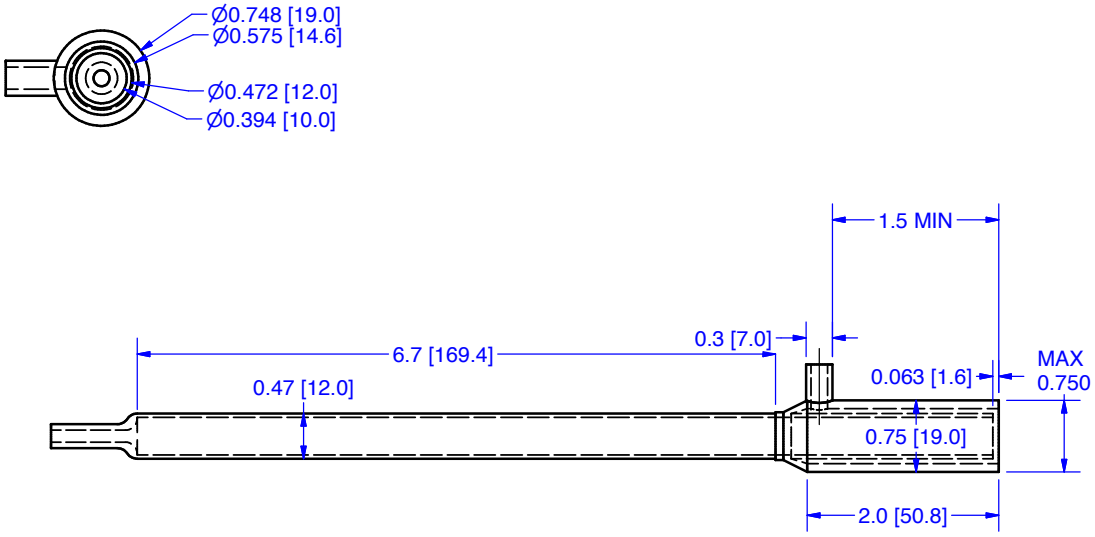

(a)

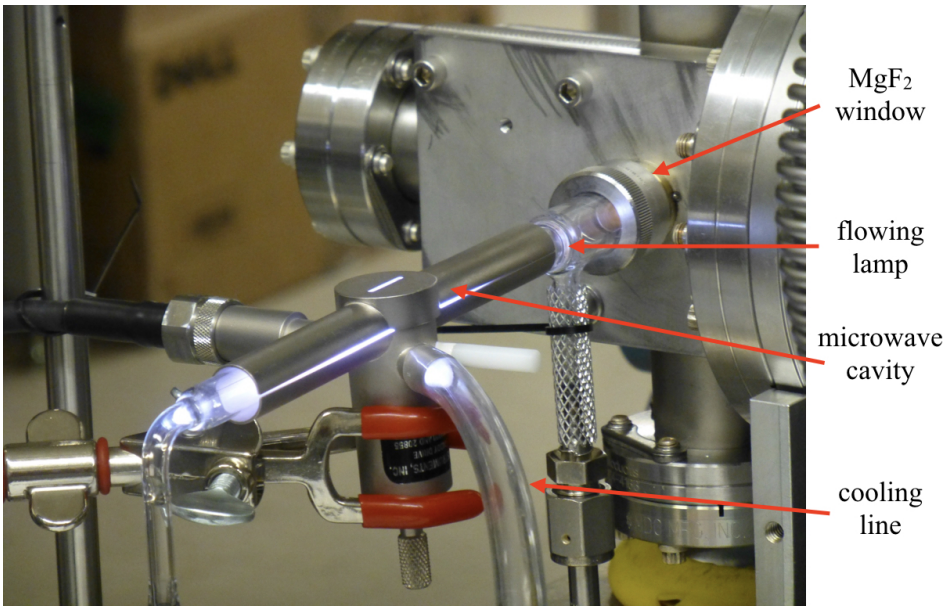

(b)

Figure 7.3: (a) Mechanical drawing of the flowing lamp. Gas travels into the arm perpendicular to the body, and along an outer sheath to the wide end of the lamp, where the window is placed. Upon reaching the window, the gas passes through a 1/16" gap into the main tube and flows away from the window toward and eventually out of the narrow end of the main tube. Drawing courtesy of Kevin Bailey. (b) Image of the flowing lamp with an active discharge provided by a microwave cavity. The lamp is appended to a rectangular plate onto which a MgF_2 window has been sealed using an indium seal on the opposite side of the plate from the lamp. The lamp is sealed against the window by contact using external pressure only. The light passes into a source chamber like the one shown in Figure 7.6.

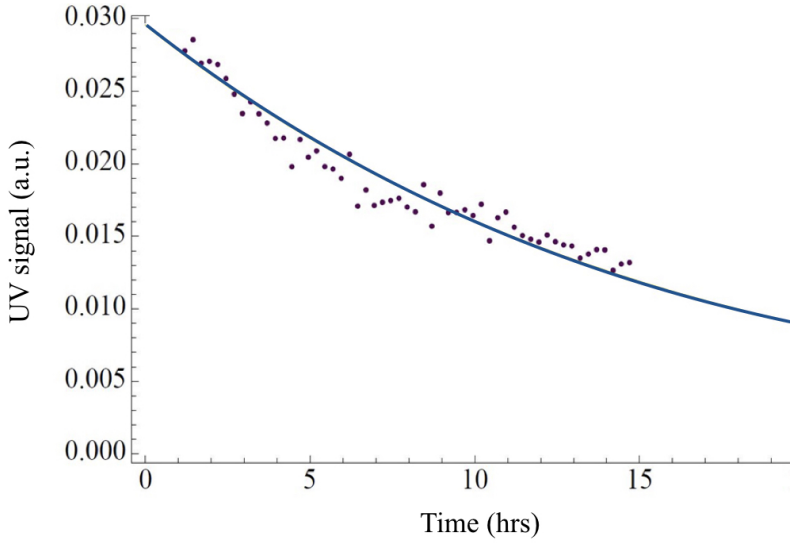

Figure 7.4: Fluorescence lifetime measurement for flowing lamp. Signal on the UV spectrometer in arbitrary units is plotted against the length of time the discharge is active, in hours. This is one of the longer lifetimes from the many trials given the varied properties described in the text. The lifetime is approximately 15 hours as represented by the fit to an exponential decay function shown as the dark blue line.

doable) may mitigate the lifetime problem as efforts to develop this source continue.

Beyond the development of a quartz lamp, our investigation has led to two other recommendations for building up a discharge lamp source. First, if the quartz lamp does not completely remove the lifetime issue (as silicon may perhaps simply build up on a longer timescale), we suggest intermittently injecting sulfur hexafluoride (SF_6) into the lamp. It is an inert gas that, when exposed to plasma in the presence of silicon, can etch it away with high efficiency, thus refreshing the window without breaking vacuum (87). Second, we have redesigned the geometry of the internal source chamber, where sample krypton would be excited, to improve excitation efficiency from previous designs. The new geometry is shown in Figure 7.6. This new geometry extends and places off-center the tube where the sample krypton atoms flow through before hitting a capillary plate, which is meant to enhance the collimation of the krypton gas cone. This shift places the most dense region of forward-directed krypton atoms (just outside the capillary plate) immediately in front of the lamp, which has been inserted more deeply into the chamber. This geometry assures excitation

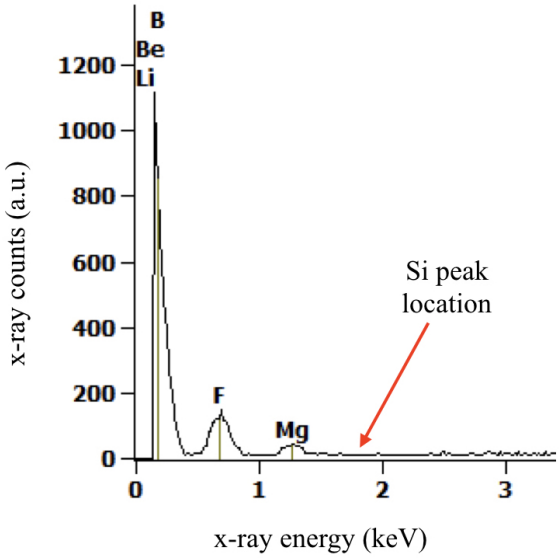

Figure 7.5: Surface composition of a discharge coated MgF_2 window determined by EDX. Counts on photodetectors are plotted against x-ray energy. The x-rays detected are characteristic of the elements magnesium (Mg) and fluoride (F), as expected, but also some very light element. We determine this other element to be boron (B), etched from the borosilicate pyrex glass used to make our lamp. A peak for silicon (Si) is noticeably absent. The full scan continued up to 10 keV, but showed no further signals beyond the 3 keV mark.

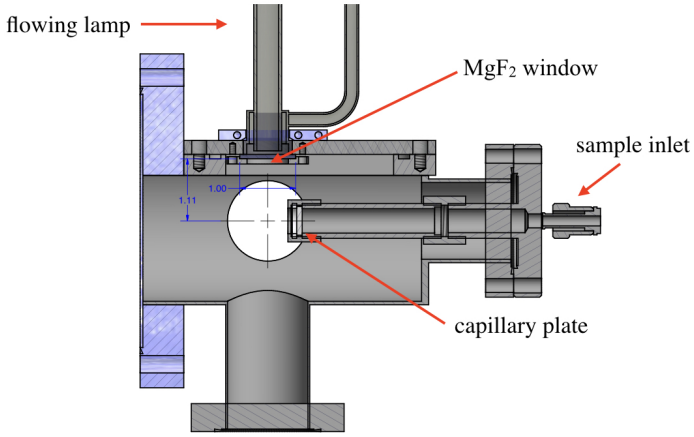

Figure 7.6: Drawing of the new source chamber for the discharge lamp source. The sample krypton travels along the tube from the right hand side of the drawing before reaching a capillary plate, which diverts more of the krypton into the forward direction as it enters the source chamber. Just outside the capillary plate, the lamp (top) is set against the MgF_2 window to excite the sample krypton with 124 nm light. 819 nm light can be inserted into or out of the page through window ports on either side of the vacuum chamber. Drawing courtesy of Kevin Bailey.

occurs in the densest region of forward-directed krypton, which is the krypton most easily cooled further down a potential ATTA beamline.

Ideally these recommendations will make optical excitation through a krypton discharge lamp ready for application to ATTA in the near-future.

7.2 Other upgrades and future issues

Beyond the source improvement, there are a series of smaller improvements that have been identified that can enhance the efficiency of the current ATTA-3 design at ANL.

- Replace the Zeeman slower tube: Due to other improvements in ℓN_2 cooling of the discharge tube, the current Zeeman slower tube is longer than necessary to accommodate a Zeeman slower which is necessary for optimal longitudinal cooling. Reducing the length of the tube could provide an increase in counting efficiency by a factor of 1.2 - 1.5.

- Replace the ℓN_2 dewar: A larger dewar will make the cooling more stable and reliable throughout measurements.

- Replace VCOs with stable RF sources to remove dead time: The nominally 5-minute cycle of switching between ^{81}Kr, ^{85}Kr, and ^{83}Kr often takes closer to 7 - 8 minutes. This extension is due to dead time during which the control computer needs to check and adjust the frequencies for the various VCOs. By using stable, synthesized, RF sources we can remove this process, reducing the cycle to only 5 - 6 minutes of actual time per 5 minutes of trapping time.

- 819 nm metastable booster: We have conducted a proof-of-principle demonstration of increased metastable efficiency by overlapping an 819 nm laser beam with the Zeeman slower laser beam. This laser pumps atoms which the plasma has put into the first

excited state to the metastable state following the path shown in Figure 7.2. Even in a first unoptimized initial trial, we saw a 20% boost in ^{83}Kr trapping efficiency.

Beyond efficiency there are several other items of importance. For instance, with increased efficiency, eventually systematic limits will be reached and system stability will thus need to be enhanced. This can be achieved by fiber-coupling optics from the optical table to the beamline table and adding power stabilization stages at each coupling. Also with increased efficiency we must alter our trapping and counting methods somewhat. Regarding single atom trapping, if we trap too many atoms then the higher single atom peaks between, say, 10 and 11 atoms, will be indiscernible from one another. We can increase signal by including a mirror opposite the camera to collect twice the solid angle's worth of photons, but that will only take us so far. If we start trapping twenty or more atoms per trapping cycle, we will need a more major alteration. Similarly, for ^{83}Kr, even a factor of two increase in trapping efficiency will take us out of the usable region of the ion detection method (mentioned in Section 2.2.7; for more details see (39)). Here we can freely reduce the efficiency since the error is not determined by the number of ^{83}Kr trapped atoms, but we will need to find a way to do so in a controlled method that does not produce systematic effects when comparing to the ^{81}Kr and ^{85}Kr loading efficiencies.

7.3 Conclusions

This dissertation has presented several major accomplishments in improving the state of radiokrypton analysis for the scientific community in subfields ranging from hydrology to nuclear science.

^{81}Kr-analysis is now two times faster than the previous state-of-the-art, improved in efficiency, and has had internal and external systematic effects addressed at the 1% level of precision. Such developments have opened the door to increased groundwater dating, new ice-core dating, and high-precision measurements on younger groundwater to assist in

understanding ^{14}C-dating corrections. ^{85}Kr-analysis has improved commensurately, and also with the help of our new rapid-processing method, has seen a further increase in sample throughput. This increase opens up large-scale ^{85}Kr-analysis for the monitoring of nuclear fuel reprocessing and the more resolved tracing of young and shallow groundwater aquifers.

Our continued application work in the meantime has not only produced new scientific understanding in these various subfields but demonstrated the depth and variety of the demand for radiokrypton analysis. As such, it is crucial that further improvements, such as those described in this Chapter–particularly for the source–are made, so that the scientific contributions of ATTA can continue to grow, taking advantage of the still sizable untapped potential of this technique.

APPENDIX A

SETTINGS FOR ATTA-3 INSTRUMENTATION

This Appendix lists the settings used to operate the ATTA-3 system at ANL as of March 2017.

Table A.1 reports the currents used on the lasers throughout the system, described fully throughout Section 2.2.

	Laser/Chip Type	Current (mA)
Master Laser	DL 100 (Toptica)	145
Prime TA	Eagleyard 1000 mW 808 nm TA	2200
TC TA	Eagleyard 2000 mW 808 nm TA	2000
Slower TA	TA 100 (Toptica)	155
MOT TA	Eagleyard 2000 mW 808 nm TA	2750
Quench Laser	DL 100 (ECDL)	203

Table A.1: Seed laser and tapered amplifier current settings. Reported currents are in mA and are absolute values. Outputs as a result of these currents appear in Figure 2.4 and are discussed throughout Section 2.2. Current settings for seed lasers are varied by a few milliamps during locking procedures.

Table A.2 includes the frequencies applied for trapping and repumping for ^{81}Kr, ^{83}Kr, and ^{85}Kr. They are listed by what frequencies are actually applied to the EOMs and AOMs shown in the optical setup from Figure 2.4, as opposed to simply listing the transition frequencies for the isotopes. Of course, following the stages in Figure 2.4 and using the numbers in Table A.2, the transition frequencies can be easily determined as well.

	DP AOM	TC AOM	MOT AOM	TC EOM 1st SB	TC EOM 2nd SB	TC EOM 3rd SB	MOT EOM 1st SB	MOT EOM 2nd SB
^{81}Kr	276	100.3	94.5	963	1454	1662	955.5	1446.5
^{83}Kr	341.2	100.3	94.5	870	1489	1915	862.5	1481.5
^{85}Kr	385	100.3	94.5	947	1558	1930	939.5	1550.5

Table A.2: Frequency offsets on ATTA-3 for trapping and repumping transitions in MHz. Isotopes are listed against the optical elements to which the frequencies are applied. Elements shown in Figure 2.4. EOM frequencies are stabilized to 0.5 MHz before they are relocked. DPAOM and AOM frequencies are stabilized to 0.1 MHz.

Table A.3 reports the currents used on each section of copper coils that provide for the magnetic fields.

Coil Section	Current (A)
2D MOT coils	0.950
Slower, tapered down section (1st)	0.791
Slower, uniform section (2nd)	1.291
Slower, tapered up section (3rd)	1.130
3D MOT, horizontal and vertical trim	0.700
3D MOT, optical axis trim	0.260
3D MOT main coil (high gradient)	6
3D MOT main coil (low gradient)	5

Table A.3: Currents to coils providing magnetic fields. Currents are reported in amps and kept stable to the mA level by the power supplies for all coils except the 3D MOT main coil (due to flipping between the two gradients for single atom trapping).

Finally, although the high voltages on the electrodes must be altered based on the alignment (as noted in Section 2.2.7), the current settings as of March 2017 for reference are (based on markings on the MOT chamber):

- Far North: 3500 V
- Far South: 2800 V
- Near South: 1700 V
- Reflector: Grounded

APPENDIX B

DATA ANALYSIS PROGRAMS

This Appendix includes the Mathematica notebooks used for data analysis of ATTA-3 measurements, which is generally discussed in Sections 2.3, 2.4, and 2.5. The programs that appear are (in order)

- outgassing calculator (6 pages)
- sample gas diagnostics (7 pages)
- single atom optimization (5 pages)
- ATTA main analysis (17 pages)

There are notebook titles in the header of each page to determine the programs from one another.

The "outgassing calculator" is used to analyze the RGA scans taken during the outgassing test, ultimately producing a rate for krypton outgassing into the system (separate fits must be made for the weak mode and strong mode rates).

These results are directly compared to the average krypton pressure as measured by the RGA during the sample run to get the correct contamination fraction. The average krypton pressure is determined at the end of the "sample gas diagnostics" program. This program also measures the gas composition ratios of other gases with respect to krypton according to the RGA.

The "single atom optimization" program is to ensure that we have collected the maximum amount of photons from the ^{81}Kr or ^{85}Kr atoms in our trap. The program shifts the region of interest coordinates to maximize the signal. Furthermore, the end of the program shows a histogram of these optimized coordinates. If these histogram distributions are skewed it is a marker that the single atom signal is asymmetric and the MOT requires realignment.

The final "ATTA main analysis" program is used to produce the graphs and results seen in Section 2.4 and follows the description in that section. Note, that the file initially plotted typically includes both a sample measurement and its reference measurement. We then select out the data from one or the other during the signal cutting process for removing bad data. The example shown selects the sample measurement. The end of this program also contains a small section of code to test whether or not the distribution of atoms trapped is governed by a Poisson distribution.

In[221]:=
```
Clear["Global`*"]
```

```
(*Maybe add an inputs section up here at some point*)
(*For shortened scans non-integrated plots are disabled*)
```

In[222]:=
```
(*SCAN SPECIFICATIONS*)
<< PlotLegends`;
SetOptions[Plot, BaseStyle → {FontFamily → "Times", FontSize → 18}];
SetOptions[ListPlot, BaseStyle → {FontFamily → "Times", FontSize → 18}];
SetOptions[ListLogPlot, BaseStyle → {FontFamily → "Times", FontSize → 18}];
SetOptions[ListLogLogPlot, BaseStyle → {FontFamily → "Times", FontSize → 18}];
(*This program reads RGA Analog Scans. Write in the
 directory name to call the file. The file with then be opened for
 reading. Usually replace "System" with "Folder Name" of experiment.*)
outgasFile =
  "/Users/jczappala/Desktop/161020/outgas test/rga2_Oct_20_2016_09-38-44_AM.ana";
outgas = OpenRead[outgasFile, BinaryFormat → True];
(*RGA File Parameters*)
FileHead = 52;
ScanHead = 50;
(*The following parameters are required
 from the scan to approatiately parce the file.*)
StartMass = 1;
StopMass = 90;
MassStep = 0.1;
ScanSize = Round[(StopMass - StartMass)/MassStep + 1];
ScanNumTest = (FileByteCount[outgasFile] - FileHead) / (ScanSize * 4 + ScanHead);
(*n.b. the head is removed via 26*2,
the rest is parced into scans, each which contain 4 bits
 for each sample point as well as 50 bits of timing info*)
δT = 37.0 / 3600;(*Single scan time in hours, typically 37.0/3600 for full scan*)
```

```
(*GENERAL PLOTS*)
```

```
(*Plot some run details*)
MassAxis = Table[StartMass + (i - 1) * MassStep, {i, 1, ScanSize}];
SetStreamPosition[outgas, FileHead];
StartTime = ReadList[outgas, Word, 4];
i = ScanNumTest;
```

```
SetStreamPosition[outgas, FileHead + (ScanSize * 4) * (i - 1) + ScanHead * (i - 1)];
StopTime = ReadList[outgas, Word, 4];
Print["Total Scan Number = ", ScanNumTest]
Print["Start Time", StartTime]
Print["Stop Time", StopTime]

(*The following bits allow us to probe our gases of interest*)
Gases = {"H2", "CH4", "H2O", "N2", "O2", "Ar", "CO2", "Xe(Dbl)", "Kr"};

(*We now want to find the peaks for the gases of interest,
scanning 0.3 in either direction of the expected peak locations*)
MassList = {2.0, 16.0, 18.0, 28.0, 32.0, 40.0, 44.0, 65.4, 84.0};
r = ScanNumTest - 10;
SetStreamPosition[outgas, FileHead + (ScanSize * 4) * (r - 1) + ScanHead * (r - 1)];
StopTime = ReadList[outgas, Word, 4];
SetStreamPosition[outgas,
  FileHead + (ScanSize * 4) * (r - 1) + ScanHead * (r - 1) + ScanHead];
RandomScan = BinaryReadList[outgas, "Real32", ScanSize];
RandomPlot = ListLogPlot[Thread[{MassAxis, RandomScan}],
  Joined → True, PlotRange → {{0, 90}, {10^-16, 10^-6}},
  AspectRatio → 1 / 4, ImageSize → 800, PlotStyle → Blue]
MassListLength = Length[MassList];
For[j = 1, j < MassListLength + 1, j++,
  m = Round[(MassList[[j]] - 1)/MassStep + 1];
  temp = 0;
  For[i = m - 4, i < m + 5, i++,
   If[RandomScan[[i]] > temp, PeakMass = (i - 1) * MassStep + 1;
     temp = RandomScan[[i]]];
  ];
  MassList[[j]] = PeakMass;
 ];

(*And we write them down as output*)

TableForm[{Gases, MassList}, TableHeadings → {{"Gas Name", "Peak Mass"}, None}]
(*Now we can analyze these other gases. Recall,
the readings start at 1.0, not 0.0!*)
mList = Round[(MassList - 1)/MassStep + 1];

(*To start, we generate a list of lists containing the pressure
```

```
 values for each gas. The outermost call is the gas of interest*)

PList = Table[Table[0, {i, 1, ScanNumTest}, {j, 1, 2}], {k, MassListLength}];
For[i = 1, i < ScanNumTest + 1, i++,
  SetStreamPosition[outgas,
   FileHead + (ScanSize * 4) * (i - 1) + ScanHead * (i - 1) + ScanHead];
  iScan = BinaryReadList[outgas, "Real32", ScanSize];
  For[j = 1, j < MassListLength + 1, j++,
   PList[[j]][[i, 1]] = δT * i;
   PList[[j]][[i, 2]] = iScan[[mList[[j]]]]
  ]
 ];
(*And now we plot our gases all together*)
ColorList = {Blue, Green, Darker[Yellow],
   Brown, Orange, Darker[Green], Red, Magenta, Darker[Red]};
ThickList = Table[Thick, {i, Length[ColorList]}];
StyleList = Thread[{ColorList, ThickList}];
FullGasPlot = ListLogPlot[{PList[[1]], PList[[2]], PList[[3]],
    PList[[4]], PList[[5]], PList[[6]], PList[[7]], PList[[8]], PList[[9]]},
   Joined → True, PlotRange → {10^-16, 10^-5}, AspectRatio → 1 / 3,
   ImageSize → 850, Frame → True, GridLines → Automatic,
   FrameLabel → {"Time (hr)", "Pressure (Torr)"}, PlotStyle → StyleList,
   PlotLegend → Gases, LegendPosition → {0.85, -0.23}, LegendTextSpace → 2,
   LegendSize → 0.53, ShadowOffset → 0.0, LabelStyle → Directive[Black, 15]];
Show[FullGasPlot]
```

General: PlotLegends` is now obsolete. The legacy version being loaded may conflict with current functionality. See the Compatibility Guide for updating information.

```
Total Scan Number = 41

Start Time{Oct, 20,, 2016, 09:39:21}

Stop Time{Oct, 20,, 2016, 10:04:02}
```

Out[253]=

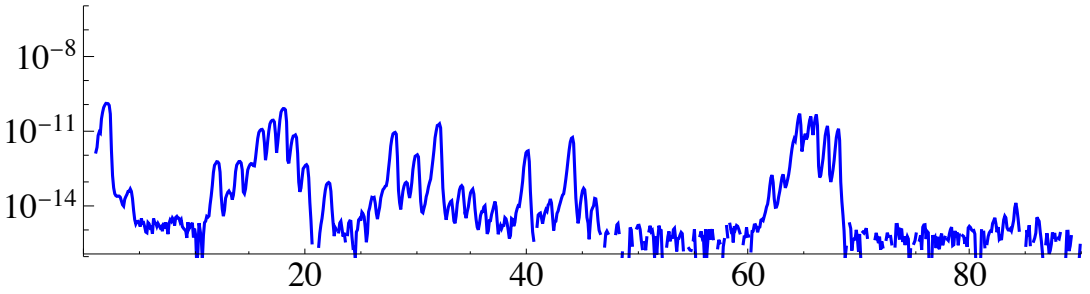

Out[256]//TableForm=

Gas Name	H2	CH4	H2O	N2	O2	Ar	CO2	Xe(Dbl)	Kr
Peak Mass	1.9	16.	17.9	28.	32.	40.	44.	65.5	84.

Out[264]=

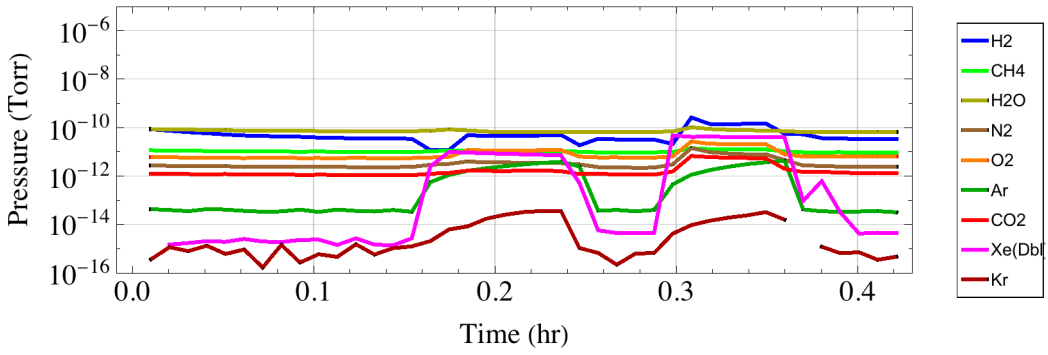

In[288]:=

```
(*Outgassing Plot*)

IntNum = 9;
(*and pick some times*)
StartTime = 0;
EndTime = ScanNumTest * δT;(**)
(*Then we'll collect the surrounding peaks based on a chosen center and width*)
c = 83.9;
w = 0.5;
mStart = Round[ ((c - w) - StartMass) / MassStep + 1];
mEnd = Round[ ((c + w) - StartMass) / MassStep + 1];
IntGas = Table[0, {k, ScanNumTest}, {j, 2}];
(*Insert data with background subtraction, comment*)
Bg = 89.0;
mBg = Round[ (Bg - StartMass) / MassStep + 1];
mBgS = Round[ ((Bg - w) - StartMass) / MassStep + 1];
mBgE = Round[ ((Bg + w) - StartMass) / MassStep + 1];
For[i = 1, i < ScanNumTest + 1, i++,
  IntGas[[i, 1]] = δT * i;
  SetStreamPosition[outgas,
   FileHead + (ScanSize * 4) * (i - 1) + ScanHead * (i - 1) + ScanHead];
  iScan = BinaryReadList[outgas, "Real32", ScanSize];
  IntGas[[i, 2]] =
   Total[Take[iScan, {mStart, mEnd}]] - Total[Take[iScan, {mBgS, mBgE}]];
 ];
(*and the rest is magic*)
StartCount = 1;
```

```
EndCount = ScanNumTest;
For[i = 1, i < ScanNumTest + 1, i++,
  If[IntGas[[i, 1]] < StartTime, StartCount = i + 1];
  If[IntGas[[i, 1]] < EndTime, EndCount = i];
 ];
Data = Table[IntGas[[i, j]], {i, StartCount, EndCount}, {j, 1, 2}];
PMin = Min[Table[Data[[i, 2]], {i, 1, EndCount - StartCount + 1}]];
PMax = Max[Table[Data[[i, 2]], {i, 1, EndCount - StartCount + 1}]];
IntPlot =
  ListPlot[{Data}, PlotRange → {PMin, PMax}, AspectRatio → 1 / 3, ImageSize → 850,
   Frame → True, Joined → True, GridLines → Automatic, PlotStyle → {Darker[Red]},
   FrameLabel → {"Time (hr)", Gases[[IntNum]] "Integrated Pressure in Torr for" }];

(*Fit for the mean pressure*)
FitOn = 1;
If[FitOn == 1,
 start = 0.16;
 end = 0.24;
 StartCount = 1;
 EndCount = ScanNumTest;
 For[i = 1, i < ScanNumTest + 1, i++,
  If[IntGas[[i, 1]] < start, StartCount = i + 1];
  If[IntGas[[i, 1]] < end, EndCount = i];
 ];
 runData = Table[IntGas[[i, j]], {i, StartCount, EndCount}, {j, 1, 2}];
 MyFit = FindFit[runData, {a + b * x}, {a, b}, x];
 LinFit[a_, b_, x_] := a + b * x;
 Avg = Mean[runData[[All, 2]]];
 RatePlot =
  Plot[LinFit[a /. MyFit, b /. MyFit, T], {T, start, end}, PlotStyle → {Red, Thick}];
 Print["We are sampling ", Length[runData], " points for this fit."];
 Print["The outgassing rate is  Kr pressure is ", b /. MyFit, " Torr/hr."],
 RatePlot = Plot[0, {i, 0, 0.01}];]
Show[IntPlot, RatePlot]
```

```
We are sampling 8 points for this fit.
The outgassing rate is  Kr pressure is 1.49347 × 10^-12 Torr/hr.
```

Out[310]=

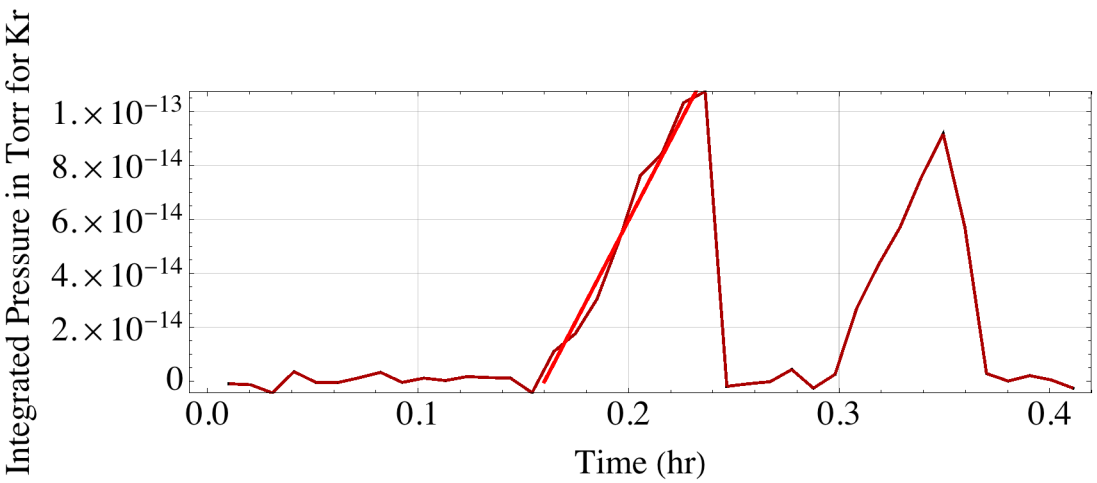
Integrated Pressure in Torr for Kr
1.×10^-13
8.×10^-14
6.×10^-14
4.×10^-14
2.×10^-14
0
0.0
0.1
0.2
0.3
0.4
Time (hr)

In[357]:=
```
Clear["Global`*"]
```

```
(*Maybe add an inputs section up here at some point*)
(*For shortened scans non-integrated plots are disabled*)
```

In[358]:=
```
(*SCAN SPECIFICATIONS*)
<< PlotLegends`;
SetOptions[Plot, BaseStyle → {FontFamily → "Times", FontSize → 18}];
SetOptions[ListPlot, BaseStyle → {FontFamily → "Times", FontSize → 18}];
SetOptions[ListLogPlot, BaseStyle → {FontFamily → "Times", FontSize → 18}];
SetOptions[ListLogLogPlot, BaseStyle → {FontFamily → "Times", FontSize → 18}];
(*This program reads RGA Analog Scans. Write in the
 directory name to call the file. The file with then be opened for
 reading. Usually replace "System" with "Folder Name" of experiment.*)
runFile = "/Users/jczappala/Desktop/161020/RUN1/rga2_Oct_20_2016_10-04-24_AM.ana";
run = OpenRead[runFile, BinaryFormat → True];
(*RGA File Parameters*)
FileHead = 52;
ScanHead = 50;
(*The following parameters are required
 from the scan to approatiately parce the file.*)
StartMass = 1;
StopMass = 90;
MassStep = 0.1;
ScanSize = Round[(StopMass - StartMass)/MassStep + 1];
ScanNumRun = (FileByteCount[runFile] - FileHead) / (ScanSize * 4 + ScanHead);
(*n.b. the head is removed via 26*2,
the rest is parced into scans, each which contain 4 bits
 for each sample point as well as 50 bits of timing info*)
δT = 37.0 / 3600;(*Single scan time in hours, typically 37.0/3600 for full scan*)
```

```
(*GENERAL PLOTS*)
```

```
(*Plot some run details*)
MassAxis = Table[StartMass + (i - 1) * MassStep, {i, 1, ScanSize}];
SetStreamPosition[run, FileHead];
StartTime = ReadList[run, Word, 4];
i = ScanNumRun;
SetStreamPosition[run, FileHead + (ScanSize * 4) * (i - 1) + ScanHead * (i - 1)];
```

```
StopTime = ReadList[run, Word, 4];
Print["Total Scan Number = ", ScanNumRun]
Print["Start Time", StartTime]
Print["Stop Time", StopTime]

(*The following bits allow us to probe our gases of interest*)
Gases = {"H2", "CH4", "H2O", "N2", "O2", "Ar", "CO2", "Xe(Dbl)", "Kr"};

(*We now want to find the peaks for the gases of interest,
scanning 0.3 in either direction of the expected peak locations*)
MassList = {2.0, 16.0, 18.0, 28.0, 32.0, 40.0, 44.0, 65.4, 84.0};
r = ScanNumRun - 1;
SetStreamPosition[run, FileHead + (ScanSize * 4) * (r - 1) + ScanHead * (r - 1)];
StopTime = ReadList[run, Word, 4];
SetStreamPosition[run,
  FileHead + (ScanSize * 4) * (r - 1) + ScanHead * (r - 1) + ScanHead];
RandomScan = BinaryReadList[run, "Real32", ScanSize];
RandomPlot = ListLogPlot[Thread[{MassAxis, RandomScan}],
  Joined → True, PlotRange → {{0, 90}, {10^-16, 10^-6}},
  AspectRatio → 1 / 4, ImageSize → 800, PlotStyle → Blue]
MassListLength = Length[MassList];
For[j = 1, j < MassListLength + 1, j++,
  m = Round[(MassList[[j]] - 1)/MassStep + 1];
  temp = 0;
  For[i = m - 4, i < m + 5, i++,
   If[RandomScan[[i]] > temp, PeakMass = (i - 1) * MassStep + 1;
     temp = RandomScan[[i]]];
  ];
  MassList[[j]] = PeakMass;
 ];

(*And we write them down as output*)

TableForm[{Gases, MassList}, TableHeadings → {{"Gas Name", "Peak Mass"}, None}]
(*Now we can analyze these other gases. Recall,
the readings start at 1.0, not 0.0!*)
mList = Round[(MassList - 1)/MassStep + 1];

(*To start, we generate a list of lists containing the pressure
 values for each gas. The outermost call is the gas of interest*)
```

```
PList = Table[Table[0, {i, 1, ScanNumRun}, {j, 1, 2}], {k, MassListLength}];
For[i = 1, i < ScanNumRun + 1, i++,
  SetStreamPosition[run,
   FileHead + (ScanSize * 4) * (i - 1) + ScanHead * (i - 1) + ScanHead];
  iScan = BinaryReadList[run, "Real32", ScanSize];
  For[j = 1, j < MassListLength + 1, j++,
   PList[[j]][[i, 1]] = δT * i;
   PList[[j]][[i, 2]] = iScan[[mList[[j]]]]
  ]
 ];
(*And now we plot our gases all together*)
ColorList = {Blue, Green, Darker[Yellow],
   Brown, Orange, Darker[Green], Red, Magenta, Darker[Red]};
ThickList = Table[Thick, {i, Length[ColorList]}];
StyleList = Thread[{ColorList, ThickList}];
FullGasPlot = ListLogPlot[{PList[[1]], PList[[2]], PList[[3]],
    PList[[4]], PList[[5]], PList[[6]], PList[[7]], PList[[8]], PList[[9]]},
   Joined → True, PlotRange → {10^-16, 10^-5}, AspectRatio → 1 / 3,
   ImageSize → 850, Frame → True, GridLines → Automatic,
   FrameLabel → {"Time (hr)", "Pressure (Torr)"}, PlotStyle → StyleList,
   PlotLegend → Gases, LegendPosition → {0.85, -0.23}, LegendTextSpace → 2,
   LegendSize → 0.53, ShadowOffset → 0.0, LabelStyle → Directive[Black, 15]];
Show[FullGasPlot]
GasPlot = ListPlot[PList[[9]]];
Show[GasPlot]
```

General: PlotLegends` is now obsolete. The legacy version being loaded may conflict with current functionality. See the Compatibility Guide for updating information.

```
Total Scan Number = 549
Start Time{Oct, 20,, 2016, 10:05:01}
Stop Time{Oct, 20,, 2016, 03:43:14}
```

Out[389]=

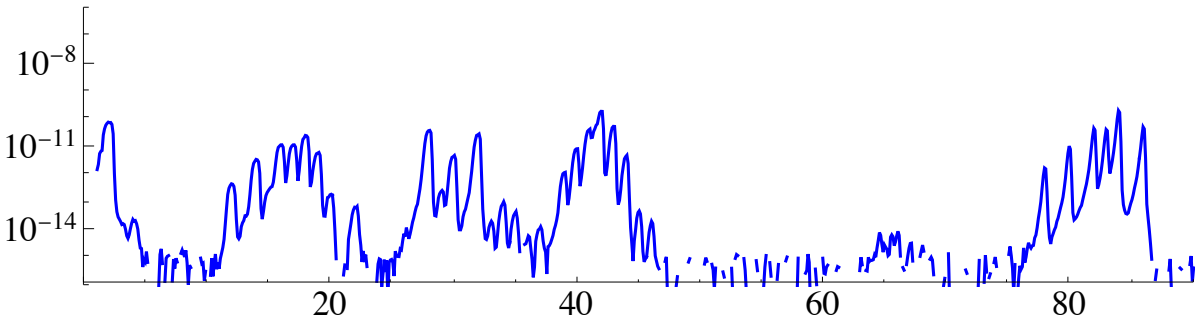

Out[392]//TableForm=

Gas Name	H2	CH4	H2O	N2	O2	Ar	CO2	Xe(Dbl)	Kr
Peak Mass	1.9	16.	17.9	28.	32.	40.	44.	65.5	83.9

Out[400]=

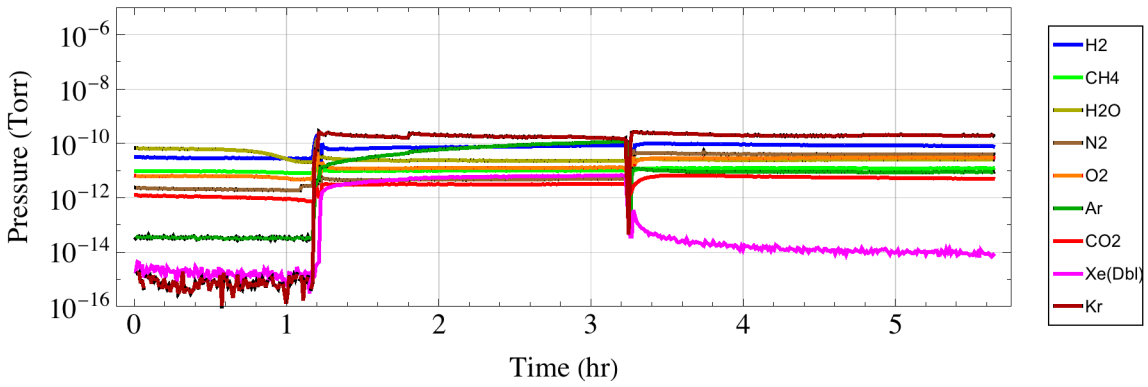

In[403]:=
```
(*Gas Composition Plots*)

(* Check the ratios of the various gases *)
r = i = 0;
scans = Table[0, {j, 5}];
While[r == 0, If[PList[[9, i, 2]] > 0.2 * 10^-12, r = i]; i++]
For[j = 0, j < 5, j++,
 SetStreamPosition[run,
  FileHead + (ScanSize * 4) * (r + j - 1) + ScanHead * (r + j - 1) + ScanHead];
 scans[[j + 1]] = BinaryReadList[run, "Real32", ScanSize];]
ListLogPlot[{Thread[{MassAxis, scans[[1]]}],
  Thread[{MassAxis, scans[[2]]}], Thread[{MassAxis, scans[[3]]}],
  Thread[{MassAxis, scans[[4]]}], Thread[{MassAxis, scans[[5]]}]},
 Joined → True, PlotRange → {{0, 90}, {10^-16, 10^-6}}, AspectRatio → 1 / 4,
 ImageSize → 800, PlotStyle → {Purple, Yellow, Red, Blue, Black}]
```

Out[407]=

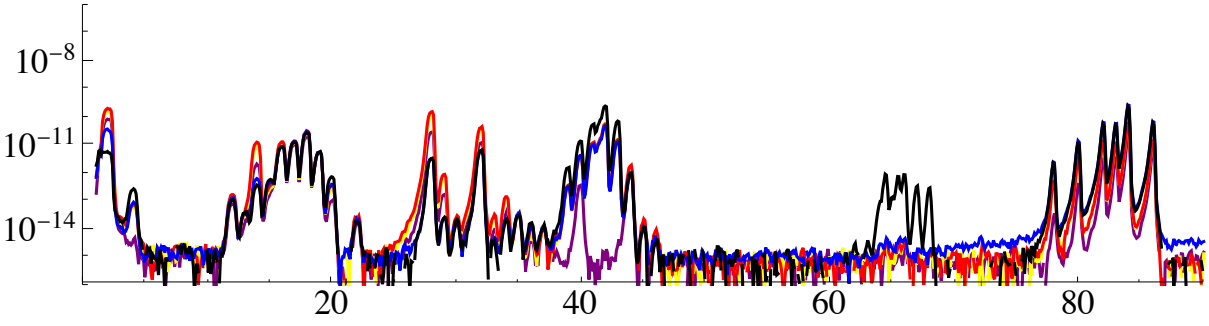

In[408]:=
```
gasScan = 2;
composition = Table[0, {i, 9}];
For[i = 1, i < 10, i++,
 composition[[i]] = PList[[i, r + (gasScan - 1), 2]] / PList[[9, r + (gasScan - 1), 2]]]
TableForm[{Gases, composition},
 TableHeadings → {{"Gas Name", "Ratio to Krypton"}, None}]
SetStreamPosition[run, FileHead + (ScanSize * 4) * (r + gasScan - 2) +
    ScanHead * (r + gasScan - 2) + ScanHead];
scan = BinaryReadList[run, "Real32", ScanSize];
ListLogPlot[Thread[{MassAxis, scan}],
 Joined → True, PlotRange → {{0, 90}, {10^-16, 10^-6}},
 AspectRatio → 1 / 4, ImageSize → 800, PlotStyle → {Green}]
```

Out[411]//TableForm=

Gas Name	H2	CH4	H2O	N2	O2	Ar
Ratio to Krypton	2.70671	0.189947	0.444976	1.70425	0.562413	0.061679

Out[414]=

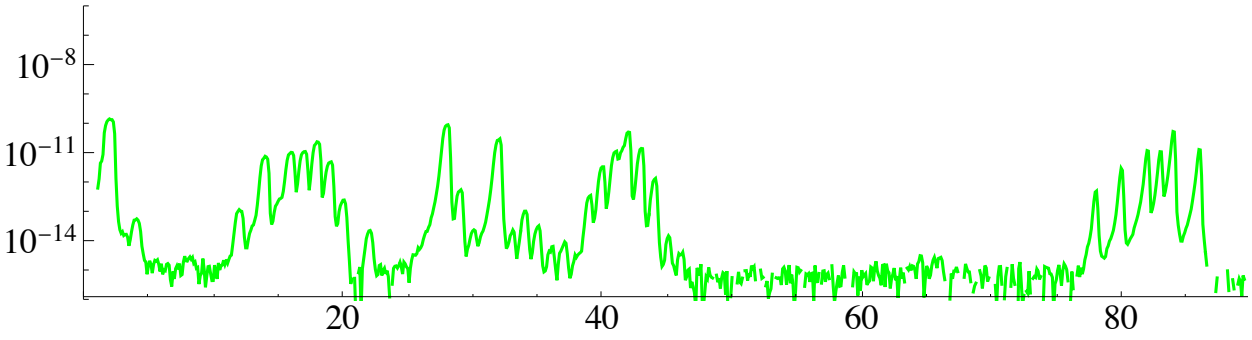

In[438]:=
```
(* Krypton pressure during run and mean total pressure *)

IntNum = 9;
(*and pick some times*)
StartTime = 0;
EndTime = ScanNumRun * δT(*ScanNumRun*δT*);
(*Then we'll collect the surrounding peaks based on a chosen center and width*)
c = 83.9;
w = 0.5;
mStart = Round[ ((c - w) - StartMass) / MassStep + 1];
mEnd = Round[ ((c + w) - StartMass) / MassStep + 1];
IntGas = Table[0, {k, ScanNumRun}, {j, 2}];
(*Insert data with background subtraction, comment*)
Bg = 89.0;
mBg = Round[ (Bg - StartMass) / MassStep + 1];
```

```
mBgS = Round[ ((Bg - w) - StartMass)/MassStep + 1];
mBgE = Round[ ((Bg + w) - StartMass)/MassStep + 1];
For[i = 1, i < ScanNumRun + 1, i++,
  IntGas[[i, 1]] = δT * i;
  SetStreamPosition[run,
   FileHead + (ScanSize * 4) * (i - 1) + ScanHead * (i - 1) + ScanHead];
  iScan = BinaryReadList[run, "Real32", ScanSize];
  IntGas[[i, 2]] =
   Total[Take[iScan, {mStart, mEnd}]] - Total[Take[iScan, {mBgS, mBgE}]];
 ];
(*and the rest is magic*)
StartCount = 1;
EndCount = ScanNumRun;
For[i = 1, i < ScanNumRun + 1, i++,
  If[IntGas[[i, 1]] < StartTime, StartCount = i + 1];
  If[IntGas[[i, 1]] < EndTime, EndCount = i];
 ];
Data = Table[IntGas[[i, j]], {i, StartCount, EndCount}, {j, 1, 2}];
PMin = Min[Table[Data[[i, 2]], {i, 1, EndCount - StartCount + 1}]];
PMax = Max[Table[Data[[i, 2]], {i, 1, EndCount - StartCount + 1}]];
IntPlot =
  ListPlot[{Data}, PlotRange → {PMin, PMax}, AspectRatio → 1 / 3, ImageSize → 850,
   Frame → True, Joined → True, GridLines → Automatic, PlotStyle → {Darker[Red]},
   FrameLabel → {"Time (hr)", Gases[[IntNum]] "Integrated Pressure in Torr for" }];

(*Fit for the mean pressure*)
FitOn = 1;
If[FitOn == 1,
 start = 1.21;
 end = 3.22;
 StartCount = 1;
 EndCount = ScanNumRun;
 For[i = 1, i < ScanNumRun + 1, i++,
  If[IntGas[[i, 1]] < start, StartCount = i + 1];
  If[IntGas[[i, 1]] < end, EndCount = i];
 ];
 runData = Table[IntGas[[i, j]], {i, StartCount, EndCount}, {j, 1, 2}];
 Avg = Mean[runData[[All, 2]]];
 AvgPlot = Plot[Avg, {T, start, end}, PlotStyle → {Black, Thick}];
 Print["The average Kr pressure is ", Mean[runData[[All, 2]]],
  " Torr. The run was ", end - start, " hours long."],
```

```
 AvgPlot = Plot[0, {i, 0, 0.01}];]
Show[IntPlot, AvgPlot]
```

The average Kr pressure is 5.3854×10^{-10} Torr. The run was 2.01 hours long.

Out[460]=

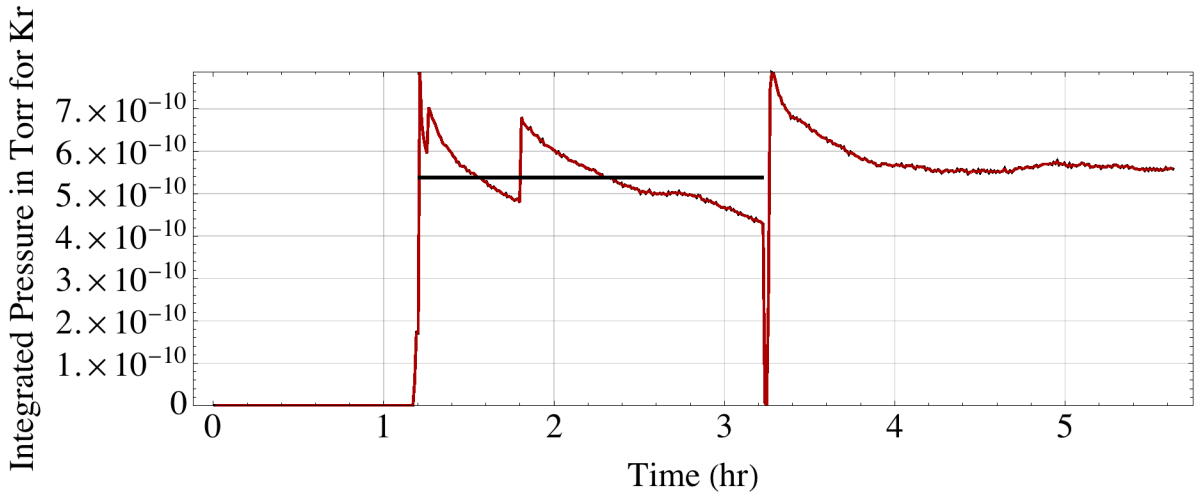

In[461]:=
```
(* ATTA Single Atom Optimization Program, Ver. 1.4 *)
Clear["Global`*"]
```

In[462]:=
```
Needs["ErrorBarPlots`"];
SetOptions[Plot, BaseStyle → {FontFamily → "Times", FontSize → 18}];
SetOptions[ListPlot, BaseStyle → {FontFamily → "Times", FontSize → 18}];
SetOptions[ListLinePlot, BaseStyle → {FontFamily → "Times", FontSize → 18}];
SetOptions[ListLogPlot, BaseStyle → {FontFamily → "Times", FontSize → 18}];
SetOptions[ListLogLogPlot, BaseStyle → {FontFamily → "Times", FontSize → 18}];
SetOptions[Histogram, BaseStyle → {FontFamily → "Times", FontSize → 18}];
(* Import Data: [1] Kr81, [2] Kr85, [3] Kr83 (quench), [4]
 (Do Not Use), [5] (Do Not Use), [6] Kr83 (ion), [7] σ of Kr83
 (ion), [8] Kr83 background, [9]σ of Kr83 background (ion) *)

FileName = "/Users/jczappala/Desktop/161020/RUN1/Modern_0000.pic";
cfg = Import[StringReplace[FileName, "pic" → "cfg"], "Table"];
tag = Import[StringReplace[FileName, "pic" → "tag"], "CSV"];
data = Import[StringReplace[FileName, "pic" → "dat"], "CSV"];
pic = OpenRead[FileName, BinaryFormat → True];

(* Pull all relevant image size settings *)

(* Frames and sizes *)
frames = Length[tag];
tagX = tag[[All, 1]] / tag[[All, 3]];
tagY = tag[[All, 2]] / tag[[All, 3]];

(* ROI info *)
δROIy = Abs[cfg[[9, 3]] - cfg[[11, 3]]];
δROIx = Abs[cfg[[10, 3]] - cfg[[12, 3]]];
ROIyInit = Min[cfg[[9, 3]], cfg[[11, 3]]];
ROIxInit = Min[cfg[[10, 3]], cfg[[12, 3]]];
OptROIxTable = {ROIxInit}
OptROIyTable = {ROIyInit}
ROIClipPrevent[x_] := Which[x < 1, 1, x > 23, 23, x <= 23 && x ≥ 1, x];

(* Data for optimization *)
opt = Table[0, {i, frames}, {j, 9}];
opt = data;
```

Out[481]= {13}

Out[482]= {13}

In[486]:=
```
(* Find a no-atom frame and produce an ROI threshold *)

low = Input["Select threshold for no-atom frame:", 137 000];
blank = 1;
i = 1;
While[blank == 1, If[0 < data[[i, 2]] < low, blank = i]; i++]
x = Take[tagX, blank - 1];
y = Take[tagY, blank - 1];
w = tagX[[blank]];
h = tagY[[blank]];
blank
SetStreamPosition[pic, 4 * Total[x * y]];
bgscan = BinaryReadList[pic, "Integer32", w * h];
bgpicScan = Table[0, {i, h}, {j, w}];
For[i = 1, i < h + 1, i++,
  For[j = 1, j < w + 1, j++,
   bgpicScan[[i, j]] = bgscan[[(i - 1) * w + j]]]];
ArrayPlot[bgpicScan, ColorFunction → "TemperatureMap"]
ListPlot3D[bgpicScan]
```

Out[494]= 251

Out[499]=

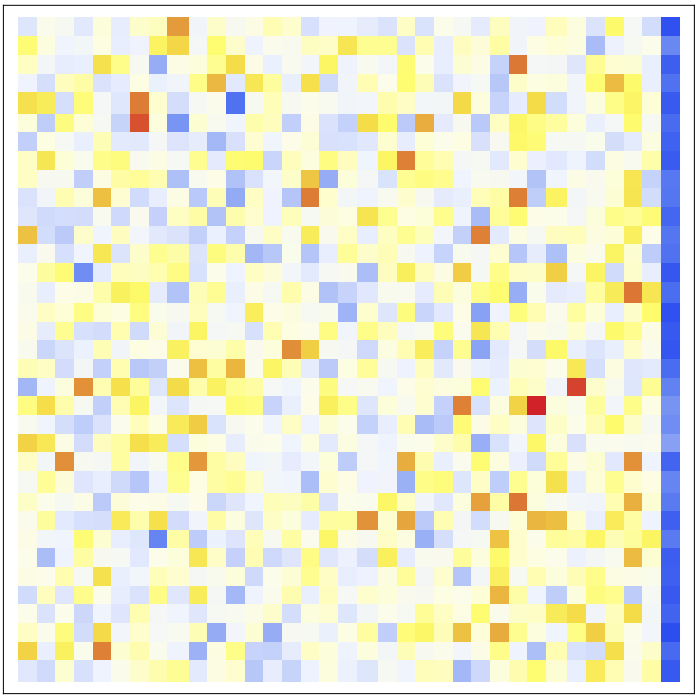

Out[500]=

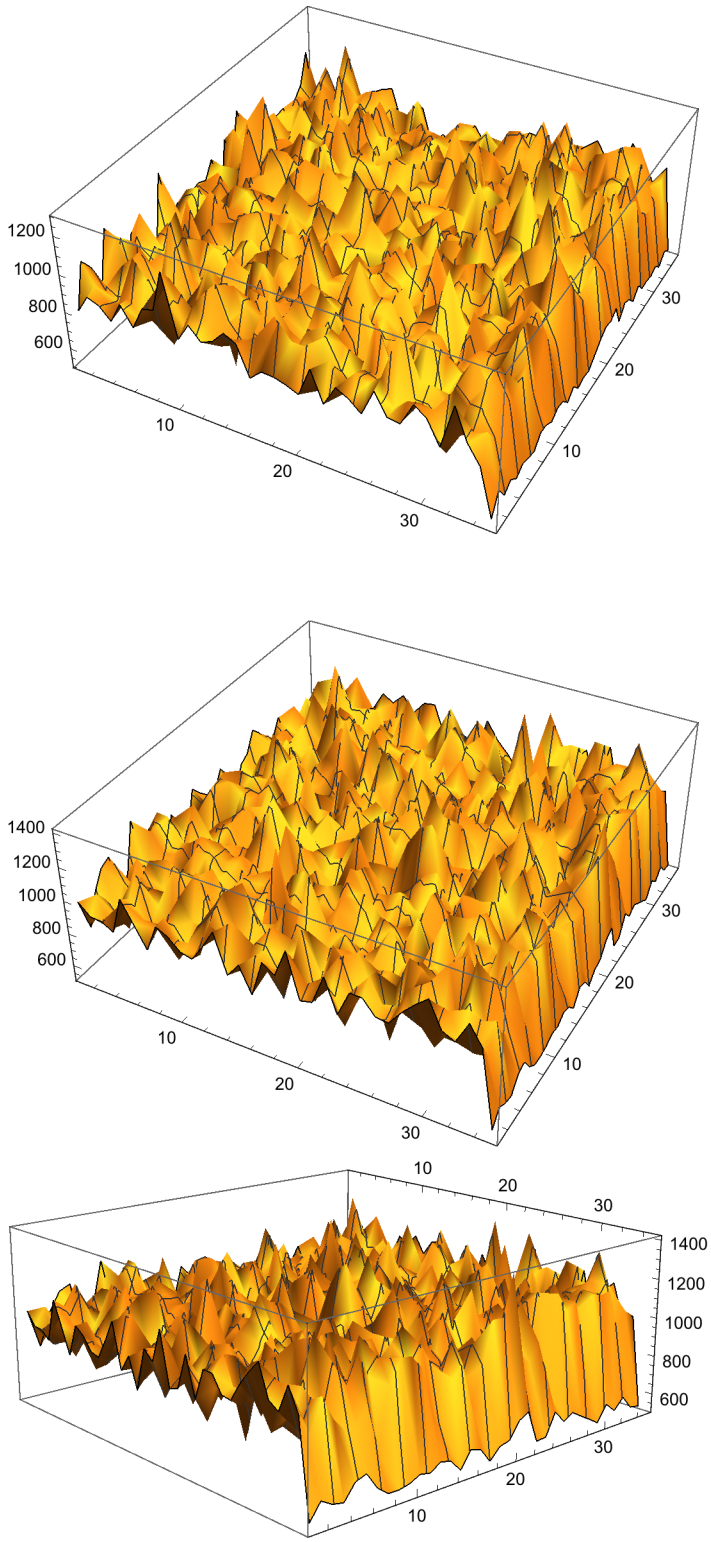

In[501]:=

```
(*picscan = frame1, scan = whole *)

threshold = Max[bgscan] + 100;
newROI = Table[0, {i, δROIx}, {j, δROIy}];
```

```
flag[x_] := If[x > threshold, 1, -1];
For[i = 1, i < frames + 1, i++,
  frame = i;
  If[tag[[frame, 5]] ≠ 2,
   xi = Take[tagX, frame - 1];
   yi = Take[tagY, frame - 1];
   SetStreamPosition[pic, 4 * Total[xi * yi]];
   scan = BinaryReadList[pic, "Integer32", w * h];
   picScan = Table[0, {t, h}, {m, w}];
   For[t = 1, t < h + 1, t++,
    For[m = 1, m < w + 1, m++,
     picScan[[t, m]] = scan[[(t - 1) * w + m]]]];
   PeakPixelList = Position[Map[flag, picScan, {2}], 1];
   PeakPixelListLength = Length[PeakPixelList];
   If[PeakPixelListLength > 1, (* 1 point may be a hot pixel*)
     PeakY = Sum[picScan[[PeakPixelList[[k, 1]], PeakPixelList[[k, 2]]]] *
          PeakPixelList[[k, 2]], {k, 1, PeakPixelListLength}] /
       Sum[picScan[[PeakPixelList[[k, 1]], PeakPixelList[[k, 2]]]],
        {k, 1, PeakPixelListLength}];
     PeakX = Sum[picScan[[PeakPixelList[[k, 1]], PeakPixelList[[k, 2]]]] *
          PeakPixelList[[k, 1]], {k, 1, PeakPixelListLength}] /
       Sum[picScan[[PeakPixelList[[k, 1]], PeakPixelList[[k, 2]]]],
        {k, 1, PeakPixelListLength}];
     ROIx = ROIClipPrevent[Round[PeakX - δROIx / 2]];
     ROIy = ROIClipPrevent[Round[PeakY - δROIy / 2]];
     AppendTo[OptROIxTable, ROIx];
     AppendTo[OptROIyTable, ROIy],
     ROIx = ROIxInit;
     ROIy = ROIyInit]
    For[j = 0, j < δROIy, j++,
     newROI[[All, j + 1]] = Take[picScan[[All, j + ROIy]], {ROIx, ROIx + δROIx - 1}];
    ];
   intROI = Total[Total[newROI]];
   opt[[frame, tag[[frame, 5]] + 1]] = intROI
  ];
 ];
Histogram[OptROIxTable, {-0.5, 30.5, 1},
 Frame → True, PlotLabel → "ROI X distribution"]
Histogram[OptROIyTable, {-0.5, 30.5, 1}, Frame → True,
 PlotLabel → "ROI Y distribution"]
Export[StringJoin[StringReplace[FileName, ".pic" -> ""], "_opt.dat"], opt, "csv"];
```

Out[505]=

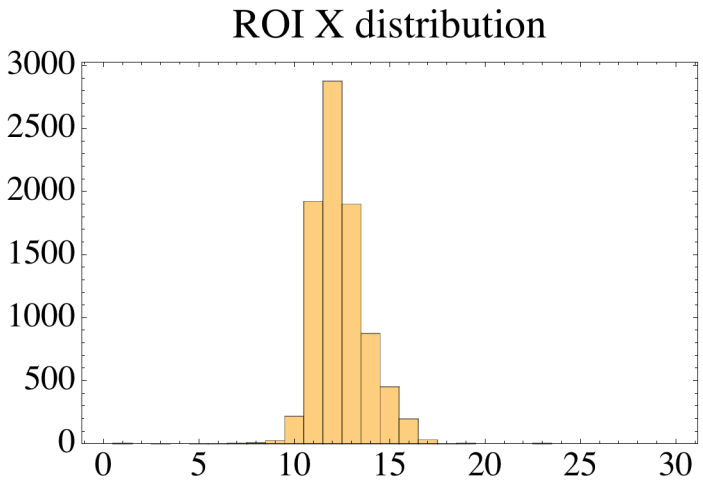

Out[506]=

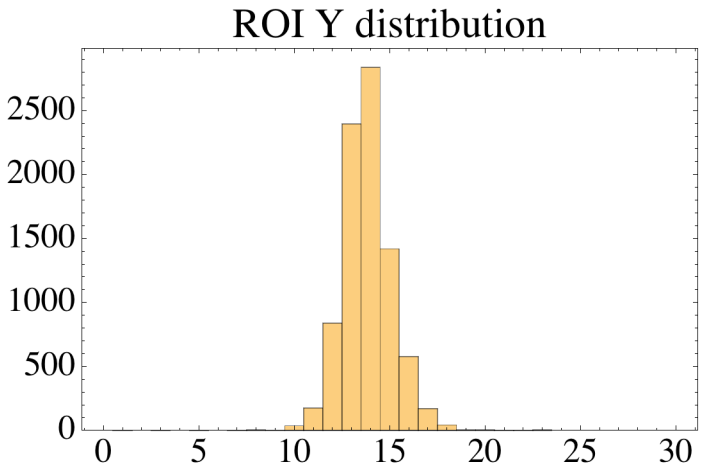

In[1]:=
```
(* ATTA Analysis Program, Ver. 3.6*)
Clear["Global`*"]
```

In[2]:=
```
Needs["ErrorBarPlots`"];
SetOptions[Plot, BaseStyle → {FontFamily → "Times", FontSize → 14}];
SetOptions[LogPlot, BaseStyle → {FontFamily → "Times", FontSize → 14}];
SetOptions[ListPlot, BaseStyle → {FontFamily → "Times", FontSize → 14}];
SetOptions[ListLinePlot, BaseStyle → {FontFamily → "Times", FontSize → 14}];
SetOptions[ListLogPlot, BaseStyle → {FontFamily → "Times", FontSize → 14}];
SetOptions[ListLogLogPlot, BaseStyle → {FontFamily → "Times", FontSize → 14}];
SetOptions[Histogram, BaseStyle → {FontFamily → "Times", FontSize → 14}];
(* Import Data: [1] Kr81, [2] Kr85, [3] Kr83 (quench), [4]
 (Do Not Use), [5] (Do Not Use), [6] Kr83 (ion), [7] σ of Kr83
 (ion), [8] Kr83 background, [9]σ of Kr83 background (ion) *)
FileName = "/Users/jczappala/Documents/Argonne National
    Laboratory/Dissertation/Analysis example/161020/RUN1/Modern_0000_opt.dat";
FileName2 = "/Users/jczappala/Documents/Argonne National
    Laboratory/Dissertation/Analysis example/161020/RUN1/Modern_0000.cfg";
config = Import[FileName2, "Table"];
data = Import[FileName, "CSV"];
style = {PlotRange → All, Frame → True,
   GridLines → Automatic, ImageSize → 1000, AspectRatio → 0.2};
(* Store and Plot *)
kr81 = Transpose[data][[1]] ;
kr85 = Transpose[data][[2]] ;
ions = Transpose[data][[6]];
err = Transpose[data][[7]];
bg = Transpose[data][[8]];
bgerr = Transpose[data][[9]];
ListLinePlot[{kr81, kr85} , Frame → True,
 PlotLabel → "Atom Counting: Red - 81Kr ; Blue - 85Kr", PlotRange → All,
 GridLines → Automatic, ImageSize → 1000, AspectRatio → 0.2,
 PlotStyle → {Red, Blue}, FrameLabel → {"Frames", "Signal (a.u.)"}]
ListLinePlot[{ions} , Frame → True, PlotLabel → "Ion signal for 83Kr",
 PlotRange → All, GridLines → Automatic, ImageSize → 1000, AspectRatio → 0.2,
 PlotStyle → {Purple}, FrameLabel → {"Frames", "Signal (V)"}]
ListLinePlot[{bg} , Frame → True, PlotLabel → "Background ion signal for 83Kr",
 PlotRange → All, GridLines → Automatic, ImageSize → 1000, AspectRatio → 0.2,
 PlotStyle → {Purple}, FrameLabel → {"Frames", "Signal (V)"}]
(* Collect the timing information and produce interval legnths *)
T1 = config[[6]];
T2 = config[[7]];
```

```
(* Functions for fixing the time format *)
AMPM[x_] := If[x == "PM", 12, 0];
TakeHour[T_] := ToExpression[StringTake[T, StringPosition[T, ":"][[1, 1]] - 1]];
TakeMin[T_] := ToExpression[StringTake[T,
    {StringPosition[T, ":"][[2, 1]] - 2, StringPosition[T, ":"][[2, 1]] - 1}]];
GetTime[T_] := TakeHour[T[[-2]]] +
   TakeMin[T[[-2]]] / 60.0 + AMPM[T[[-1]]] If[TakeHour[T[[-2]]] == 12, 0, 1];
(* Time and intervals for cutting, all in seconds*)
runTime = (GetTime[T2] - GetTime[T1]) * 3600;
(* Total measurement time in seconds*)
cycleTime = 0.44; (* Time per point *)(* Matches chopper speed *)
```

Out[21]=

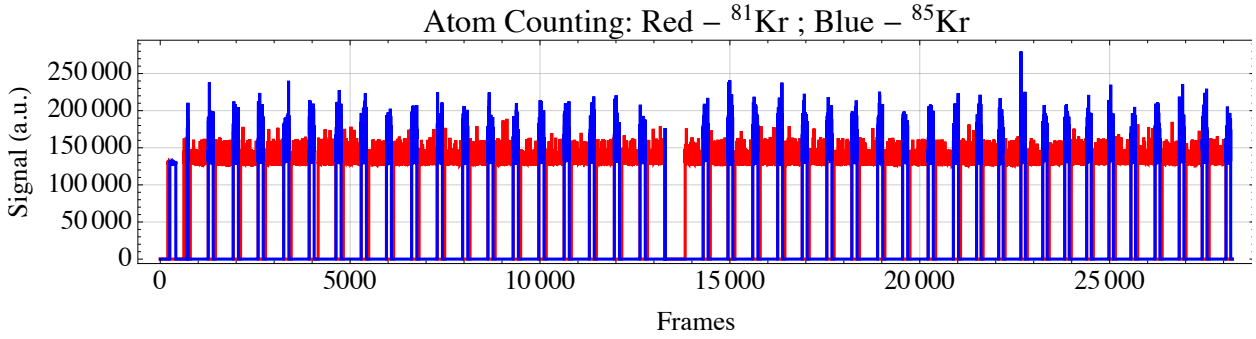

Out[22]=

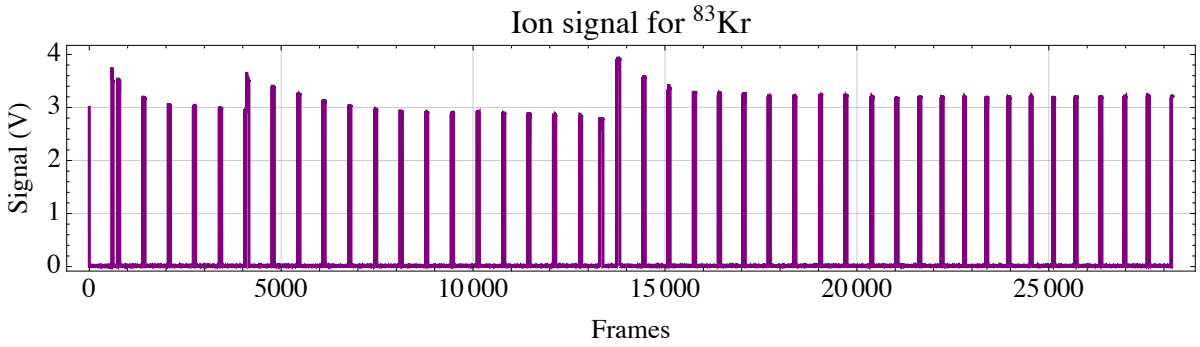

Out[23]=

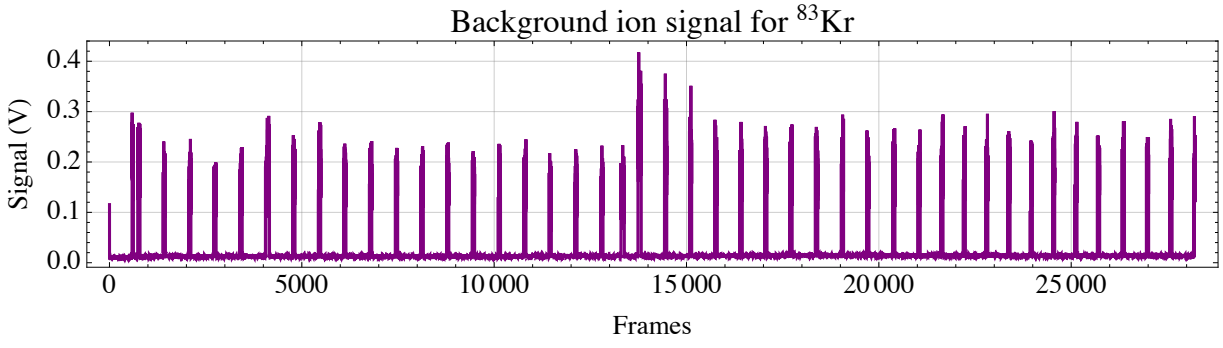

In[32]:=

```
(* Cut and concatenate signal *)
```

```
(* Removing laser jumps, and selecting section of run. Enter
 zero if a drop is uneeded. Please input in ascending order*)
drop1A = Input["Set first drop start point (zero if unused):", 1];
drop1B = Input["Set first drop end point (zero if unused):", 753];
If[drop1A > 0, slide = drop1B - drop1A + 1, slide = 0];
drop2A =  Input["Set second drop start point (zero if unused):", 2720];
drop2B = Input["Set second drop end point (zero if unused):", 2800];
If[drop2A > 0, slide2 = drop2B - drop2A + 1, slide2 = 0];
drop3A =  Input["Set third drop start point (zero if unused):", 0];
drop3B = Input["Set third drop end point (zero if unused):", 0];
If[drop3A > 0, slide3 = drop3B - drop3A + 1, slide3 = 0];
drop4A =  Input["Set third drop start point (zero if unused):", 12 820];
drop4B = Input["Set third drop end point (zero if unused):", Length[data]];
(* Length[data]-1*)
If[drop1A > 0, data = Drop[data, {drop1A, drop1B}]];
If[drop2A > 0, data = Drop[data, {drop2A - slide, drop2B - slide}]];
If[drop3A > 0,
  data = Drop[data, {drop3A - (slide + slide2), drop3B - (slide + slide2)}]];
If[drop4A > 0, data = Drop[data,
    {drop4A - (slide + slide2 + slide3), drop4B - (slide + slide2 + slide3)}]];
goodTime = Length[data] * cycleTime ;(* Total usable
 measurement time in seconds*)

(* Removing end if contamination became an issue *)
ending =
  Input["Enter total amount of data taking time to use in hours (default is
     full time minus laser jumps using GateTime):", N[goodTime / 3600]];
If[ending < N[goodTime / 3600], data = Drop[data,
    {Floor[ending * 3600 / cycleTime], Length[data]}]];
(* Check data cutting *)
kr81 = Transpose[data][[1]] ;
kr85 = Transpose[data][[2]] ;
ions = Transpose[data][[6]];
err = Transpose[data][[7]];
bg = Transpose[data][[8]];
bgerr = Transpose[data][[9]];
ListLinePlot[{kr81, kr85} , Frame → True,
 PlotLabel → "Atom Counting: Red - 81Kr ; Blue - 85Kr (jump and length corrected)",
 PlotRange → All, GridLines → Automatic, ImageSize → 1000, AspectRatio → 0.2,
 PlotStyle → {Red, Blue}, FrameLabel → {"Frames", "Signal (a.u.)"}]
ListLinePlot[{ions} , Frame → True,
 PlotLabel → "Ion signal for 83Kr (jump and length corrected)",
 PlotRange → All, GridLines → Automatic, ImageSize → 1000, AspectRatio → 0.2,
```

```
 PlotStyle → {Purple}, FrameLabel → {"Frames", "Signal (V)",}]
ListLinePlot[{bg} , Frame → True,
 PlotLabel → "Background ion signal for 83Kr (jump and length corrected)",
 PlotRange → All, GridLines → Automatic, ImageSize → 1000, AspectRatio → 0.2,
 PlotStyle → {Purple}, FrameLabel → {"Frames", "Signal (V)"}]
```

Out[56]=

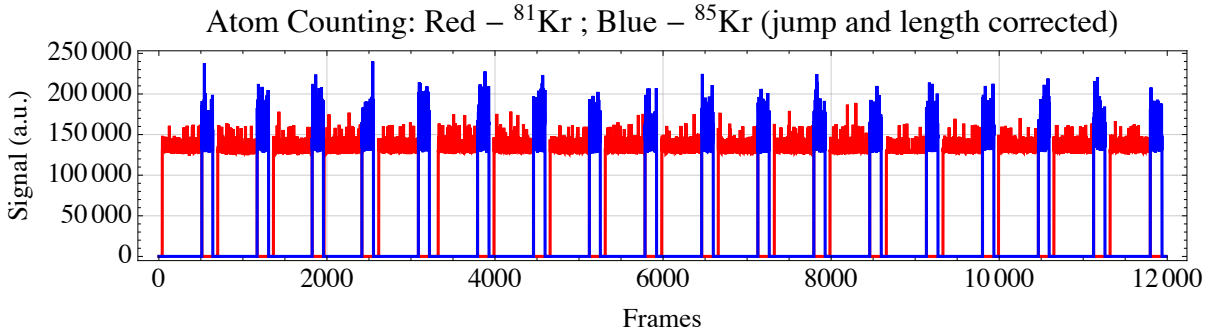

Out[57]=

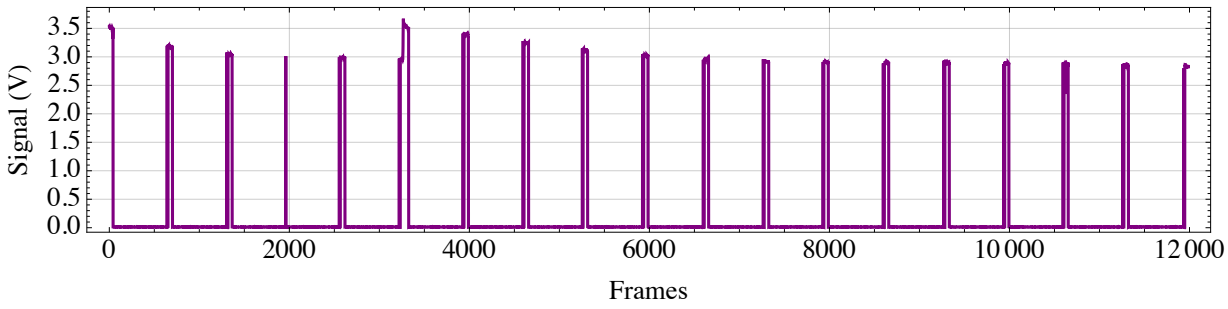

Out[58]=

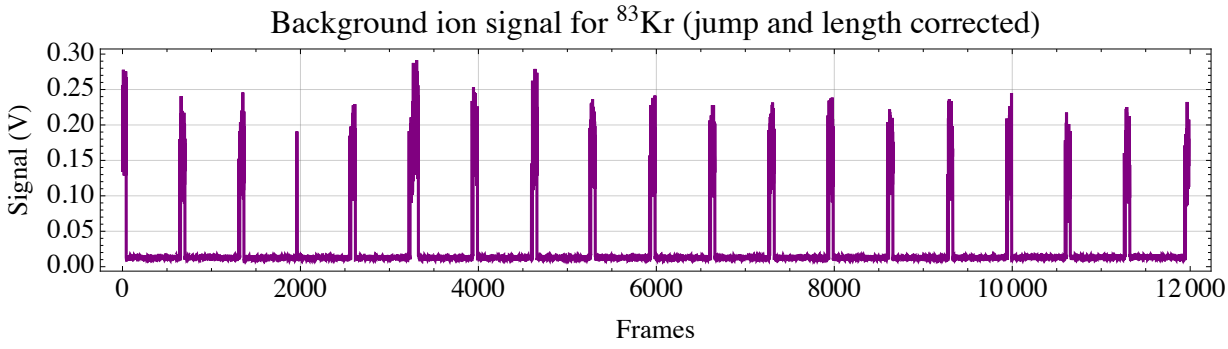

In[59]:=
```
(* Get background subtracted signals and fits *)

(* Kr83 Ion Signal *)
(* set thresholds *)
ionSen = Input["Set current amp sensativity (nA/V):", 2];
ionCut = Input["Set cutoff for ion signal:", 2.7];
bgCut = Input["Set cutoff for ion background:", 0.020];
ions = Select[ions, # > ionCut &];
bg = Select[bg, -0.02 < # < bgCut &];
ions1 = ions[[1 ;; Round[Length[ions] / 3]]];
ions2 = ions[[Round[Length[ions] / 3] ;; 2 * Round[Length[ions] / 3]]];
ions3 = ions[[2 * Round[Length[ions] / 3] ;; Length[ions]]];
bg1 = bg[[1 ;; Round[Length[bg] / 3]]];
bg2 = bg[[Round[Length[bg] / 3] ;; 2 * Round[Length[bg] / 3]]];
bg3 = bg[[Round[2 * Length[bg] / 3] ;; Length[bg]]];
(* plots for checking *)
ListLinePlot[ions, style, PlotLabel → "Ion signal for 83Kr",
 Joined → False, FrameLabel → {"Frames", "Signal (V)"}]
ListLinePlot[bg, style, PlotLabel → "Background signal for 83Kr",
 Joined → False, FrameLabel → {"Frames", "Signal (V)"}]
final83 = (Mean[ions] - Mean[bg]) * ionSen;
final831 = (Mean[ions1] - Mean[bg1]) * ionSen;
final832 = (Mean[ions2] - Mean[bg2]) * ionSen;
final833 = (Mean[ions3] - Mean[bg3]) * ionSen;
err83 = StandardDeviation[
   Take[ions, {Round[Length[ions] / 2] - 15, Round[Length[ions] / 2]}]];


(* Kr81 and Kr 85 Signal *)

(* Remove backgrounds *)

(* set thresholds *)
atomsCut = Input["Set cutoff for signals vs. zeros:", 90 000];
kr81 = Select[kr81, # > atomsCut &];
kr85 = Select[kr85, # > atomsCut &];
t81 = Length[kr81];
t85 = Length[kr85];
ListLinePlot[kr81, style, PlotLabel → "Kr-81 signal",
 PlotStyle → Red, FrameLabel → {"Frames", "Signal (a.u.)"}]
ListLinePlot[kr85, style, PlotLabel → "Kr-85 signal",
 PlotStyle → Blue, FrameLabel → {"Frames", "Signal (a.u.)"}]
```

Out[70]=

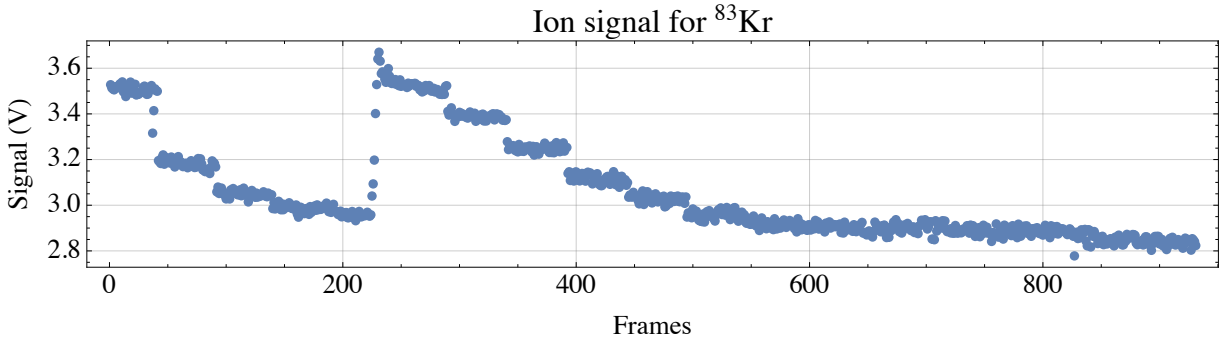

Out[71]=

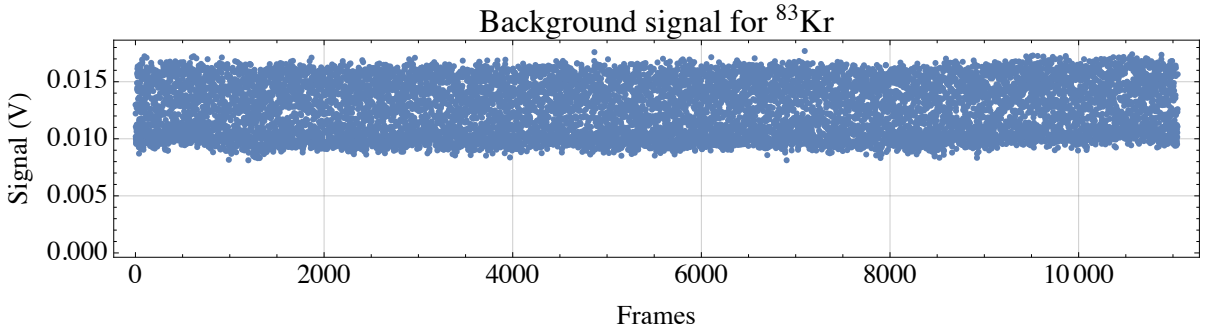

Out[82]=

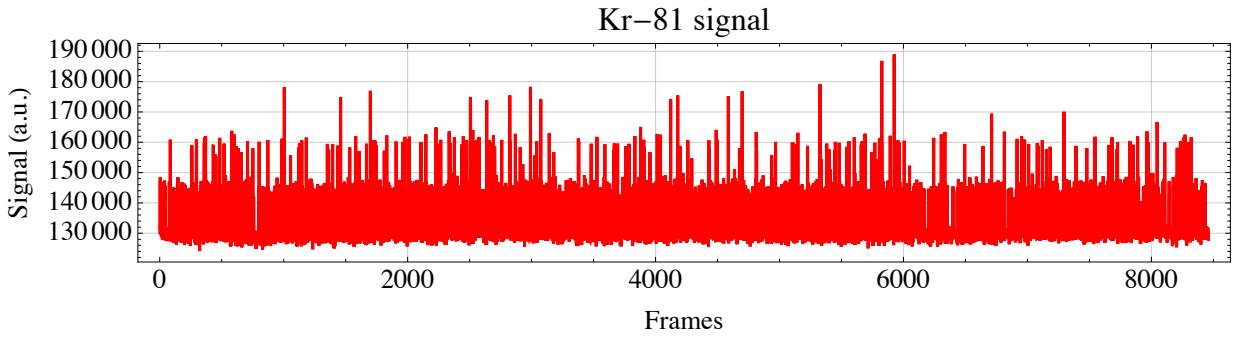

Out[83]=

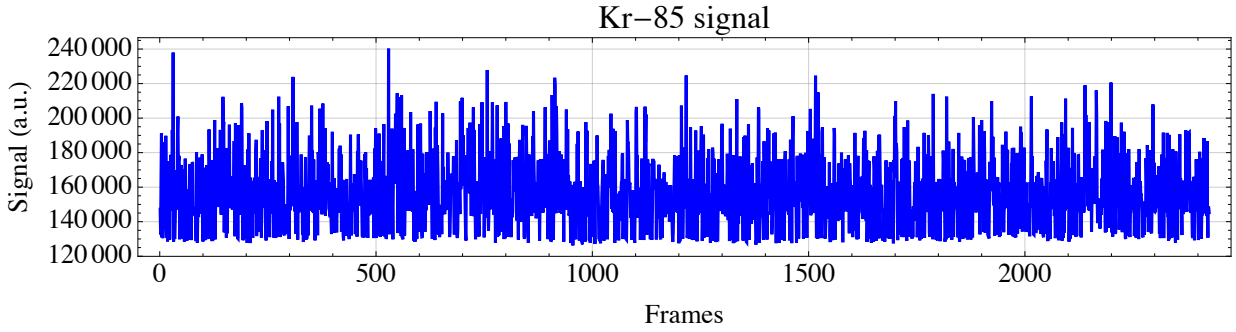

In[84]:=

```
(* collect baseline *)
base01 = Input["Set low baseline cut for 81:", 138 000];
base05 = Input["Set low baseline cut for 85:", 138 000];
base11 = Input["Set high baseline cut for 81:", 138 000];
base15 = Input["Set high baseline cut for 85:", 138 000];
decay81 =
```

```
  Input["Set points between baselines for 81 (make 0 for no slope):", 0];
decay85 = Input["Set points between baselines for 85 (make 0 for no slope):", 0];
baseCut1[x_] := Piecewise[
   {{base11 - ((base11 - base01) / decay81) * x, x < decay81}, {base01, x ≥ decay81}}];
baseCut5[x_] := Piecewise[{{base15 - ((base15 - base05) / decay85) * x, x < decay85},
    {base05, x ≥ decay85}}];
baseCut81 = Table[baseCut1[i], {i, t81}];
baseCut85 = Table[baseCut5[i], {i, t85}];
base81 = Table[i * cycleTime, {i, t81}, {j, 2}];
base85 = Table[i * cycleTime, {i, t85}, {j, 2}];
ListLinePlot[{kr81, baseCut81}, style, PlotLabel → " 81Kr signal",
 PlotStyle → {Red, Darker[Red]}, FrameLabel → {"Frames", "Signal (a.u.)"}]
ListLinePlot[{kr85, baseCut85}, style, PlotLabel → " 85Kr signal",
 PlotStyle → {Blue, Darker[Blue]}, FrameLabel → {"Frames", "Signal (a.u.)"}]
(* seperate baseline (interpolate)*)
For[i = 1, i < t81, i++
   If[kr81[[i]] < baseCut81[[i]],
    base81[[i, 2]] = kr81[[i]],
    base81[[i, 2]] = base81[[i, 1]] = -2]];
For[i = 1, i < t85, i++
   If[kr85[[i]] < baseCut85[[i]],
    base85[[i, 2]] = kr85[[i]],
    base85[[i, 2]] = base85[[i, 1]] = -2]];
base81 =
  Thread[{Select[base81[[All, 1]], # > -1 &], Select[base81[[All, 2]], # > 1 - 1 &]}];
base85 = Thread[{Select[base85[[All, 1]], # > -1 &],
    Select[base85[[All, 2]], # > -1 &]}];
baseFunc81 = Interpolation[base81, InterpolationOrder → 1, Method → "Spline"];
baseFunc85 = Interpolation[base85, InterpolationOrder → 0, Method → "Spline"];
bg81 = Table[baseFunc81[i * cycleTime], {i, 1, t81}];
bg85 = Table[baseFunc85[i * cycleTime], {i, 1, t85}];
(* smooth baseline *)
avgLen =
  Input["Average baseline over how many points (low pass filtering):", 10];
sbg81 = Table[0, {i, t81}];
sbg85 = Table[0, {i, t85}];
For[i = 1, i < t81 + 1, i++,
  sbg81[[i]] = If[i < t81 - avgLen,
    Mean[Take[bg81, {i, i + avgLen}]],
    Mean[Take[bg81, {i - avgLen, i}]]]];
For[i = 1, i < t85 + 1, i++,
  sbg85[[i]] = If[i < t85 - avgLen,
    Mean[Take[bg85, {i, i + avgLen}]],
```

```
    Mean[Take[bg85, {i - avgLen, i}]]]];
ListLinePlot[sbg81, style,
 PlotLabel → "Background for ⁸¹Kr, high frequencies removed",
 FrameLabel → {"Frames", "Signal (a.u.)"}]
ListLinePlot[sbg85, style,
 PlotLabel → "Background for ⁸⁵Kr, high frequencies removed",
 FrameLabel → {"Frames", "Signal (a.u.)"}]
For[i = 1, i < t81 + 1, i++,
  kr81[[i]] = kr81[[i]] - sbg81[[i]]];
For[i = 1, i < t85 + 1, i++,
  kr85[[i]] = kr85[[i]] - sbg85[[i]]];
ListLinePlot[kr81, style, PlotLabel → " ⁸¹Kr, background removed",
 FrameLabel → {"Frames", "Signal (a.u.)"}]
ListLinePlot[kr85, style, PlotLabel → " ⁸⁵Kr, background removed",
 FrameLabel → {"Frames", "Signal (a.u.)"}]
Histogram[kr81, 100, "LogCount", Frame → True, PlotRange → All,
 ChartStyle → {Darker[Red]}, PlotLabel → "Kr-81 counts",
 FrameLabel → {"Integrated signal", "Counts"}]
Histogram[kr85, 100, "LogCount", Frame → True, PlotRange → All,
 ChartStyle → {Darker[Blue]}, PlotLabel → "Kr-85 counts",
 FrameLabel → {"Integrated signal", "Counts"}]
```

Out[96]=

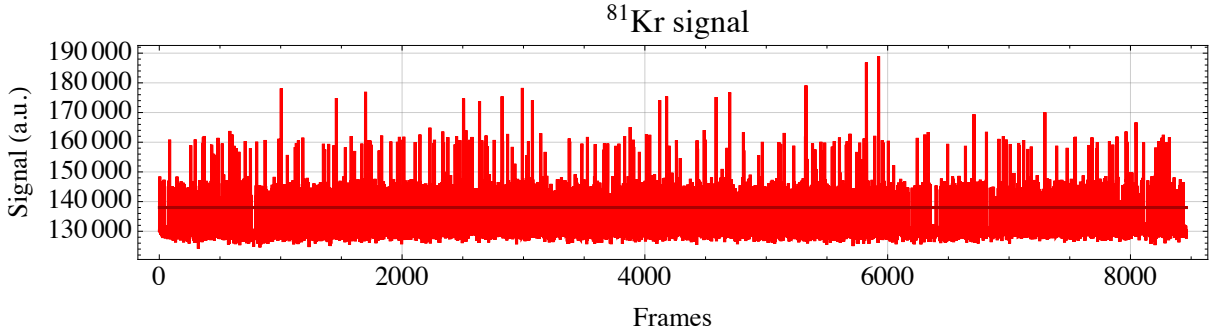

Out[97]=

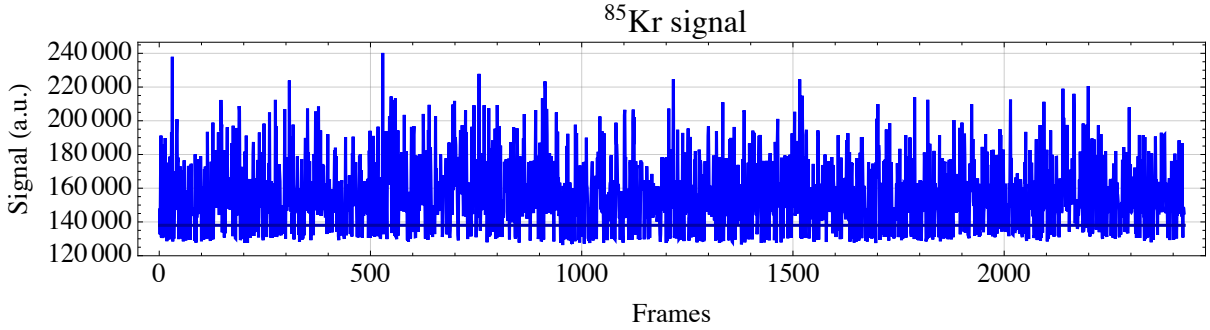

Out[111]=

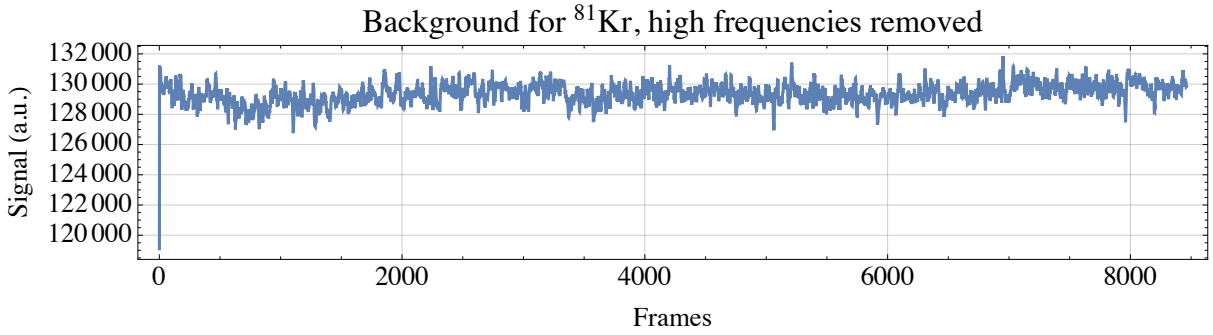

Out[112]=

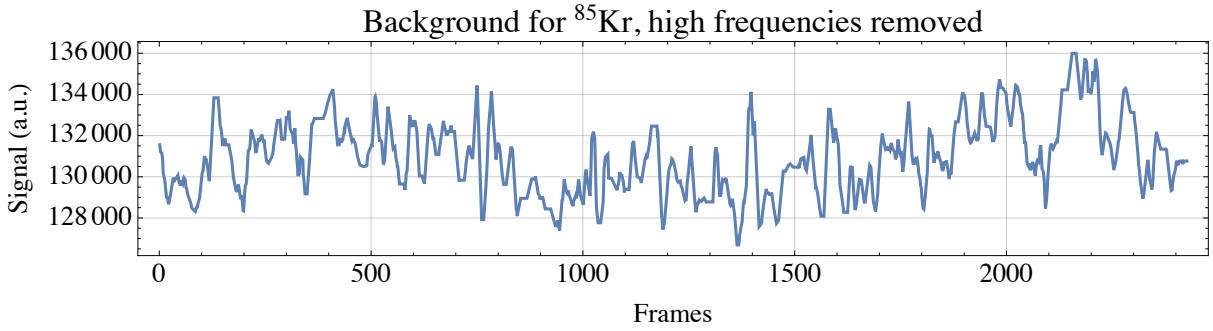

Out[115]=

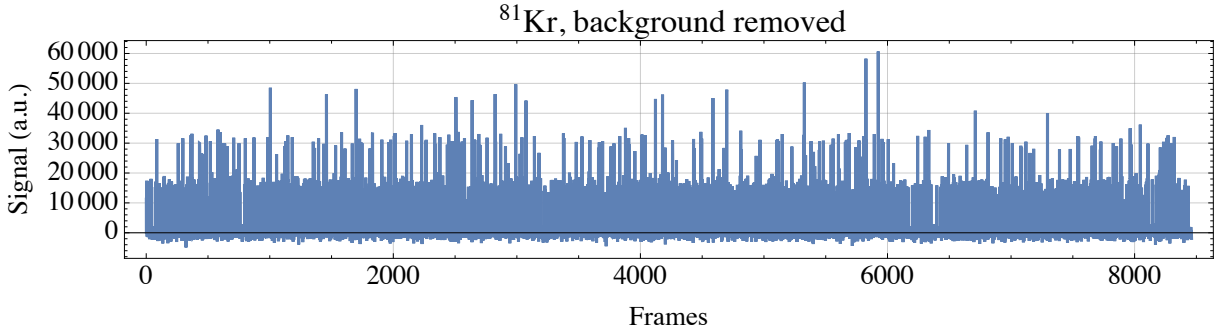

Out[116]=

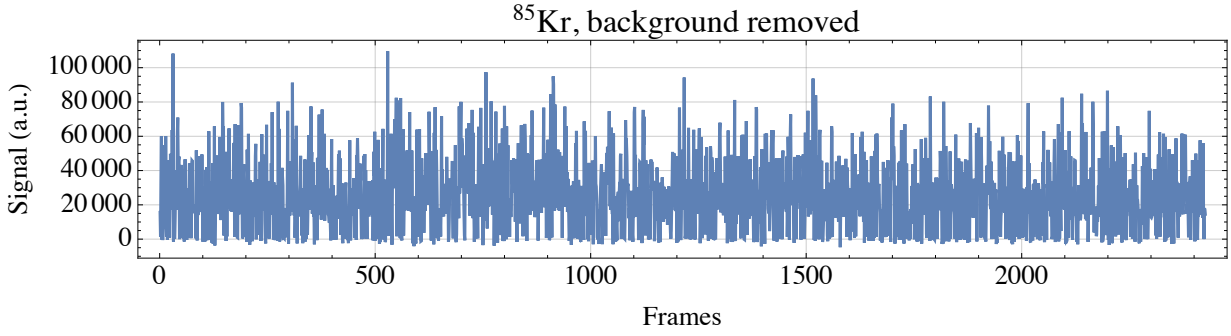

Out[117]=

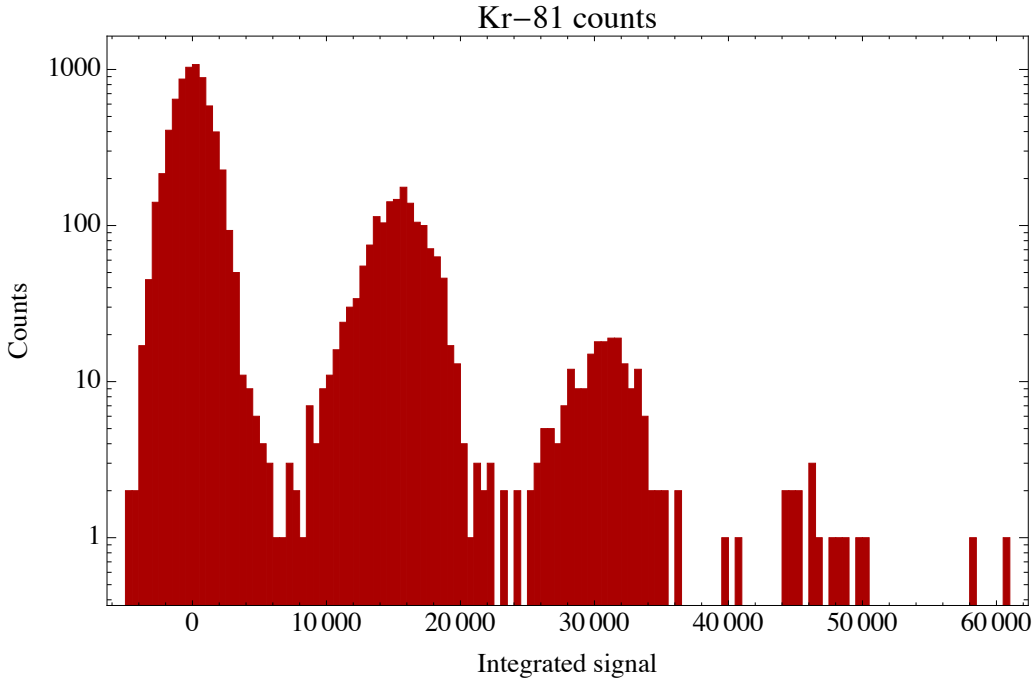

Out[118]=

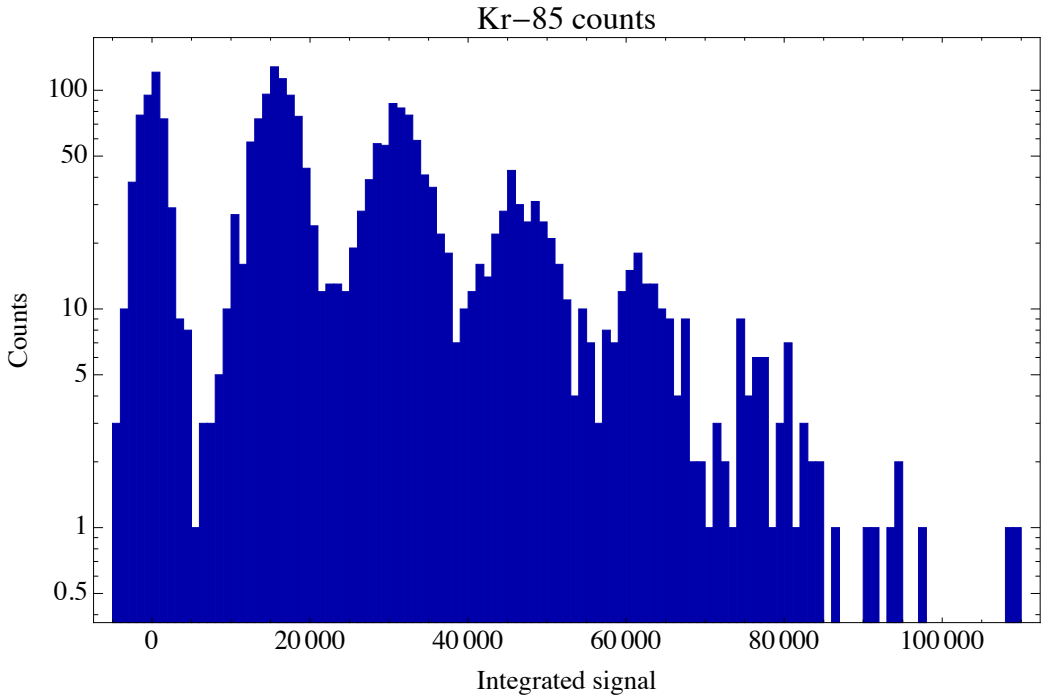

In[119]:=
```
export = Input["Export? (2 for 85 lifetime, 1 for yes, 0 for no):", 0];
(* Fit data *)
binSize = Input["Insert histogram bin size for fitting:", 500];

(* put histogram data into plot *)
{histCount81, {counter81}} = Reap[Histogram[kr81,
    {Min[kr81], Max[kr81], binSize}, Function[{bins, counts}, Sow[counts]]]];
binAxis = Table[i * binSize + Min[kr81], {i, Length[counter81[[1]]]}];
prepData = Thread[{binAxis, counter81[[1]]}];
prep = ListLogPlot[prepData, style];
{histCount85, {counter85}} = Reap[Histogram[kr85,
    {Min[kr85], Max[kr85], binSize}, Function[{bins, counts}, Sow[counts]]]];
binAxis2 = Table[i * binSize + Min[kr85], {i, Length[counter85[[1]]]}];
prepData2 = Thread[{binAxis2, counter85[[1]]}];
prep2 = ListLogPlot[prepData2, style];

If[export == 1, {Export[
   StringJoin[StringReplace[FileName, ".dat" -> ""], "_raw81.dat"], kr81, "csv"],
  Export[StringJoin[StringReplace[FileName, ".dat" -> ""], "_raw85.dat"],
   kr85, "csv"],
  Export[StringJoin[StringReplace[FileName, ".dat" -> ""], "_hist81.dat"],
   prepData, "csv"],
  Export[StringJoin[StringReplace[FileName, ".dat" -> ""], "_hist85.dat"],
   prepData2, "csv"]},
 If[export == 2, Export[StringJoin[StringReplace[FileName, ".dat" -> ""],
    "_2braw85.dat"], kr85, "csv"], Print["No export"]]]
```

```
No export
```

In[212]:=
```
(* Some fitting constants *)
η1 = 15 500 / 3000.0;
η5 = 15 500 / 3000.0;
a1Max = 1000;
a0Max = 3000;

(* Kr81 *)

(* Create fit for data *)
peaks81 =  Input["Number of atom peaks to fit for Kr81:", 2];
(* prep constants *)
Clear[A, X0, xs, xs0, a0, a1, a2, a3, x0, x1, x2, x3]
A = {a0, a1, a2, a3};
X0 = {x0, x1, x2, x3};
gaussian81[x_] := A[[1]] * Exp[-(x - xs0)^2 / (2 * X0[[1]]^2)] +
   A[[2]] * Exp[-(x - (xs) - xs0)^2 / (2 * X0[[2]]^2)] +
```

```
    If[peaks81 > 1, A[[3]] * Exp[-(x - (2 * xs) - xs0)^2 / (2 * X0[[3]]^2)], 0] +
    If[peaks81 > 2, A[[4]] * Exp[-(x - (3 * xs) - xs0)^2 / (2 * X0[[4]]^2)], 0];
fit = FindFit[prepData, {gaussian81[x], {0 < a0 < a0Max, 0 < a1 < a1Max,
      0 < a2 < a1Max, 0 < a3 < a1Max, 50 * η1 < x0 < 1200 * η1, 100 * η1 < x1 < 500 * η1,
      x1 < x2 < 3000 * η1, x2 < x3 < 5000 * η1, -700 < xs0 < 700, 2900 * η1 < xs < 3300 * η1}},
    {a0, a1, a2, a3, x0, x1, x2, x3, xs, xs0}, x];
A = {a0 /. fit, a1 /. fit, a2 /. fit, a3 /. fit};
X0 = {x0 /. fit, x1 /. fit, x2 /. fit, x3 /. fit};
xs0 = xs0 /. fit;
xs = xs /. fit;
ht81 = xs;
Gauss = LogPlot[gaussian81[x], {x, Min[kr81], Max[kr81]},
    PlotRange → {10^-4, 10^4}, Frame → True, GridLines → Automatic,
    PlotStyle → {Red, Thick}, FrameLabel → {"Integrated signal", "Counts"}];
quant = Plot[SquareWave[{-9, 9}, x / (2 * xs)], {x, Min[kr81], Max[kr81]},
    PlotStyle → Transparent, ExclusionsStyle → {{Purple, Thick}, Yellow}];
Show[Gauss, prep, quant]

(*Select single atoms via quantization*)
thresh = Input["Threshold for number of σ confidence in atom count (Kr81):", 6];
level = thresh * X0[[1]] / xs;
atoms81 = Table[0, {i, Length[kr81]}];
check = ListPlot[kr81 / xs, PlotRange -> All];
check2 = Plot[level, {x, 0, Length[kr81]}];
Show[check, check2]
For[i = 1, i < Length[kr81] + 1, i++,
  atoms81[[i]] = If[kr81[[i]] / xs > level, Round[kr81[[i]] / xs], 0]];
ListLinePlot[atoms81, Frame → True, GridLines → Automatic, Filling → Bottom,
 FillingStyle → Orange, ImageSize → 700, AspectRatio → 0.2, PlotRange → Full]
final81 = Total[atoms81];
final811 = Total[atoms81[[1 ;; Round[Length[atoms81] / 3]]]];
final812 =
  Total[atoms81[[Round[Length[atoms81] / 3] ;; 2 * Round[Length[atoms81] / 3]]]];
final813 = Total[atoms81[[2 * Round[Length[atoms81] / 3] ;; Length[atoms81]]]];

(*Error estimation*)
(*Count a background as a atom*)
error81 = N[Erfc[thresh] * Length[kr81] / final81];
(*Miss a atom, treated as background*)
missing81 = N[Erfc[(xs - level * xs) / (X0[[2]])]];

(* Kr85 *)
```

```
(* Create fit for data *)
peaks85 = Input["Number of atom peaks to fit for Kr85:", 3];
(* prep constants *)
Clear[A, X0, xs, xs0, a0, a1, a2, a3, x0, x1, x2, x3]
A = {a0, a1, a2, a3};
X0 = {x0, x1, x2, x3};
gaussian85[x_] := A[[1]] * Exp[-(x - xs0)^2 / (2 * X0[[1]]^2)] +
  A[[2]] * Exp[-(x - (xs) - xs0)^2 / (2 * X0[[2]]^2)] +
  If[peaks85 > 1, A[[3]] * Exp[-(x - (2 * xs) - xs0)^2 / (2 * X0[[3]]^2)], 0] +
  If[peaks85 > 2, A[[4]] * Exp[-(x - (3 * xs) - xs0)^2 / (2 * X0[[4]]^2)], 0]
fit = FindFit[prepData2, {gaussian85[x], {0 < a0 < a0Max, 0 < a1 < a1Max,
      0 < a2 < a1Max, 0 < a3 < a1Max, 25 * η5 < x0 < 1000 * η5, 50 * η5 < x1 < 1500 * η5,
      x1 < x2 < 3000 * η5, x2 < x3 < 5000 * η5, -700 < xs0 < 700, 2900 * η5 < xs < 3300 * η5}},
    {a0, a1, a2, a3, x0, x1, x2, x3, xs, xs0}, x];
A = {a0 /. fit, a1 /. fit, a2 /. fit, a3 /. fit};
X0 = {x0 /. fit, x1 /. fit, x2 /. fit, x3 /. fit};
xs0 = xs0 /. fit;
xs = xs /. fit;
ht85 = xs;
Gauss2 = LogPlot[gaussian85[x], {x, Min[kr85], Max[kr85]},
    PlotRange → {10^-4, 10^4}, Frame → True, GridLines → Automatic,
    PlotStyle → {Green, Thick}, FrameLabel → {"Integrated signal", "Counts"}];
quant2 = Plot[SquareWave[{-9, 9}, x / (2 * xs)], {x, Min[kr85], Max[kr85]},
    PlotStyle → Transparent, ExclusionsStyle → {{Purple, Thick}, Yellow}];
Show[Gauss2, prep2, quant2]

(*Select single atoms via quantization*)
thresh = Input["Threshold for number of σ confidence in atom count (Kr85):", 6];
level = thresh * X0[[1]] / xs;
atoms85 = Table[0, {i, Length[kr85]}];
For[i = 1, i < Length[kr85] + 1, i++,
  atoms85[[i]] = If[kr85[[i]] / xs > level, Round[kr85[[i]] / xs], 0]];
ListLinePlot[atoms85, Frame → True, GridLines → Automatic, Filling → Bottom,
 FillingStyle → Orange, ImageSize → 700, AspectRatio → 0.2, PlotRange → Full]
final85 = Total[atoms85];
final851 = Total[atoms85[[1 ;; Round[Length[atoms85] / 3]]]];
final852 =
  Total[atoms85[[Round[Length[atoms85] / 3] ;; 2 * Round[Length[atoms85] / 3]]]];
final853 = Total[atoms85[[2 * Round[Length[atoms85] / 3] ;; Length[atoms85]]]];

(*Error estimation*)
(*Count a background as a atom*)
error85 = N[Erfc[thresh] * Length[kr85] / final85];
```

```
(*Miss a atom, treated as background*)
missing85 = N[Erfc[(xs - level * xs) / (X0[[2]])]];

(*Print all information*)
ListLinePlot[ions, style, PlotLabel → "Ion signal for 83Kr", Joined → False]
Print[FileName2]
Print["Measurement Time: ", runTime / 3600, " hours."]
Print["Analysis Time Used: " , ending, " hours."]
Print[""]
Print[ "Kr Loading Rate: ", (t81 * cycleTime) / final81,
 " seconds per atom. Determined from ", final81,
 " 81Kr atoms detected in ", t81 * cycleTime, " seconds."]
Print["Single Atom Height for 81Kr: ", ht81]
Print["The error rate for 81Kr atoms is ",
 error81 * 100, "% and the missing rate is ", missing81 * 100 "%."]
Print[""]
Print[ "Kr Loading Rate: ", (t85 * cycleTime) / final85,
 " seconds per atom. Determined from ", final85,
 " 85Kr atoms detected in ", t85 * cycleTime, " seconds."]
Print["Single Atom Height for 85Kr: ", ht85]
Print["The error rate for 85Kr atoms is ",
 error85 * 100, "% and the missing rate is ", missing85 * 100 "%."]
Print[""]
Print["The average ion signal for the 83Kr loading rate was ",
 final83, " (in nA) with an error of ", err83, "."]
Grid[{{"Kr81 time", "Kr81 counts", "Kr85 time" , "Kr85 counts",
    "Kr83 signal", "Kr81/Kr83 (a/hr/nA)", "Kr85/Kr83 (a/hr/nA)"},
  {(t81 * cycleTime / 3), final811, (t85 * cycleTime / 3), final851,
    final831, final811 * 3600 / ((t81 * cycleTime / 3) * final831),
    final851 * 3600 / ((t85 * cycleTime / 3) * final831)},
  {(t81 * cycleTime / 3), final812, (t85 * cycleTime / 3), final852,
    final832, final812 * 3600 / ((t81 * cycleTime / 3) * final832),
    final852 * 3600 / ((t85 * cycleTime / 3) * final832)},
  {(t81 * cycleTime / 3), final813, (t85 * cycleTime / 3), final853,
    final833, final813 * 3600 / ((t81 * cycleTime / 3) * final833),
    final853 * 3600 / ((t85 * cycleTime / 3) * final833)}}, Frame → All]
```

Out[229]=

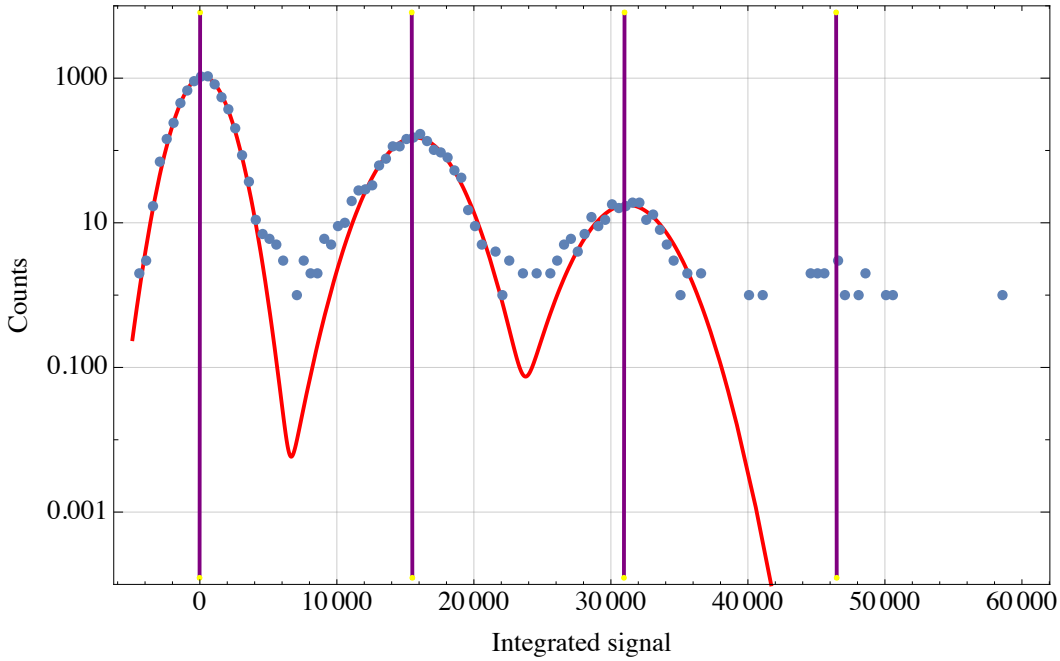

Out[237]=

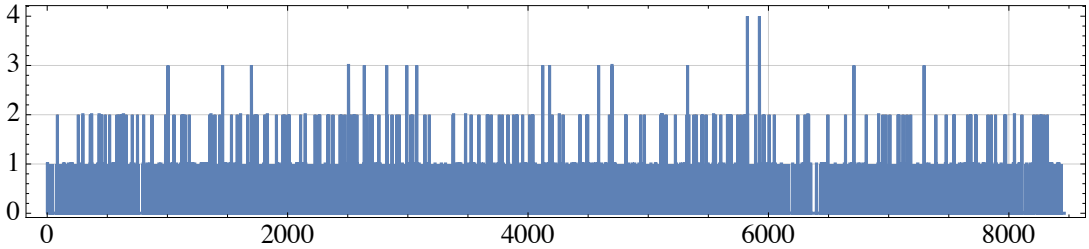

Out[257]=

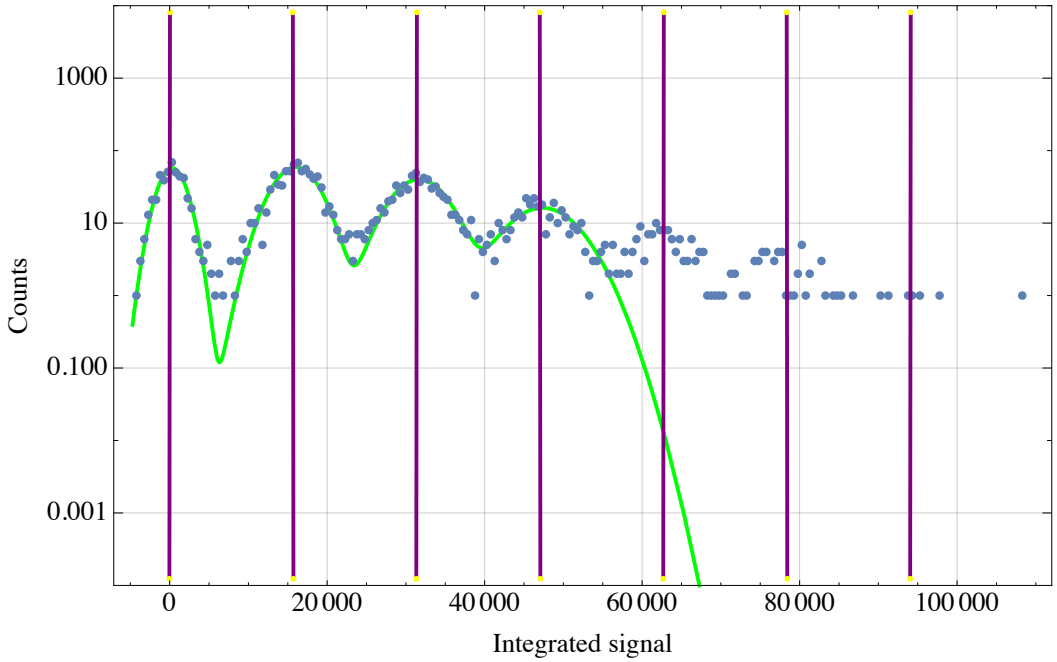

Out[262]=

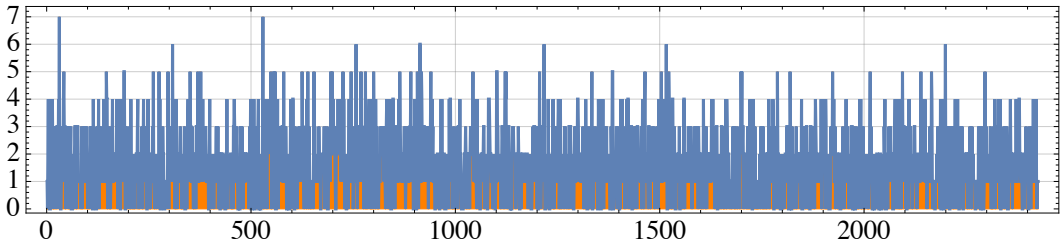

Out[269]=

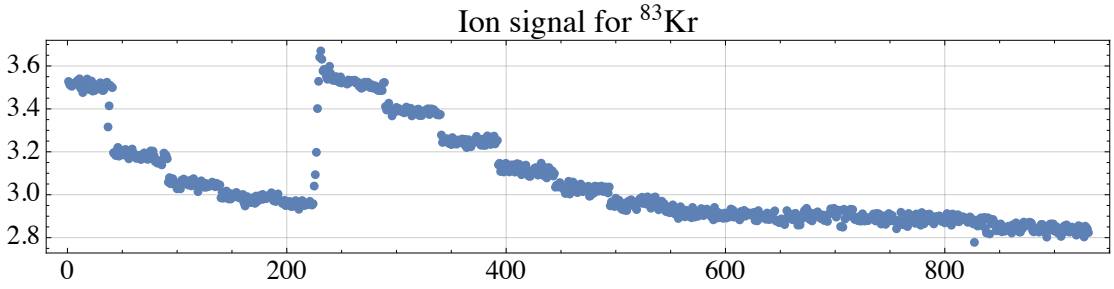

/Users/jczappala/Documents/Argonne National Laboratory/Dissertation/Analysis example/161020/RUN1/Modern_0000.cfg

Measurement Time: 4.7 hours.

Analysis Time Used: 1.46483 hours.

Kr Loading Rate: 1.88881 seconds per atom. Determined from 1971 ^{81}Kr atoms detected in 3722.84 seconds.

Single Atom Height for ^{81}Kr: 15486.8

The error rate for ^{81}Kr atoms is 9.23787×10^{-15}% and the missing rate is 1.07119×10^{-6} %.

Kr Loading Rate: 0.275326 seconds per atom. Determined from 3877 ^{85}Kr atoms detected in 1067.44 seconds.

Single Atom Height for ^{85}Kr: 15679.5

The error rate for ^{85}Kr atoms is 1.34658×10^{-15}% and the missing rate is 0.105411 %.

The average ion signal for the ^{83}Kr loading rate was 6.09704 (in nA) with an error of 0.0172075.

Out[283]=

Kr81 time	Kr81 counts	Kr85 time	Kr85 counts	Kr83 signal	Kr81/Kr83 (a/hr/nA)	Kr85/Kr83 (a/hr/nA)
1240.95	708	355.813	1355	6.43657	319.101	2129.93
1240.95	673	355.813	1350	6.12829	318.585	2228.82
1240.95	590	355.813	1174	5.72974	298.722	2073.07

```
(* Poisson Distruibution *)
```

In[202]:=
```
poi = BinCounts[atoms81, {0, 12, 1}];
poiNorm = Table[N[poi[[i]] / Total[poi]], {i, Length[poi]}];
switch = Table[i * 1 - 1, {i, Length[poiNorm]}];
poisson = Thread[{switch, poiNorm}]
fitP = FindFit[poisson, {PDF[PoissonDistribution[μ], x], {0 < μ < 7}}, {μ}, x];
μ /. fitP
Charlie = DiscretePlot[
   PDF[PoissonDistribution[μ /. fitP], x], {x, 0, 12}, PlotStyle → Green];
Paul = DiscretePlot[PDF[PoissonDistribution[0.5], x],
   {x, 0, 10}, PlotStyle → Purple];
poissonAtoms = ListPlot[poisson, PlotStyle → Pink, PlotRange → All];
Show[poissonAtoms, Charlie]
```

Out[205]=
```
{{0, 0.79506}, {1, 0.179411}, {2, 0.0232833}, {3, 0.00200922},
 {4, 0.000236379}, {5, 0.}, {6, 0.}, {7, 0.}, {8, 0.}, {9, 0.}, {10, 0.}, {11, 0.}}
```

Out[207]=
```
0.22798
```

Out[211]=

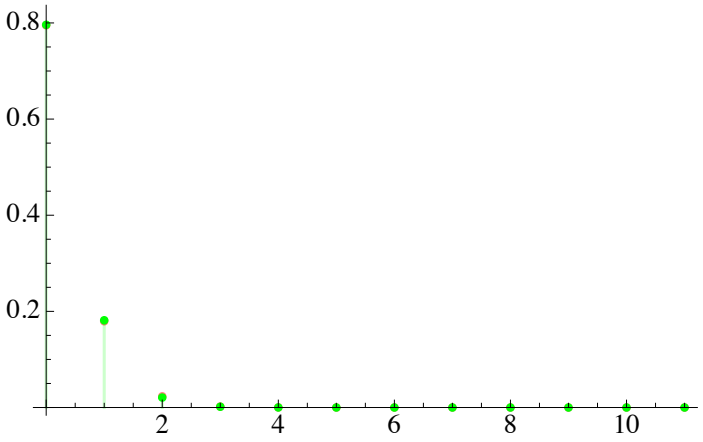

APPENDIX C

ATTA RESULTS: MAY 2014 - FEBRUARY 2017

Table C.1 includes all of the final reported $^{81}Kr/^{81}Kr_{atmosphere}$ ratios and ^{85}Kr activities (in dpm/cc) of samples measured for the various applications covered under the umbrella of this disserration, i.e. from May 2014 - February 2017. Sample associations with the projects as detailed in Chapter 6 are noted in the last column of the table. After Table C.1, we have included an example template of the reports submitted to collaborators with these results in Figure C.1. We have not included the reports due to copyright issues. However, the author may be contacted to obtain information on samples not included in this Appendix, but typically included in the report, such as sampling dates, analysis dates, sampling locations, etc.

ATTA Trace No.	$^{81}Kr/^{81}Kr_{atmosphere}$	^{85}Kr **activity**	**Project**
10104	1.02 ± 0.04	92.3 ± 1.6	IAEA
10105	0.95 ± 0.04	<0.71 (90% C.L.)	IAEA
10105	1.02 ± 0.05	<0.65 (90% C.L.)	IAEA
10106	0.29 ± 0.04	1.55 ± 0.42	South Africa
10107	1.01 ± 0.04	68.3 ± 1.4	South Africa
10108	1.08 ± 0.05	68.0 ± 1.4	South Africa
10109	0.74 ± 0.04	0.55 ± 0.56	IAEA
10110	0.86 ± 0.04	<0.18 (90% C.L.)	IAEA
10111	0.95 ± 0.04	50.5 ± 1.2	IAEA
10112	0.10 ± 0.06	9.4 ± 1.2	BAB
10113	0.87 ± 0.05	<0.30 (90% C.L.)	IAEA
10114	0.06 ± 0.03	<0.17 (90% C.L.)	IAEA
10115	0.65 ± 0.06	0.76 ± 0.49	IAEA
10116	0.72 ± 0.04	<0.26 (90% C.L.)	IAEA
10117	0.49 ± 0.04	1.11 ± 0.50	IAEA
10118	0.31 ± 0.06	0.78 ± 0.48	IAEA
10119	0.90 ± 0.05	<0.47 (90% C.L.)	IAEA
10120	1.05 ± 0.05	<0.27 (90% C.L.)	IAEA
10121	0.90 ± 0.04	<0.75 (90% C.L.)	Israel I
10122	0.92 ± 0.05	<0.39 (90% C.L.)	Israel I
10123	0.90 ± 0.04	<0.24 (90% C.L.)	Israel I
10124	0.82 ± 0.04	<0.30 (90% C.L.)	Israel I
10125	0.96 ± 0.05	7.67 ± 0.59	Israel I

10126	1.05 ± 0.05	<0.35 (90% C.L.)	Israel I
10127	0.63 ± 0.03	<0.40 (90% C.L.)	Israel I
10128	0.75 ± 0.04	<0.57 (90% C.L.)	Israel I
10129	0.87 ± 0.04	<0.21 (90% C.L.)	Israel I
10130	0.49 ± 0.04	1.16 ± 0.58	Israel I
10131	0.63 ± 0.04	<0.32 (90% C.L.)	Israel I
10133	0.37 ± 0.03	<0.42 (90% C.L.)	Israel I
10136	0.96 ± 0.04	<0.68 (90% C.L.)	Israel I
10137	1.10 ± 0.05	<0.55 (90% C.L.)	Israel I
10138	0.99 ± 0.04	<0.40 (90% C.L.)	Israel I
10139	0.88 ± 0.04	2.94 ± 0.47	Israel I
10140	0.91 ± 0.04	<0.31 (90% C.L.)	Israel I
10141	0.70 ± 0.04	0.95 ± 0.43	Israel I
10142	1.07 ± 0.05	<0.60 (90% C.L.)	Israel I
10143	0.57 ± 0.03	1.25 ± 0.41	IAEA
10144	0.86 ± 0.04	1.28 ± 0.42	IAEA
10145	0.94 ± 0.04	<0.51 (90% C.L.)	Israel I
10148	0.15 ± 0.02	<0.80 (90% C.L.)	Israel I
10149	0.37 ± 0.03	<0.51 (90% C.L.)	Israel I
10150	0.90 ± 0.05	<0.27 (90% C.L.)	Israel I
10151	0.71 ± 0.04	<0.83 (90% C.L.)	Israel I
10152	0.51 ± 0.03	<0.85 (90% C.L.)	Israel I
10153	0.56 ± 0.03	5.50 ± 0.46	Israel I
10154	0.70 ± 0.03	<0.25 (90% C.L.)	Israel I
10155	2.370 ± 0.056	5.84 ± 0.20	Neutron Capture
10156	0.96 ± 0.05	0.70 ± 0.32	IAEA
10157	0.89 ± 0.03	<0.71 (90% C.L.)	IAEA
10158	0.28 ± 0.02	1.73 ± 0.26	IAEA
10159	0.79 ± 0.03	1.51 ± 0.34	IAEA
10160	0.66 ± 0.03	0.88 ± 0.27	IAEA
10161	0.30 ± 0.02	0.34 ± 0.25	Israel I
10166	0.28 ± 0.02	1.41 ± 0.43	IAEA
10167	0.87 ± 0.03	4.98 ± 0.34	IAEA
10168	0.10 ± 0.01	<0.63 (90% C.L.)	IAEA
10169	0.17 ± 0.02	2.51 ± 0.37	IAEA
10170	0.20 ± 0.01	1.74 ± 0.32	IAEA
10171	0.19 ± 0.01	1.26 ± 0.32	IAEA
10172	0.17 ± 0.01	0.74 ± 0.33	IAEA
10173	0.55 ± 0.02	0.95 ± 0.35	Israel I
10174	0.37 ± 0.03	<0.71 (90% C.L.)	Israel I
10176	0.63 ± 0.02	0.83 ± 0.09	IAEA
10177	0.15 ± 0.01	0.44 ± 0.18	IAEA

10178	0.72 ± 0.03	0.97 ± 0.15	IAEA
10180	1.01 ± 0.04	3.23 ± 0.29	IAEA
10181	0.23 ± 0.02	0.15 ± 0.23	IAEA
10182	0.16 ± 0.01	<0.38 (90% C.L.)	IAEA
10183	0.79 ± 0.03	0.24 ± 0.27	IAEA
10184	0.24 ± 0.02	0.86 ± 0.46	IAEA
10185	0.95 ± 0.04	1.98 ± 0.17	IAEA
10186	0.87 ± 0.04	3.39 ± 0.27	IAEA
10187	0.89 ± 0.03	0.20 ± 0.05	Floridan Aquifer
10188	0.93 ± 0.04	0.27 ± 0.09	Floridan Aquifer
10189	0.91 ± 0.04	0.75 ± 0.19	Floridan Aquifer
10190	0.95 ± 0.04	0.20 ± 0.09	Floridan Aquifer
10191	0.90 ± 0.03	<0.34 (90% C.L.)	Floridan Aquifer
10192	0.95 ± 0.03	0.14 ± 0.09	Floridan Aquifer
10193	0.90 ± 0.03	0.16 ± 0.10	Floridan Aquifer
10194	1.02 ± 0.04	0.44 ± 0.10	Floridan Aquifer
10196	0.49 ± 0.02	7.21 ± 0.36	WIPP
10197	0.58 ± 0.03	5.90 ± 0.34	WIPP
10198	1.05 ± 0.05	2.16 ± 0.22	WIPP
10199	0.26 ± 0.02	3.37 ± 0.31	Etsch Valley
10200	0.80 ± 0.08	3.37 ± 0.77	IAEA
10201	0.65 ± 0.05	1.57 ± 0.32	IAEA
10202	0.17 ± 0.05	<0.65 (90% C.L.)	IAEA
10209	0.85 ± 0.16	26.7 ± 5.1	IAEA
10210*	n/a	54.0 ± 2.3	Isodetect GmbH
10211*	n/a	46.9 ± 2.2	Isodetect GmbH
10212*	n/a	44.0 ± 1.8	Isodetect GmbH
10213*	n/a	26.0 ± 1.3	Isodetect GmbH
10214*	n/a	1.26 ± 0.34	Isodetect GmbH
10215*	n/a	54.8 ± 2.3	Isodetect GmbH
10216*	n/a	2.37 ± 0.30	Isodetect GmbH
10217*	n/a	67.3 ± 3.2	Isodetect GmbH
10218*	n/a	52.8 ± 2.2	Isodetect GmbH
10219*	n/a	2.58 ± 0.51	Isodetect GmbH
10234	0.41 ± 0.02	<0.49 (90% C.L.)	Israel II
10235	0.32 ± 0.02	<0.45 (90% C.L.)	Israel II
10236	0.36 ± 0.02	<0.50 (90% C.L.)	Israel II
10237	0.346 ± 0.015	<0.47 (90% C.L.)	Israel II
10238	0.28 ± 0.02	<0.50 (90% C.L.)	Israel II
10239	0.313 ± 0.014	<0.64 (90% C.L.)	Israel II
10240	0.71 ± 0.02	<0.49 (90% C.L.)	Israel II
10241	0.68 ± 0.03	<0.56 (90% C.L.)	Israel II

10242	0.48 ± 0.02	0.33 ± 0.12	Israel II
10243	0.46 ± 0.02	0.34 ± 0.13	Israel II
10244	0.46 ± 0.02	<0.44 (90% C.L.)	Israel II
10245	0.75 ± 0.03	<0.47 (90% C.L.)	Israel II
10246	0.77 ± 0.03	<0.58 (90% C.L.)	Israel II
10247	0.51 ± 0.02	<0.77 (90% C.L.)	Israel II
10248	0.54 ± 0.02	<0.58 (90% C.L.)	Israel II
10249	0.91 ± 0.03	2.59 ± 0.19	Israel II
10250	0.83 ± 0.03	9.22 ± 0.36	Israel II
10251	0.99 ± 0.03	<0.54 (90% C.L.)	Israel II
10252	0.49 ± 0.02	<0.49 (90% C.L.)	Israel II
10253	0.60 ± 0.02	<0.51 (90% C.L.)	Israel II
10254	0.72 ± 0.03	24.0 ± 0.8	Israel II
10257	3.63 ± 0.11	23.4 ± 0.8	South Africa

Table C.1: ATTA Results for May 2014 - February 2017, including ATTA trace number, $^{81}Kr/^{81}Kr_{atmosphere}$ ratios, ^{85}Kr activities (in dpm/cc), and a short name for the project with which each sample is associated. For results below the detection limit, an upper limit is placed at the 90% confidence level. ATTA trace numbers which are marked with a "*" denote that the measurement was conducted in the rapid-processing mode described in the Chapter 5, and thus no ^{81}Kr-results are available. Repeated trace numbers mean a repeated measurement on the same sample from the same holder. Note, the ^{85}Kr activities are the measured activities on the analysis date, which may be significantly lower than the value on the sampling date due to radioactive decay between the two dates.

Laboratory for Radiokrypton Dating, Physics Division, Argonne National Laboratory, Argonne, IL 60439
(630)252-4123 www.phy.anl.gov/mep/atta/

Argonne NATIONAL LABORATORY

Atom Trap Trace Analysis (ATTA) Report

Report No. 0XX **Report Date** 00 XXX 20XX **Project Name** XXXXXX

Samples supplied by:
Samples analyzed by: Jake Zappala, Peter Mueller (ANL)

ATTA trace No.	Sample	Sampling comments	Sampling Date	Sample Used (micro-L)	ATTA Date	^{85}Kr (dpm/cc)	^{81}Kr sample / air	ATTA Lab comments
102xx	Well Name	Country/Region	01 Mar 2017	~ 8	01 Apr 2017	75.0 ± 1.5	1.00 ± 0.03	Kr : N_2 : O_2 : CH_4 = 1.0 : 0.3 : 0.3 : 0.3
102xx	Well Name	Country/Region	02 Mar 2017	~ 8	02 Apr 2017	< 0.50 (90%C.L.)	0.50 ± 0.02	Kr : N_2 : O_2 : CH_4 = 1.0 : 0.3 : 0.3 : 0.3

Notes

- **^{85}Kr** ($t_{1/2}$ = 10.76 ± 0.02 yr) abundance is reported in dpm/cc (decays per minute per cc STP of krypton).
  - Conversion: 100 dpm/cc corresponds to the isotopic abundance of ^{85}Kr/Kr = 3.03E-11.
  - The reported ^{85}Kr value is as measured on the ATTA analysis date. It may be significantly lower than the value on the sampling date due to radioactive decay in between the two dates.
- **^{81}Kr** ($t_{1/2}$ = 229 ± 11 kyr) abundance is reported as the sample-to-air ratio: $(^{81}Kr/Kr)_{sample}$ / $(^{81}Kr/Kr)_{air}$.

Figure C.1: Template ATTA Report for collaborators. Information regarding the reporting is included at the bottom of the report. The "ATTA Lab Comments" are the gas abundances relative to krypton that are typically seen in environmental samples, as measured by the RGA.

REFERENCES

[1] K. M. Hiscock. *Hydrogeology: Principles and Practice*, 2nd Ed. Wiley (2014).

[2] P. Collon, W. Kutschera and Z.-T. Lu. Tracing noble gas radionuclides in the environment. *Annu. Rev. Nucl. Part. Sci.* **54**, 39-67 (2004).

[3] W. F. Libby, E. C. Anderson, J. R. Arnold. Age determination by radiocarbon content: World-wide assay of natural radiocarbon. *Science* **109**, 227-228 (1949).

[4] L. N. Plummer. Radiocarbon dating in groundwater systems, in: Suckow, A., Aggarwal, P., and Araguas-Araguas, L. (Eds.) *Isotope Methods for Dating Old Groundwater*, International Atomic Energy Agency, Vienna, 33-73 (2013).

[5] H. Godwin. Half life of radiocarbon, *Nature* **195**, 984 (1962).

[6] W. G. Mook. Preface to hydrology section. *Radiocarbon after Four Decades: An Interdisciplinary Perspective*. Springer. 241 (1992).

[7] C. M. Baglin. Nuclear Data Sheets Update for A = 81. *Nucl. Data Sheet* **69**, 267 (1993).

[8] B. Singh and J. Chen. Nuclear Data Sheets for A = 85. *Nucl. Data Sheet* **116**, 36 (2014).

[9] B. Singh and J. A. Cameron. Nuclear Data Sheets for A = 39. *Nucl. Data Sheet* **107**, 244 (2006).

[10] J. Ahlswede, S. Hebel, J. O. Ross, R. Schoetter, and M. B. Kalinowski. Update and improvement of the global krypton-85 emission inventory. *J. Environ. Radioactivity* **115**, 34-42 (2013).

[11] Z.-T. Lu, P. Schlosser, W. M. Smethie Jr., N. C. Sturchio, T. P. Fischer, B. M. Kennedy, R. Purtschert, J. P. Severinghaus, D. K. Solomon, T. Tanhua and R. Yokochi. Tracer Applications of Noble Gas Radionuclides in the Geosciences. *Earth-Science Reviews* **138**, 196-214 (2014).

[12] C. Buizert, D. Baggenstos, W. Jiang, R. Purtschert, V.V. Petrenko, Z.-T. Lu, P. Müller, T. Kuhl, J. Lee, J.P. Severinghaus, and E.J. Brook. Radiometric ^{81}Kr dating identifies 120,000-year-old ice at Taylor Glacier, Antarctica. *Proceedings of the National Academy of Sciences* **111**, 6876 (2014).

[13] W. Jiang, W. D. Williams, K. Bailey, A. M. Davis, S.-M. Hu, Z.-T. Lu, T.P. O'Connor, R. Purtschert, N.C. Sturchio, Y.R. Sun, and P. Mueller. Ar-39 detection at the 10^{16} isotopic abundance level with atom trap trace analysis. *Phys. Rev. Lett.* **106**, 103001 (2011).

[14] F. Ritterbusch, S. Ebser, J. Welte, T. Reichel, A. Kersting, R. Purtschert, W. Aeschbach-Hertig, and M. K. Oberthaler. Groundwater dating with Atom Trap Trace Analysis of ^{39}Ar. *Geophys. Res. Lett.* **41**, 6758-6764 (2014).

[15] J. H. Reynolds. A New Long-Lived Krypton Activity. *Phys. Rev. Lett.* **886** (1950).

[16] H. H. Loosli and H. Oeschger. ^{37}Ar and ^{81}Kr in the atmosphere. *Earth Planet. Sci. Lett.* **7**, 6771 (1969).

[17] N. Aoki and M. Yoshihiro. The Concentration of Krypton in the Atmosphere, Its Revision after Half a Century. *Chemistry Letters* **34**, 1396-1397 (2005).

[18] P. Collon, T. Antaya, B. Davids, M. Fauerbach, R. Harkewicz, M. Hellstrom, W. Kutschera, D. Morrissey, R. Pardo, M. Paul, B. Sherrill, and M. Steiner. Measurement of ^{81}Kr in the atmosphere. *Nucl. Instrum. Meth.* **B123**, 122127 (1997).

[19] P. Collon, W. Kutschera, H. H. Loosli, B. E. Lehmann, R. Purtschert, A. Love, L. Sampson, D. Anthony, D. Cole, B. Davids, D. J. Morrissey, B. M. Sherrill, M. Steiner, R. C. Pardo, and M. Paul. ^{81}Kr in the Great Artesian Basin. *Earth Planet. Sci. Lett.* **182**, 103113 (2000).

[20] C.-Y. Chen, Y. M. Li, K. Bailey, T. P. O'Connor, L. Young, and Z.-T. Lu. Ultrasensitive isotope trace analysis with a magneto-optical trap. *Science* **286**, 1139-1141 (1999).

[21] X. Du, R. Purtschert, K. Bailey, B. E. Lehmann, R. Lorenzo, Z.-T. Lu, P. Mueller, T. P. O'Connor, N. C. Sturchio and L. Young. A new method of measuring ^{81}Kr and ^{85}Kr abundances in environmental samples. *Geophys. Res. Lett.* **30**, 2068-2071 (2003).

[22] N. C. Sturchio, X. Du, R. Purtschert, B. Lehmann, M. Sultan, L. J. Patterson, Z.-T. Lu, P. Mueller, T. Bigler, K. Bailey, T. P. O'Connor, L. Young, R. Lorenzo, R. Becker, Z. El Alfy, B. El Kaliouby, Y. Dawood, and A. M. A. Abdallah. One million year old groundwater in the Sahara revealed by krypton-81 and chlorine-36. *Geophys. Res. Lett.* **31**, L05503 (2004).

[23] W. Jiang, K. Bailey, Z.-T. Lu, P. Mueller, T. P. O'Connor, C.-F. Cheng, S.-M. Hu, R. Purtschert, N. C. Sturchio, Y. R. Sun, W. D. Williams, and G.-M. Yang. An Atom Counter for Measuring ^{81}Kr and ^{85}Kr in Environmental Samples. *Geochim. Cosmochi. Acta* **91**, 1-6 (2012).

[24] P. Collon, D. Cole, B. Davids, M. Fauerbach, R. Harkewicz, W. Kutschera, D. J. Morrissey, R. C. Pardo, M. Paul, B. M. Sherrill, and M. Steiner. Measurement of the long-lived radionuclide ^{81}Kr in pre-nuclear and present-day atmospheric krypton. *Radiochim. Acta* **85**, 13-19 (1999).

[25] R. Yokochi, N.C. Sturchio, R. Purtschert, W. Jiang, Z.-T. Lu, P. Mueller, G.-M. Yang, B. M. Kennedy, Y. Kharaka. Noble gas radionuclides in Yellowstone geothermal gas emissions: A reconnaissance. *Chemical Geology* **339**, 43 (2013).

[26] N. C. Sturchio, K. L. Kuhlman, R. Yokochi, P. C. Probst, W. Jiang, Z.-T. Lu, P. Mueller, G.-M. Yang. Krypton-81 in Groundwater of the Culebra Dolomite Near the Waste Isolation Pilot Plant, New Mexico. *Journal of Contaminant Hydrology* **160**, 12 (2014).

[27] P. K. Aggarwal, T. Matsumoto, N. C. Sturchio, H. K. Chang, D. Gastmans, L. J. Araguas-Araguas, W. Jiang, Z.-T. Lu, P. Mueller, R. Yokochi, R. Purtschert and T. Torgersen. Continental degassing of ^{4}He by surficial discharge of deep groundwater. *Nature Geoscience* **8**, 35 (2015).

[28] C. J. Foot. *Atomic Physics*. Oxford University Press, New York (2005).

[29] B. D. Cannon. Hyperfine spectra of the radioactive isotopes ^{81}Kr and ^{85}Kr. *Phys. Rev. A* **47**, 1148 (1993).

[30] X. Du. Realization of Radio-Krypton Dating with an Atom Trap. Doctoral Thesis. Northwestern University.

[31] J. L. Hall, L. Hollberg, T. Baer, and H. G. Robinson. Optical heterodyne saturation spectroscopy. *App. Phys. Lett.* **39**, 680 (1981).

[32] J. C. Zappala, K. Bailey, Z.-T. Lu, T. P. O'Connor, and W. Jiang. Efficient generation of optical sidebands at GHz with a high-power tapered amplifier. *Review of Scientific Instruments* **85**, 046104 (2014).

[33] C. Y. Chen, K. Bailey, X. Du, Y. M. Li, Z.-T. Lu, T. P. O'Connor, L. Young, and G. Winkler. A Beam of Metastable Krypton Atoms Extracted from an RF-Driven Discharge. *Review of Scientific Instruments* **72**, 271 (2001).

[34] W. W. Macalpine and R. O. Schildknecht. Coaxial resonators with helical inner conductors, *Proc. IRE* 2099-2105 (1959).

[35] W. Rooijakkers, W. Hogervorst, and W. Vassen. An intense collimated beam of metastable helium atoms by two-dimensional laser cooling. *Opt. Commun.* **123** 321-230 (1996).

[36] J. Welte, F. Ritterbusch, I. Steinke, M. Henrich, W. Aeschbach-Hertig, and M. K.

Oberthaler. Towards the realization of atom trap trace analysis for ^{39}Ar. *New J. Phys.* **12**, 065031 (2010).

[37] E. L. Raab, M. Prentiss, A. Cable, S. Chu, and D. E. Pritchard. Trapping of neutral sodium atoms with radiation pressure. *Phys. Rev. Lett.* **59**, 26312634 (1987).

[38] W. Phillips and H. Metcalf. Laser deceleration of an atomic beam. *Phys. Rev. Lett.* **48**, 596 (1982).

[39] W. Jiang, K. Bailey, Z.-T. Lu, P. Mueller, T. P. O'Connor, and R. Purtschert. Ion current as a precise measure of the loading rate of a magneto-optical trap. *Optics Letters* **39**, 409-412 (2014).

[40] T. A. Maldonado, Electro-optic modulators, in Handbook of Optics, 2nd ed., edited by M. Bass (McGraw-Hill, 2010), Vol. 2.

[41] *NASA Earth Fact Sheet* (2016) http://nssdc.gsfc.nasa.gov/planetary/factsheet/earthfact.html.

[42] F. von Hippel, D. H. Albright, B. G. and Levi. Stopping the Production of Fissile Material for Weapons. *Sci. American* **253**, 40 (1985).

[43] T. R. England and B. F. Rider. Evaluation and Compilation of Fission Product Yields 1993. ENDF-349, Los Alamos National Laboratory, New Mexico (1994).

[44] J. T. Goorley, M. R. James, T. E. Booth, F. B. Brown, J. S. Bull, L. J. Cox, J. W. Durkee Jr., J. S. Elson, M. L. Fensin, R. A. Forster III, J. S. Hendricks, H. G. Hughes III, R. C. Johns, B. C. Kiedrowski, R. L. Martz, S. G. Mashnik, G. W. McKinney, D. B. Pelowitz, R. E. Prael, J. E. Sweezy, L. S. Waters, T. Wilcox, A. J. Zukaitis. Initial MCNP6 Release Overview MCNP6 Version 1.0. LA-UR-13-22934, Los Alamos National Laboratory, New Mexico (2013).

[45] J. H. Hubbell and S. M. Seltzer. Tables of X-Ray Mass Attenuation Coefficients and Mass Energy-Absorption Coefficients from 1 keV to 20 MeV for Elements Z = 1 to 92 and

48 Additional Substances of Dosimetric Interest. NIST Standard Reference Database 126, http://physics.nist.gov/PhysRefData/XrayMassCoef/tab2.html (1996, last update 2004).

[46] J. M. Wallace and P. V. Hobbs. *Atmospheric Science: An Introductory Survey* 2nd Ed., Elsevier (2006).

[47] J. K. Shultis and R. E. Faw. *Radiation Shielding*, Prentice-Hall (1996).

[48] S. Glasstone and R. H. Lovberg. *Controlled Thermonuclear Reactions: An Introduction to Theory and Experiment*. Robert E. Krieger Publishing Company (1960).

[49] N. Soppera, M. Bossant, E. Dupont. JANIS 4: An Improved Version of the NEA Java-based Nuclear Data Information System. *Nucl. Data Sheet* **120**, 294-296 (2014).

[50] Union of Concern Scientists. How Nuclear Weapons Work. http://www.ucsusa.org/nuclear-weapons/how-do-nuclear-weapons-work#.WB4JLOErLsk (2009).

[51] *Tables of Physical & Chemical Constants* (16th edition, 1995). 4.7.4 Nuclear Fusion. Kaye & Laby Online. Version 1.0. www.kayelaby.npl.co.uk (2005).

[52] United Nations. Sources and Effects of Ionizing Radiation. United Nations Scientific Committee on the Effects of Atomic Radiation. 1993 Report to the General Assembly, with annexes. United Nations sales publication E.94.IX. 2. United Nations, New York. (Annex B, 1993).

[53] V. V. Kuzminov and A. A. Pomansky. New measurement of the ^{81}Kr atmospheric abundance. *Radiocarbon* **22**, 311-317 (1980).

[54] J. E. Moran, G. B. Hudson, G. F. Eaton, and R. Leif. California GAMA Program: Groundwater Ambient Monitoring and Assessment Results for the Sacremento Valley and Volcanic Provinces of Northern California. Lawrence Livermore National Laboratory, UCRL-TR209191 (2005).

[55] P. G. Cook and D. K. Solomon. Transport of atmospheric trace gases to the water table: Implications for groundwater dating with chlorofluorocarbons and krypton 85. *Water Resour. Res.* **31**, 263-270 (1995).

[56] H. Loosli, B. E. Lehmann, and W. R. Smethie Jr. Noble gas radioisotopes (^{37}Ar, ^{85}Kr, ^{39}Ar, ^{81}Kr), in: P. G. Cook, and A. L. Herczeg (Eds.), *Environmental Tracers in Subsurface Hydrology*, Kluwer, 379-396 (1999).

[57] A. Visser, H. P. Broers, and M. F. Bierkens. Dating degassed groundwater with ^{3}H/^{3}He *Water Resour. Res.* **43**, W10434 (2007).

[58] L. N. Plummer, E. Busenberg, P. G. Cook. Principles of Chlorofluorocarbons Dating, in: *Use of Chlorofluorocarbons in Hydrology*. International Atomic Energy Agency, Vienna, 17-30 (2006).

[59] M. Kalinowski, H. Sartorius, S. Uhl, and W. Weiss. Conclusions on plutonium separation from atmospheric krypton-85 measured at various distances from the Karlsruhe reprocessing plant. *Journal of Environmental Radioactivity* **73**, 203-222 (2004).

[60] F. J. Klingberg, S. Hebel, M. Kilian, M. B. Kalinowski, and G. Wotawa. Simulation of atmospheric noble gas transport to assess sampling procedures for locating unreported reprocessing. Paper to a poster presented at the *IAEA Symposium on International Safeguards*, 1-5 November 2010, IAEA-CN-184/36 (2010).

[61] J. Schröder. Krypton-85 in the Ocean. *Zeitschrift für Naturforschung A* **30**, 962-967 (1975).

[62] W. M. Smethie, Jr., D. K. Solomon, S. L. Schiff, and G. G. Mathieu. Tracing groundwater flow in the Borden aquifer using krypton-85. *Journal of Hydrology* **130**, 279-297 (1992).

[63] J. A. Corcho Alvarado, R. Purtschert, F. Barbecot, C. Chabault, J. Rueedi, V. Schneider, W. Aeschbach-Hertig, R. Kipfer, and H. H. Loosli. Constraining the age distribution of highly mixed groundwater using ^{39}Ar: a multiple environmental tracer (^{3}H/^{3}He, ^{85}Kr, ^{39}Ar, and ^{14}C) study in the semiconfined Fontainebleau Sands Aquifer (France). *Water Resources Research* **43**, W03427 (2007).

[64] R. Althaus, S. Klump, A. Onnis, R. Kipfer, R. Purtschert, F. Stauffer, and W. Kinzelbach. Noble gas tracers for characterisation of flow dynamics and origin of groundwater: A case study in Switzerland. *Journal of Hydrology* **370**, 64-72 (2009).

[65] A. Visser, H. P. Broers, R. Purtschert, J. Sültenfuß, and M. De Jonge. Groundwater age distributions at a public drinking water supply well field derived from multiple age tracers (^{85}Kr, ^{3}H/^{3}He, noble gases and ^{39}Ar). *Water Resour. Res.* **49**, 7778-7796 (2013).

[66] A. Mayer, J. Sültenfuß, Y. Travi, R. Rebeix, C. Claude, R. Purtschert, H. Miche, C. Le Gal La Salle, and E. Conchetto. A multi-tracer study of groundwater origin and transit-time in the aquifers of the Venice region (Italy). *Applied Geochemistry* **50**, 177-198 (2014).

[67] C. Delbart, F. Barbecot, D. Valdes, A. Tognelli, E. Fourre, R. Purtschert, and P. Jean-Baptiste. Investigation of young water inflow in karst aquifers using SF_6-CFC-^{3}H/^{3}He-^{85}Kr-^{39}Ar and stable isotope components. *Applied Geochemistry* **50**, 164-176 (2014).

[68] J. Alikhani, A. Deinhart, A. Visser, R. Bibby, R. Purtschert, J. Moran, A. Massoudieh, and B. Esser. Nitrate vulnerability projections from Bayesian inference of multiple groundwater age tracers, *Journal of Hydrology* **543**, 167-181 (2016).

[69] R. Purtschert, R. Yokochi, and N. Sturchio. Kr-81 dating of old groundwater, in: A. Suckow, P. Aggarwal, and L. Araguas-Araguas (Eds.) *Isotope Methods for Dating Old Groundwater*, International Atomic Energy Agency, Vienna, 91-122 (2013).

[70] R. Yokochi. Recent developments on field gas extraction and sample preparation methods for radiokrypton dating of groundwater. *Journal of Hydrology* **540**, 368-378 (2016).

[71] L. N. Plummer and L. C. Friedman. US Geological Survey, Fact Sheet-134-99 (1999).

[72] H. H. Loosli and R. Purtschert. Rare Gases, in: P. Aggarwal, J. R. Gat, K. Froehlich (Eds.), *Isotopes in the Water Cycle: Past, Present and Future of a Developing Science.* International Atomic Energy Agency, Vienna, 91-95 (2005).

[73] C. Gerber, R. Vaikmäe, W. Aeschbach, A. Babre; W. Jiang, M. Leuenberger, Z.-T. Lu, R. Mokrik, P. Müller, V. Raidla, T. Saks, H. N. Waber, T. Weissbach, J. C. Zappala, and R. Purtschert. Using ^{81}Kr and Noble Gases to Characterize and Date Groundwater and Brines in the Baltic Artesian Basin on the One-Million-Year Timescale. *Geochim. et Cosmichim. Acta* **205**, 187-210 (2017).

[74] H. Beer. Capture cross section measurements of krypton and xenon isotopes and the fundamental parameters of the s-process. *Astrophysical Journal*, Part 1 (ISSN 0004-637X), **375**, 823-832 (1991).

[75] S. Halfon, A. Arenshtam, D. Kijel, M. Paul, D. Berkovits, I. Eliyahu, G. Feinberg, M. Friedman, N. Hazenshprung, I. Mardor, A. Nagler, G. Shimel, M. Tessler, I. Silverman. High-Power Liquid-Lithium Jet Target for Neutron Production. *Rev. Sci. Instrum.* **84** (12), 123507 (2013).

[76] R. Yokochi, University of Chicago. Private communication (2017).

[77] S. K. Morrissey, J. F. Clark, M. Bennett, E. Richardson, and M. Stute. Groundwater reorganization in the Floridan aquifer following Holocene sea-level rise. *Nature Geoscience* **3**, 683 (2010).

[78] N. C. Sturchio. Results of Radiokrypton Analyses of Monitoring Wells AEC-7R, H-12R,

and SNL-16 Near the Waste Isolation Pilot Plant, New Mexico. Report prepared for Sandia National Laboratories (2016).

[79] R. Ram, J. Zappala, R. Yokochi, Z.-T. Lu, Y. Yechieli, A. Burg, R. Purtschert, R. Bernier, W. Jiang, P. Mueller, E. Adar. ^{81}Kr ages shed new light on groundwater flow in the deep Nubian Sandstone Aquifer (Israel). Draft (2017).

[80] R. Purtschert, University of Bern. Private communication (2017).

[81] L. Young, D. Yang, and R. W. Dunford. Optical production of metastable krypton. *J. Phys. B At. Mol. Opt. Phys.* **35** 2985-2992 (2002).

[82] Y. Ding, S.-M. Hu, K. Bailey, A. M. Davis, R. W. Dunford, Z.-T. Lu, T. P. O'Connor, and L. Young. Thermal beam of metastable krypton atoms produced by optical excitation. *Rev. Sci. Instru.* **78**, 023103 (2007).

[83] MgF_2 Broadband Precision Window, Uncoated. WG61050. Thorlabs (Sept. 2011).

[84] W. Jiang, University of Science and Technology of China. Private communication (2014).

[85] J. H. Moore, C. C. Davis, and M. A. Coplan. *Building Scientific Apparatus*, 4th Ed. Cambridge University Press (2012).

[86] J. Goldstein. *Scanning Electron Microscopy and X-Ray Microanalysis*, 3rd Ed. Springer (2003).

[87] L. J. Stinson, J. A. Howard, and R. C. Neville. Sulfur hexafluoride etching effects in silicon. *J. Electrochem. Soc.* **123**, 551-555 (1976).